9th DELTA
User Meeting

&

Annual Report 2013

Dortmund
27. November 2013

Edited by C. Sternemann, R. Wagner,
D. Lützenkirchen-Hecht (2013)

Preface

Dear reader, dear colleague,

synchrotron radiation provided by the DELTA storage ring is used in many different ways at the beamlines and experiments installed, and various research groups in physics, biology, chemistry, materials and accelerator science make use from the opportunity to perform experiments at DELTA for their activities. This annual report summarizes the results of the experiments that have been performed in the past year, reflecting the diversity of the research conducted here.

It is impressive to see the first scientific results of the new set-ups that have been installed in the past years. Here, the time-resolved photoemission experiments at beamline BL5 using ultra-short photon pulses produced by coherent harmonic generation should be mentioned and first user experiments have been conducted at the third wiggler beamline BL10. This is particularly important because the new hard X-ray beamline may relieve the overbooking of BL9. Moreover new InSb-monochromator crystals have been installed at beamline BL8 in order to serve the low energy X-ray range from ca. 1.7 to 4 keV. Accordingly BL8 has been operated in a low-energy mode for several months for commissioning and optimization of the beamline and its experimental endstation.

Despite the problems that occur from time to time, it was possible to deliver an intense and stable beam thanks to the high motivation of the DELTA staff members. They have contributed in many ways to the success of each individual project, and they are therefore also responsible for the success of the research conducted. And let us also thank Monika Voits-Besli and Petra Lindemann for their administrative work – without them, it would hardly be possible to organize and arrange the user-program and the user-meeting at DELTA.

Finally, we acknowledge the financial support of DELTA by the different funding agencies, the local government, the TU Dortmund and the involved universities. We are looking forward to the upcoming beamtime periods, hoping that they will be as productive and successful as during the last year!

Christian Sternemann, Ralph Wagner & Dirk Lützenkirchen-Hecht

Contents:

Instrumentation

STATUS OF THE DELTA SHORT-PULSE FACILITY*

H. Huck, F. Bahnsen, J. Grewe, M. Höner, M. Huck, S. Khan, R. Molo, A. Schick, P. Ungelenk,
Center for Synchrotron Radiation (DELTA), TU Dortmund University, Dortmund
S. Cramm, S. Döring, L. Plucinski, C.M. Schneider, Forschungszentrum Jülich (FZJ) PGI6, Jülich

Synchrotron radiation pulses from electron storage rings are typically 30-100 ps long, determined by the electron bunch length. To explore the femtosecond timescale, seeding techniques originally designed for linear-accelerator-based free-electron lasers [1] can be employed at storage rings as well. One method is Coherent Harmonic Generation (CHG) [2, 3, 4]. The principle of CHG is illustrated in Fig. 1. The interaction between the electrons and a co-propagating laser pulse in a first undulator (the "modulator") causes a periodic energy modulation within a small slice (typically 50 fs long) of the bunch. Energy-dependent path-length differences in a dispersive chicane result in microbunches, which radiate coherently at harmonics of the laser wavelength in a second undulator, the "radiator". Typically, the radiator can be tuned to provide ultrashort pulses with reasonable intensity up to the 5th harmonic. Doubling or tripling the frequency of the external laser pulse through nonlinear crystals, as well as the extension of the scheme to so-called Echo-Enabled Harmonic Generation (EEHG) [5], allows for even shorter wavelengths.

At the storage ring DELTA operated by the TU Dortmund University, a new CHG source with focus on user availability is under commissioning since 2011 [6, 7]. The goal is to provide ultrashort pulses at 23 eV (53 nm, the 5th harmonic of 265 nm) for future pump-probe experiments in standard routine operation. Currently, 400 nm pulses from a second-harmonic conversion unit after a Ti:Sapphire laser system are used. With the radiator tuned to the second harmonic thereof, 200 nm CHG pulses are routinely observed in a diagnostic hutch.

Since early 2013, higher harmonics are also observed in the VUV beamline BL 5 operated by the Forschungszentrum Jülich. Furthermore, the dedicated THz beamline BL 5a provides valuable information about the laser-induced energy modulation of the electrons. As an upgrade to the CHG facility at DELTA, plans for EEHG exist [8], which will provide coherent radiation pulses at even higher photon energies (60-100 eV). For this purpose, two additional undulators are needed, and the northern straight section of the storage ring must be extended to accommodate them.

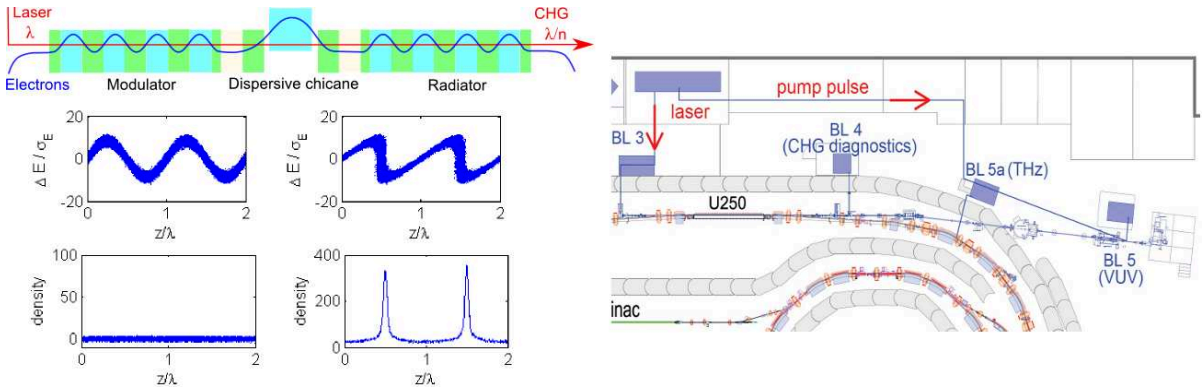

Figure 1: Principle of Coherent Harmonic Generation (left, see text) and layout of the DELTA short-pulse facility (right). Laser pulses are sent through BL 3 into the undulator U250. The resulting CHG pulses can be observed in BL 4 or used for pump-probe experiments in BL 5 while coherent THz radiation is detected in BL 5a.

Chicane Upgrade and Coherence Measurements

The degree of microbunching depends on the strength of the chicane r_{56}. In order to obtain the optimum microbunching, the relation $\lambda_L/\mathrm{h} \approx r_{56}\Delta E/E$ must hold, in which λ_L is the seed wavelength and $\Delta E/E$ the energy modulation amplitude. Since the energy modulation is limited by the available laser pulse energy and ultimately by the energy acceptance of the storage ring, the chicane strength is the key parameter to achieve the optimum microbunching. Until the beginning of 2013, the r_{56} value was limited to 11 µm. It was increased up to 130 µm by rewiring the magnetic poles of the chicane [9], which caused a dramatic rise in the intensity of the CHG radiation (see Fig. 2a).

With the new chicane, CHG pulses up to the fifth harmonic (15.5 eV) have been detected in BL 5, using a delay-line detector (DLD) with modified readout electronics [10]. The highest observed ratio between photoelectron counts from a gold target due to CHG and due to spontaneous radiation was about 600 at 6.2 eV and 150 at 9.3 eV (Fig. 2b,c).

* Work supported by DFG (INST 212/236-1 FUGG), BMBF (05K10PE1, 05K10PEB), and the Federal State NRW

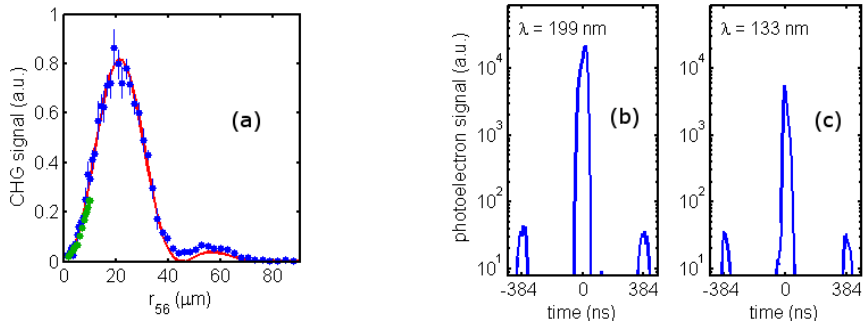

Figure 2: CHG intensity vs. chicane strength (a), and CHG (at t = 0) and spontaneous emission (at t = ± 384 ns) signal from photoelectrons detected by the DLD in BL 5 at 6.2 eV (b) and 9.3 eV (c).

The transverse coherence degree of the second-harmonic CHG pulses has been measured to ≈0.76 by evaluating the fringe pattern behind a double slit in the diagnostic hutch [11], and the coherence length has been measured by delaying light from one slit to about 15 fs, in accordance with the spectral width of about 0f FWHM.

Pump-Probe Overlap

In order to enable pump-probe experiments using the CHG pulses, an evacuated laser beamline has been built to send a fraction of each laser pulse with a variable delay to the experimental station of BL5. After establishing the spatial overlap of undulator radiation and pump pulses on the sample, observed by a CCD camera, the pump and probe pulses must be temporally overlapped by adjusting the length of the 53 m pump beamline with an accuracy of approx. 15 µm. This was achieved using two-photon absorption of the pump pulses and the seed laser pulses instead of CHG radiation in a SiC photodiode (taking into account the small and well-known delay between). The two-photon signal (Fig. 3 left) shows a FWHM of a few ps, mainly caused by the seed pulse lengthening in the monochromator (Δt H $n\lambda/c$ for n grating grooves). In order to achieve a sub-ps temporal resolution, it is planned to install a grating with less grooves per mm.

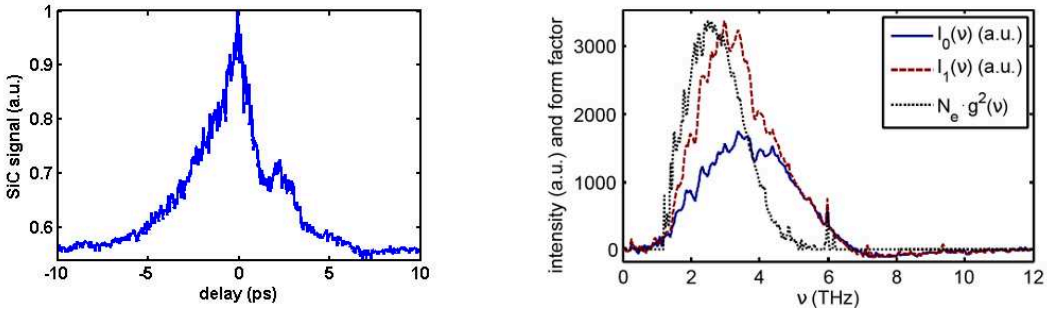

Figure 3: Two-photon absorption of pump and seed laser (left). The right graph shows incoherent (I_0) and coherent (I_1) THz spectra, and their (normalized) ratio.

Coherent THz Pulses

Ultrashort and coherent THz pulses, which are also caused by the laser-electron interaction in the U250, are detected in a dedicated beamline (BL 5a). The THz signal is routinely used to find and optimize the laser-electron overlap and to perform electron beam diagnostics, e.g. measuring the longitudinal bunch profile [12]. First results from the newly installed FT-IR spectrometer at BL 5a show coherent radiation reaching from 1.8 to 3.8 THz (Fig. 3) in good agreement with previous simulations [13]. Furthermore, ultrafast THz detectors [14, 15] have been used in cooperation with KIT in Karlsruhe to study the evolution of the laser-induced density modulation over several revolutions in the storage ring [13]. It is planned to permanently install such a fast detector at BL 5a as well as to use long intensity-modulated laser pulses to produce narrow-banded THz radiation [16].

[1] E. Allaria et al., Nature Photonics 6, 699 (2012).
[2] B. Girard et al., Phys. Rev. Lett. 53, 2405 (1984).
[3] E. Allaria et al., Phys. Rev. Lett. 100, 174801 (2008).
[4] M. Labat et al., Phys. Rev. Lett. 101, 164803 (2008).
[5] G. Stupakov, Phys. Rev. Lett. 102, 074801 (2009).
[6] H. Huck et al., Proc. FEL conf. 2011, Shanghai, 5.
[7] S. Khan et al., Sync. Rad. News, Vol. 26, 25 (2013).
[8] R. Molo et al., Proc. FEL conf. 2011, Shanghai, 219.
[9] R. Molo et al., Proc. IPAC 2013, Shanghai, 1889.
[10] S. Döring et al., DELTA User Meeting (2013).
[11] M. Huck et al., Proc. IPAC 2013, Shanghai, 2132.
[12] P. Ungelenk et al., Proc. IPAC 2012, New Orleans, 768.
[13] P. Ungelenk et al., Proc. IPAC 2013, Shanghai, 94.
[14] A. D. Semenov et al., Proc. of IRMMW-THz 2009, 5324688.
[15] P. Probst et al., Appl. Phys. Lett. 98, 043504 (2011).
[16] S. Bielawski et al., Nature Physics 4, 390 (2008).

A short-pulse facility for time and angle resolved photoemission experiments at BL5

S. Döring[1,2], L. Plucinski[1,2], S. Cramm[1], H. Huck[3], M. Huck[3], M. Höner[3], R. Molo[3], A. Schick[3], P. Ungelenk[3], S. Khan[3], C.M. Schneider[1,2]

[1] Peter Grünberg Institut, PGI-6, Forschungszentrum Jülich GmbH, D-52425 Jülich, Germany
[2] Experimentalphysik - Universität Duisburg-Essen, Lotharstr. 1, 47057 Duisburg
[3] DELTA - TU Dortmund, Maria-Goeppert-Mayer-Str. 2, D-44221 Dortmund, Germany

(October 2013)

In a joint cooperation between the machine group of DELTA and the user group from PGI-6, a facility for performing time-resolved photoemission experiments is under commissioning utilizing the existing undulator beamline BL5 and the current end-station. The ultra-short photon pulses are produced by the DELTA storage ring using the coherent harmonic generation (CHG) scheme [1]. Only small modifications are necessary at the end-station of BL5 [2] and thus switching from standard spin-resolved ARPES experiments to time-resolved photoemission becomes straightforward. The goal of this activity is a pump-probe photoemission experiment with fs time resolution.

In order to provide CHG pulses for the experiments, one electron bunch in the storage ring is is overlapped with a strong laser pulse in the first part of the undulator U250, which is called modulator. This so-called seeding laser interacts with the electrons in a way that a density modulation in a short slice of the bunch is achieved when the electrons pass through a chicane which is at the center of the undulator. This modulation leads to the emission of short light pulses at higher harmonics of the original laser wavelength in the second part of the undulator, which is called radiator. The length of those pulses equals roughly the lengths of the seeding laser pulses and thus is much shorter than in conventional synchrotron light pulses. At the same time, this ultra-short pulse is much more intense than the radiation from non-modulated bunches.

Several modifications that were necessary to produce the CHG pulses were finished at the beginning of this year and this unique light source is ready to be used for photoemission experiments.

The first step towards time-resolved experiments was to identify the photoelectrons excited by CHG pulses and separate them from those excited by conventional synchrotron light. Therefore, we had to enable the experimental end-station to measure the photoelectrons with a time-resolution of a few nanoseconds, which is sufficient to separate the CHG pulse from the incoherent light pulses. Fortunately, the delay-line detector (DLD) that is attached to the photoelectron analyzer comes with an intrinsic time-resolution of a few picoseconds and by synchronizing this detector with the seeding laser we were able to record the photoelectrons from single light pulses. The inlets in Figure 1 show the Cu(111) surface state. We recorded this parabolic state at 9.35 eV which is the third harmonic of the seeding laser. The kinetic energy of the photoelectrons is between 4.5 eV and 4.7 eV.

Figure 1 shows the intensity of the detected photoelectrons as a function of time. The DLD is a two dimensional detector that maps the angular momentum of photoelectrons as a function of their kinetic energy. In the histogram we show the integrated intensity of those images. In standard photoemission experiments, the data are integrated over time and the implementation of this time-resolved mode requires synchronization to the

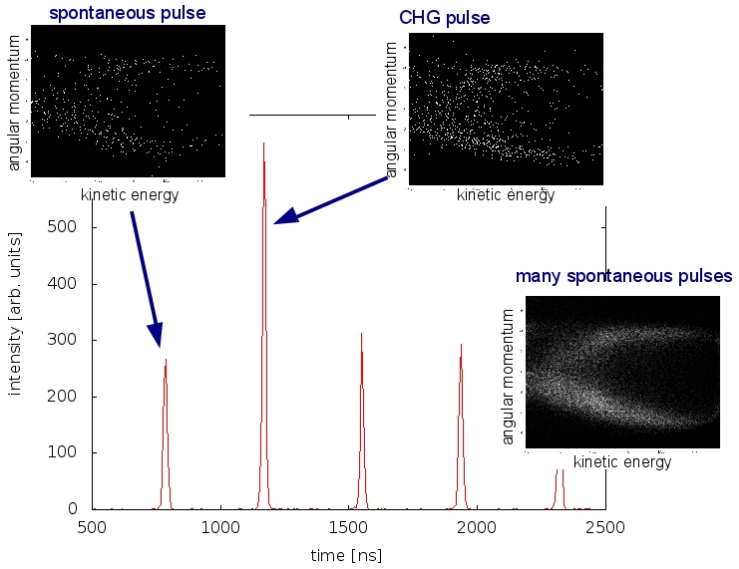

Figure 1: The photoelectron pulse excited by the CHG pulse is clearly separated from the photoelectrons that are excited by spontaneous synchrotron radiation in single-bunch mode. The inlets show DLD images. The pulses in the histogram are the integrals over those images.

CHG pulses. And this in turn required a larger buffer in the electronics of the DLD because the standard model is only able to buffer 100 microseconds. The seeding laser repetition rate is 1 kHz and, therefore, we had to buffer 1 millisecond. The modifications were performed by the company *Surface Concept GmbH* and the new hardware is fully operational since summer 2013.

The final goal is to implement the pump-probe process. A second beamline for the pump laser pulses is under commissioning since the beginning of this year. During the summer shut-down, the beamlines were connected and the pump laser light was brought up to the photoemission end-station. A delay-stage to vary the time between pump and probe pulses has been installed and the pump laser pulse has been overlapped in time and space with the seeding laser pulse which was guided through the synchrotron light beamline. This overlap was observed by a photo-diode in front of the end-station and, thus, the preparations for pump-probe photoemission experiments are nearly completed.

The first experiments will be performed on the magnetic system Co/Cu. The goal is to use the magnetic linear dichroism effect in order to track (de-)magnetization dynamics in this thin-film system. The main challenges that we encounter are connected to the low photon energy of the CHG pulses and the resulting low kinetic energies of the photoelectrons. Both, the beamline and the experimental end-station were not operated at this energy range before and require further modifications as well as calibrations.

[1] S. Khan, F. Bahnsen, S. Cramm, S. Döring, J. Grewe, M. Höner, H. Huck, M. Huck, R. Molo, L. Plucinski, A. Schick, C. M. Schneider und P. Ungelenk,*Generation of Ultrashort and Coherent Synchrotron Radiation Pulses at DELTA*, Synchrotron Radiation News **26**, 25 (2013).

[2] L. Plucinski, A. Oelsner, F. Matthes und C. Schneider, *A hemispherical photoelectron spectrometer with 2-dimensional delay-line detector and integrated spin-polarization analysis*, Journal of Electron Spectroscopy and Related Phenomena **181**, 215 (2010).

Beamline 5: Angle-resolved magnetic linear dichroism in resonant photoemission of thin Co films

Torsten Veltum[1]*, Tobias Löffler[1], Sven Döring[2], L. Plucinski[2] and Mathias Getzlaff[1]

[1] Institut für Angewandte Physik, Heinrich-Heine-Universität Düsseldorf, 40225 Düsseldorf
[2] Peter Grünberg Institut PGI-6, Forschungszentrum Jülich, 52428 Jülich
* torsten.veltum@uni-duesseldorf.de

Magnetic linear dichroism in the angular distribution of photoelectrons (MLDAD) is a technique that allows the study of both the electronic band structure and the magnetic properties of thin films and single crystals. In this study we use linearly polarized synchrotron radiation in the VUV regime.
The studied system is an epitaxially grown thin hcp(0001) Co film on a W(110) single-crystal. Preliminary characterization of the thin film is carried out by LEED as demonstrated by J. Bansmann et al. [1]. The easy magnetization axis for thin Co films lies in-plane and along the $[1\bar{1}00]$-direction, which corresponds to the W$[1\bar{1}0]$-direction. The magnetic linear dichroism requires a specific geometry as displayed in figure 1, where the linearly polarized light scatters in the xz-plane and the sample is magnetized in the y-direction.

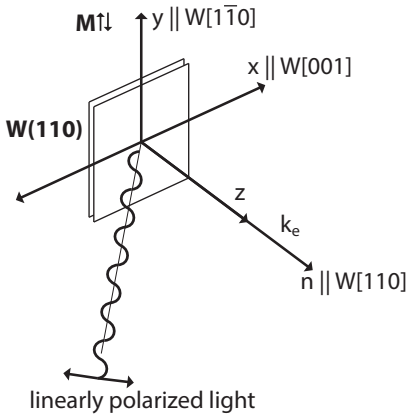

Figure 1: Geometric arrangement of sample and incoming photon beam with linear polarized radiation. The photoelectrons are detected in normal emission.

The experimental results for Co/W(110) in the photon energy range between 20 and 31 eV has already been discussed by J. Bansmann et al. [2], therefore we want to go to higher energies, up to the resonant photoemission at 60 - 80 eV photon energy. The results of our measurements are shown in figure 2. The spectra show both magnetization directions and compare very well to the results obtained by Bansmann et al. Notice a

peak emerging near the Fermi energy at 21 eV that shows clear magnetization dependence to up to 33 eV. Asymmetry values go as high as 10% in the low energy range. The effect of the dichroism is still visible to up to 50 eV, but is small compared to the lower energies, although there is an interesting effect at 33 to 35 eV, where the asymmetry switches direction. You may notice, that the blue line is always above and then below the red line up to 33 eV, and at higher energies, this is reversed.

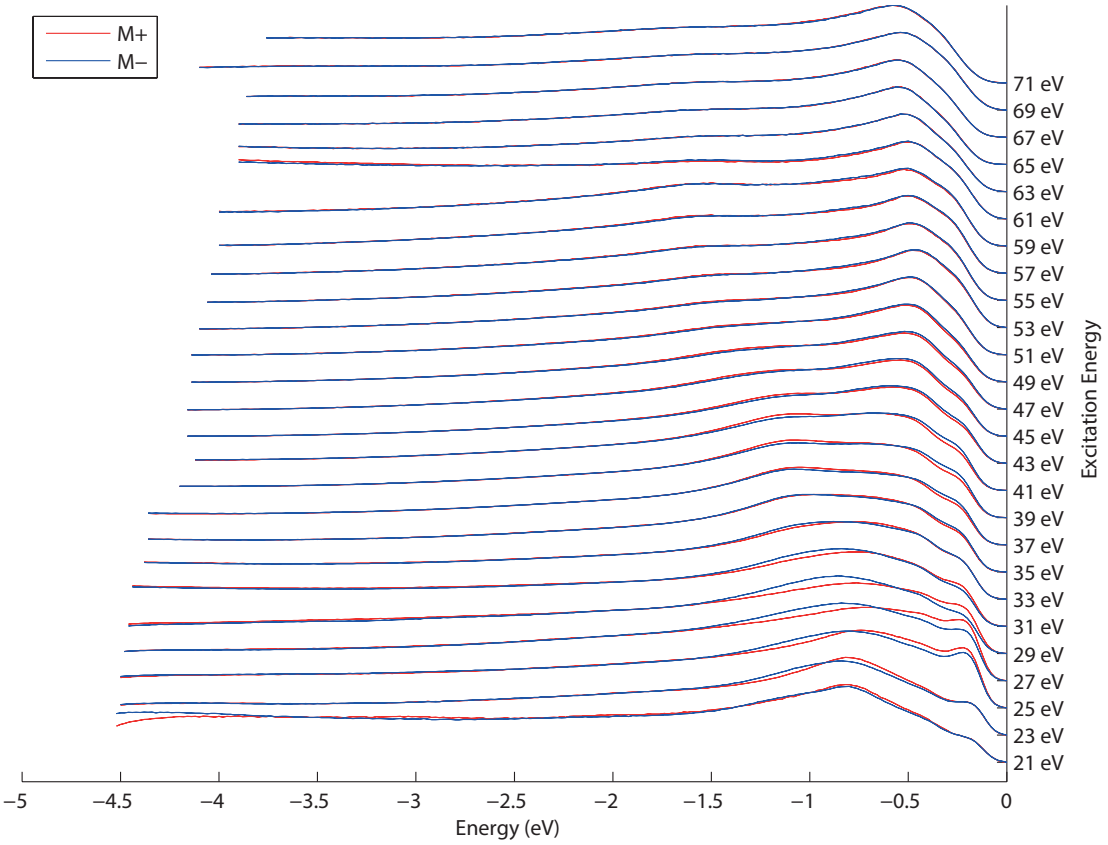

Figure 2: Valence band photoelectron spectra from a 8 ML thick hcp(0001) Co film on tungsten with linearly polarized light for opposite magnetization directions.

Another focus of our investigations are the angle-resolved spectra taken during these measurements. They show some interesting aspects, when compared to the Cobalt band structure, and it seems as if the asymmetry is far higher at some angles than at others. In the future we want to expand these measurements to even higher energies.

[1] J. Bansmann et al., Eur. Phys. J. D **9** (1999), 461 - 466
[2] J. Bansmann et al., Surf. Sci. 454-456 (2000), 686-691

Automatized PEEM measurements at the PGM Beamline 11 using the novel, self-developed S.P.A.M.M. software

C. Keutner[1,2,*], U. Berges[1,2], C. Westphal[1,2]

[1] Experimentelle Physik I - Technische Universität Dortmund, Otto-Hahn-Str. 4, D-44221 Dortmund
[2] DELTA - Technische Universität Dortmund, Maria-Goeppert-Mayer-Str. 2, D-44221 Dortmund
[*] corresponding author: christoph.keutner@tu-dortmund.de

The photoemission electron microscopy (PEEM) is a microscopic technique, which uses electrons emitted from an illuminated sample to generate a spatially resolved image of its surface. Depending on the characteristics of the photon source, PEEM can be used for spatially resolved x-ray absorption spectroscopy (XAS) with monochromatic light by scanning the light energy for each image of a sequence.

Up to now, the image acquisition as well as the tuning of the beamline to a specific photon energy are manual processes. Both processes require the intervention of an experimenter with sufficient experience with the beamline control system, especially for the last one. Since the typical acquisition time is in the range of up to a few minutes, this is a very work intensive and exhausting task for the experimenter, easily leading to errors. Therefore, a novel control software had to be developed which preforms these tasks autonomous.

Here, the challenge was combining the Open Source Experimental Physics and Industrial Control System (EPICS) [1], which is the basis of DELTA's control system, with the CCD camera's proprietary, strictly Windows-based driver and software. Fortunately, A. Edelstein et al. [2] from the UC San Francisco had already developed a powerful tool to control diverse cameras and optical microscopes called μManager [2], compatible with the PEEM's CCD. Based on ImageJ [3,4], which is already in use for processing the PEEM images and extracting spectra, μManager provides a very useful framework for Java applications. We use this framework to develop the software for PEEM-data acquisition with Micro-Manager (S.P.A.M.M.).

The simplified functionality of S.P.A.M.M. during the acquisition of images is displayed in Figure 1. The photon energy to set is calculated from the energy range and step width, which the user had entered before starting the scan. S.P.A.M.M. checks whether the energy range is compatible to the pre-set grating before starting the scan and reports an error if this not the case. Based on μManager and ImageJ, S.P.A.M.M. uses the Java interface of EPICS for stetting the PGM monochromator according to the required energy by adjusting the pitch of both the grating as well as the PGM's mirror. In order to maximize the photon flux at this energy, the permanent magnet undulator's gap (U55) has to be adjusted, too. Its new value is calculated by S.P.A.M.M. via a linear interpolation, using the gap range for the whole scan and the number of steps. The later one is calculated from the energy range and the energy step width. If the PGM and U55 are set to the new values, the beamline is ready to start the measurement.

S.P.A.M.M. then uses the CCD to acquire a previously user defined number of images with an also defined acquisition time per image. These images are saved individually under a user set name, extended by suffix indicating the used energy and consecutive number, if more than one image is acquired per energy. Simultaneously, the beamline flux[1] is measured by one

[1] Strictly spoken, these values are just measures for the flux. However, the normalization should remove the proportionality of the signal to the flux, hence a value proportional to the flux is sufficient for this task.

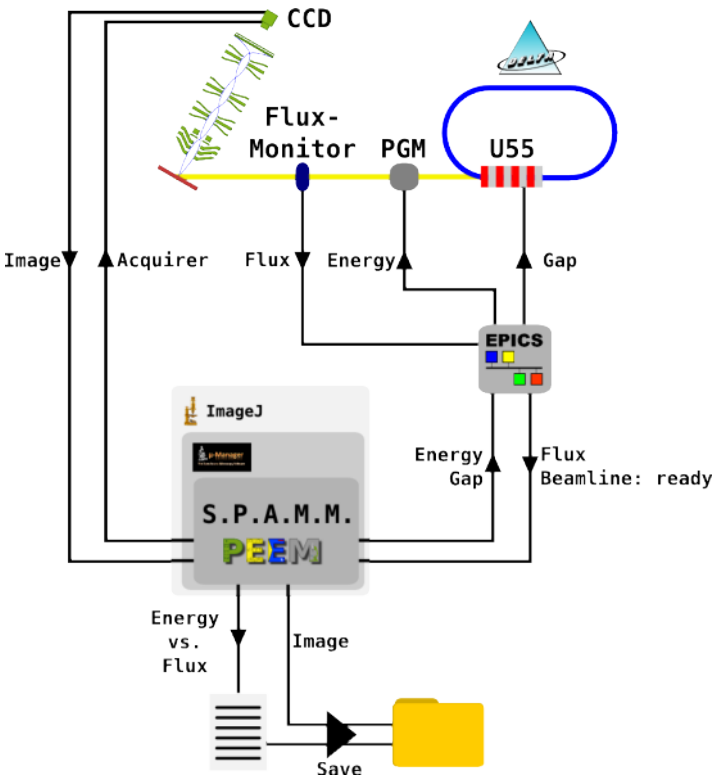

Figure 1: Chart illustrating the interaction of S.P.A.M.M. and the controlled devices.

of two Keithley channels, to be used for data normalization during the later analysis. These are normally obtained from the mirror current to the last beamline mirror, and the current to the last gold mesh, just in front of the experimental station. This flux is saved together with the photon energy in a text file, named identically as the entire scan and containing all energy-flux pairs. All these steps repeat till the entire energy range of the scan is gone through, or the scan is aborted by the user.

In conclusion, PEEM measurements at Bl 11 became much more convenient by using the S.P.A.M.M. control software. The experimenter just has to decide which flux monitor is to be used and has to enter the energy range, energy step width, and gap range. Scientists with much beamline experience are only necessary for determining whether the gap range is fitting to the energy range. Since these values are more and more documented, these scientists need not be present at the start of each scan, allowing users to work more freely, and setting beamline personal free for other tasks.

Acknowledgement

We would like to thank the DELTA-staff for their support.

References

[1] Experimental Physics and Industrial Control System (EPICS), http://www.aps.anl.gov/epics/ (2013).
[2] A. Edelstein, N. Amodaj, K. Hoover, R. Vale, and N. Stuurman, Current Protocols in Molecular Biology (2010).
[3] W. S. Rasband, ImageJ, U. S. National Institutes of Health, Bethesda, Maryland, USA, http://imagej.nih.gov/ ij/, (1997-2012).
[4] C. A. Schneider, W. S. Rasband, and K. W. Eliceiri, Nature Methods 9, 671-675, (2012).

BL10: Universities of Siegen and Wuppertal

Konstantin Istomin[1], Ralph Wagner[2], Anne Hüsecken[1], Stefan Balk[2] and D.Lützenkirchen-Hecht[2]
[1]Universität Siegen [2]Universität Wuppertal

Beamline 10 is a joint project of universities of Siegen and Wuppertal. Most of the beam time in 2013 was used by the researchers from both universities for their outgoing projects, as well as for educational purposes. Some weeks of operation were allocated also for external users. The beamline is devoted to materials science research with the focus on X-ray diffraction and absorption spectroscopy measurements, including:

1. Precise single crystal and powder diffraction
2. Fatigue studies in metals
3. Transmission and fluorescence EXAFS measurements
4. Reflection mode EXAFS, making use of the diffractometer

A new X-ray focussing capillary system will be installed soon, which will increase the photon flux to projected 5 x 10^9 Photons / s mm^2.

Several successful experiments have been already performed at the beamline.
One was an *in situ* measurement of fatigue effects in duplex (austenite/ferrite) stainless steel by the group from Siegen. The sample was fatigued with increasing stress amplitudes up to $8.17x10^7$ stress cycles, while mounted on the diffractometer. Fig 1 (left) shows a diffraction pattern in reflection geometry of a fatigued sample after $8x10^7$ cycles with a maximum stress amplitude of 390 MPa recorded with the Pilatus 2D detector. The pattern shows spots indexed for austenite (A) and ferrite (F) reflections. The penetration depth at 15 keV amounts to few µm focussing on the most damaged sample region. Although the sample is illuminated with a beam of about 0.5x0.5 mm^2, individual diffraction spots appear allowing for grain resolved analysis. The data evaluation is under way.

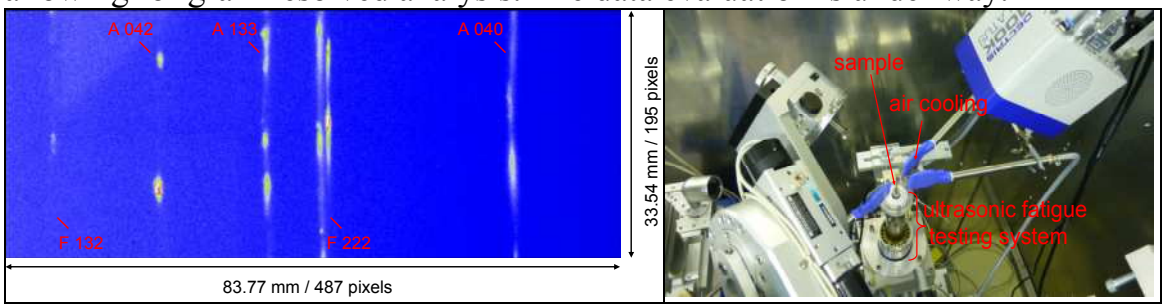

Fig. 1: Diffraction pattern of a fatigued duplex stainless steel sample (left). Experimental setup (right).

Another experiment was a study of austenitic-martensitic steel. Scope of the research was the investigation of the transformation paths (Gamma-Epsilon-Sigma or Gamma-Sigma) of a metastable austenitic stainless steel by means of quantitative phase analysis. For this purpose samples were strained plastically at low temperatures and then prepared for the investigations. The formation of the ε-martensite phase is highly localized and the very low volume fraction makes the usage of high energy X-Ray diffraction indispensable. Preliminary experiments show for the considered material, that a deformation of 15% at -40°C leads to the formation of an intermediate ε-martensite phase (Fig. 2).

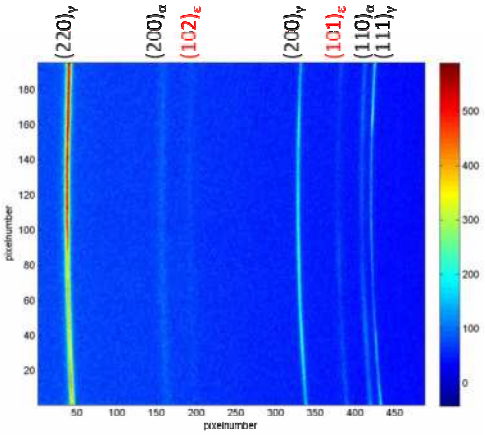

Fig. 2: Diffraction pattern of an austenitic stainless steel with the evident additional ε – martensite phase.

Besides the use for diffraction experiments the beamline has been a reliable instrument for several x-ray absorption measurements so far, some of which are part of this collection of reports. Here we show another application as a combination of diffraction and absorption techniques through site specific absorption spectroscopy also called diffraction anomalous fine structure DAFS. In this case the (400)-diffraction peak of a powder sample of Co_3O_4 has been continuously integrated while scanning the x-ray energy around the Co K-edge. The diffracted signal was detected by the before mentioned area-detector as one image per energy value. A plot of the measurement is shown in Figure 3. This way it is possible to investigate the atomic structure of Co for only one specific set of crystallographic planes or from a mixture of phases.

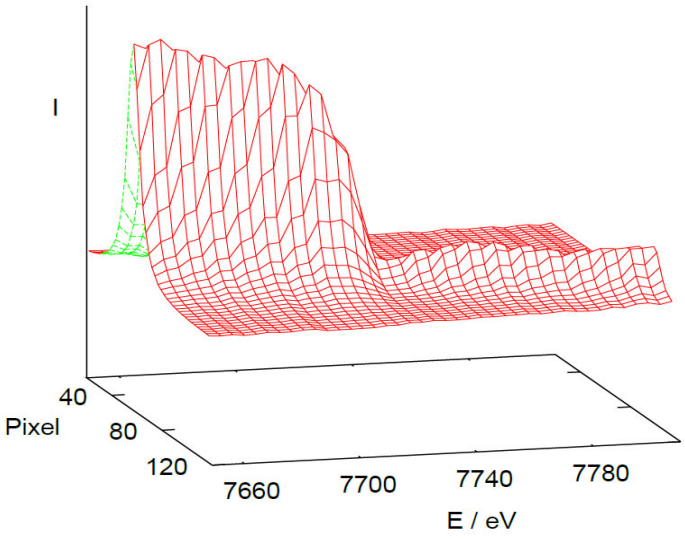

Fig. 3: Diffraction patterns of a Co_3O_4-sample for different photon energies in the region of the Co K-edge. The substantial decrease in diffracted intensity above the edge is clearly detectable, as well as the modulation in the edge and the post-edge region.

High resolution EXAFS experiments at DELTA BL10

D. Lützenkirchen-Hecht, R. Wagner, R. Frahm

Fachbereich C-Physik, Bergische Universität Wuppertal, Gaußstr. 20, 42097 Wuppertal, Germany

Synchrotron based hard X-ray probes are widely used for structure-related studies in materials science, physics, chemistry and biology, and there is an increasing demand especially for X-ray absorption spectroscopic experiments, where the energy dependence of the absorption coefficient is measured in the vicinity and above an absorption edge of an element of interest. In order to increase X-ray related research activities and to meet the user needs for high energy photons, a new hard X-ray beamline BL10 was installed at the DELTA storage ring. The new beamline is designed for X-ray absorption spectroscopy, diffraction measurements and surface sensitive X-ray reflectivity experiments in the energy range between ca. 4 keV and 16 keV (ca. 3.1 – 0.7 Å) making use of the intense radiation emitted by a superconducting wiggler. There are already two hard X-ray beamlines installed at this wiggler [1, 2], but the broad radiation fan covering about ± 25 mrad horizontal beam divergence allowed the installation of a third beamline at this insertion device, however with a strongly limited space. Thus a rather simple X-ray optical layout had to be used because there is no space available e.g. for collimating mirrors, and a simple channel-cut crystal has to be used as monochromator. In the following, we briefly describe the results of the first systematic X-ray absorption spectroscopy experiments performed at BL10.

For those experiments, different metal (reference) foils were investigatd in the transmission geometry making use of ionization chambers as detectors for the incident and the transmitted intensities. Due to the lack of space especially for the monochromator, currently no angular encoder is installed and thus the resolution of the monochromator and the repeatability were investigated. For this purpose, the energy scale of the monochromator was determined from repeated measurements of the Au L_3-edge. In between the spectra, large energy scans over several keV have been performed, so that the precision of the monochromator can be judged. Results are presented in Fig. 1. As can be seen, the edge position as determined by a fit of the maximum in the first derivative of the Au L_3-edge spectra differs by less than 0.1 eV from spectrum to spectrum, with a mean value of 11919.22 ± 0.02 eV as indicated by the dashed lines in the inset of Fig. 1. The difference between the largest and the smallest values measured amounts to 0.06 eV only.

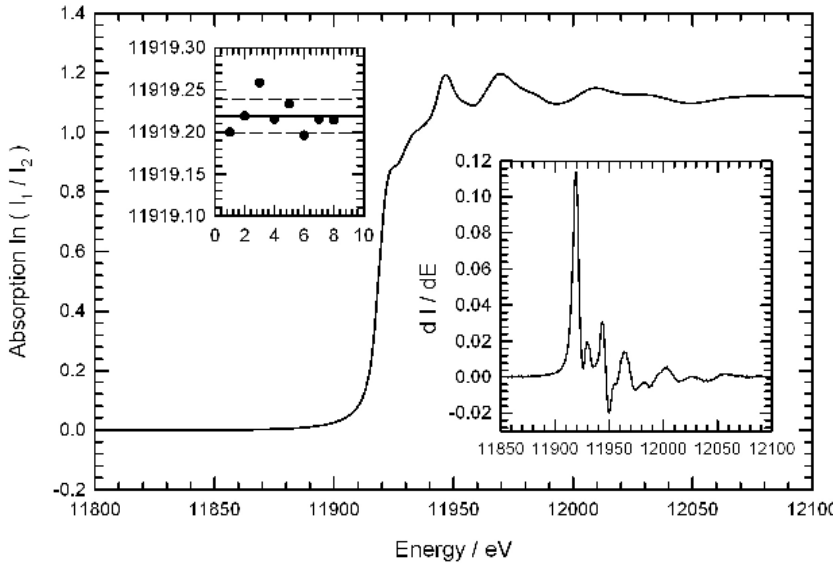

Fig. 1:
Precision, accuracy and repeatability of the BL10 channel-cut monochromator as determined from repeated measurements of the Au L_3-edge of a gold metal foil. In the inserts, a derivative spectrum and the determined edge positions are presented.

Furthermore, EXAFS spectra covering several 100 eV above the absorption edges were measured. As can be seen in Fig.2, high quality data comparable to those obtained at well-established EXAFS beamlines can be obtained within moderate measurement times of about 30-40 minutes for each spectrum. In conclusion, thus, BL10 represents an attractive instruments for EXAFS studies with hard X-rays and the first user experiments have already been performed at this beamline.

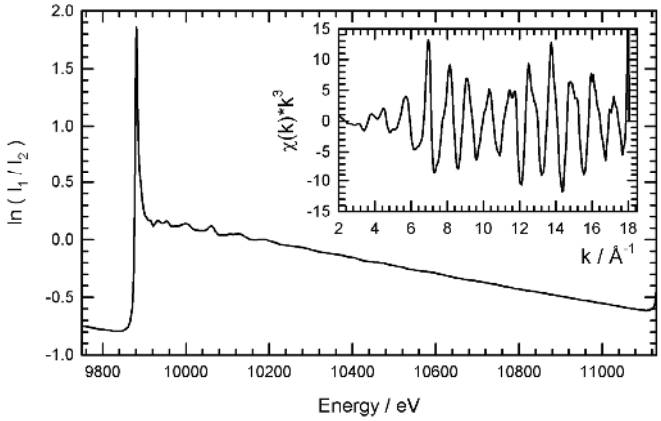

Fig. 2:
(a) X-ray absorption spectrum of a Ta metal foil at the Ta L_3-edge. The intense white-line feature as well as the EXAFS oscillations are well resolved. At 11200 eV (i.e. more than 1300 eV above the L_3-absorption edge), the onset of the Ta L_2-absorption limits the energy range for the current experiment.

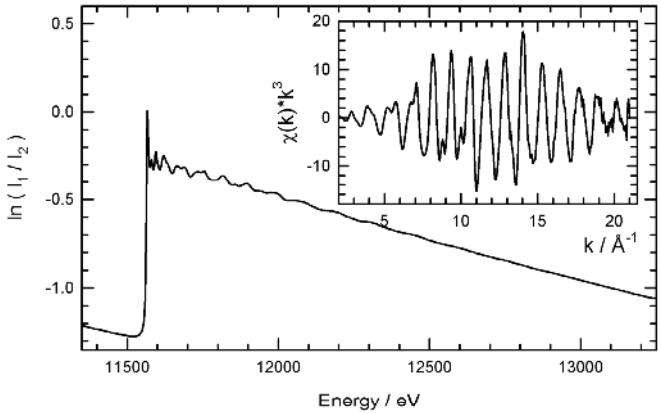

(b) X-ray absorption spectrum of a Pt metal foil at the Pt L_3-edge. The EXAFS oscillations are measured up to the onset of the Pt L_2-absorption edge at 13273 eV. In the inset, the k^3-weighted fine structure oscillations $\chi(k) * k^3$ are depicted, revealing almost noise-free data up to 20 $Å^{-1}$.

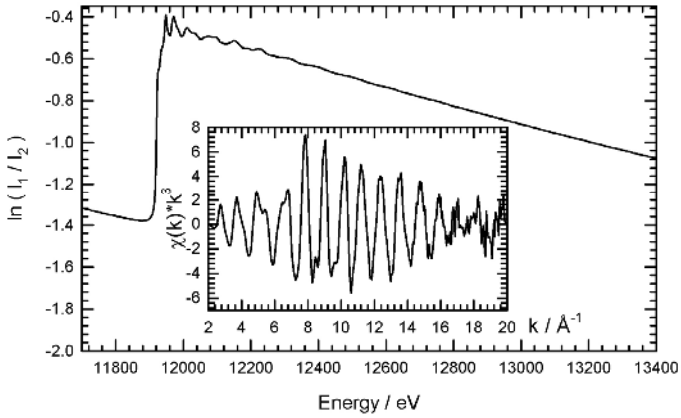

(c) X-ray absorption spectrum of a Gold metal foil at the Au L_3-edge. Again, almost noise-free $\chi(k) * k^3$ could be measured up to 17 $Å^{-1}$.

References

[1] Krywka, C., Paulus, M., Sternemann, C., Volmer, M., Remhof, A., Nowak, G., Nefedov, A., Pöter, B., Spiegel, M., and Tolan, M. (2006) J. Synchrotron Rad. 13, 8 – 13.

[2] Lützenkirchen-Hecht, D., Wagner, R., Haake, U., Watenphul, A., Frahm, R. (2009) J. Synchrotron Rad. 16, 264 – 272.

Investigations at the solid-liquid interface under high hydrostatic pressures

F. J. Wirkert*, M. Paulus, J. Nase, M. Kampmann, S. Kujawski, J. Möller, P. Salmen, C. Sternemann, J. Verwohlt, M. Tolan

Fakultät Physik/DELTA, TU Dortmund, 44221 Dortmund, Germany

*email: florian.wirkert@tu-dortmund.de

The application of pressure on matter is a powerful tool to study phase transitions and phase separations. Furthermore, understanding the nature of surfaces and interfaces is of great interest since many biological reactions occur only at interfaces. To examine the properties of interfaces X-ray reflectometry has proven to be well suited. Here we report on the first experiments with the new sample setup for reflectivity measurements at the solid-liquid interface under high hydrostatic pressure. An insight in the functional principle and the first results will be given.

Scientific background

Surfaces and interfaces are present in every lifeform. They are important for many biological and chemical reactions and thus of great interest for biomaterial science [1, 2]. In this study we concentrate on the solid-liquid interface and its properties under high hydrostatic pressure (HHP) conditions. The investigation of biomaterials using HHP has become very common in recent years. As experimental technique we use X-ray reflectometry, because of its potential to reliably resolve thin layer structures at buried interfaces [3]. With this new setup we are now able to perform X-ray reflectivity measurements under HHP conditions.

In our first experiment we wanted to study the pressure dependent protein adsorption at the solid-liquid interface. It is already known that protein adsorption can be triggered by temperature [4], and we wanted to investigate if it is also sensitive on HHP. We used silicon wafers with a functionalized surface. The wafers were coated with a self assembled monolayer of Trichloro-octadecyl-silane (OTS) in order to become hydrophobic.

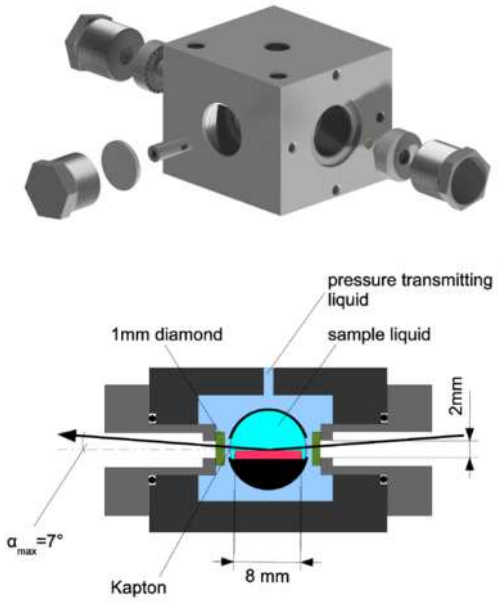

Figure 1: Schematic drawing of the outer sample cell.

Experimental setup

The experiments were carried out at beamline BL9. In reflectivity measurements the intensity of the reflected beam is detected in dependence of the wave vector transfer q_Z perpendicular to the samples surface. In the lower part of figure 1 a scetch of the measurement geometry is given. The cell (upper part of figure 1) is a modification of a cell which is already in use, it was originally designed by C. Krywka for small angle X-ray scattering experiments [6]. In order to separate the sample volume from the pressure transmitting liquid, which in our case is water, a two cell design is used.

Figure 2: The inner sample cell.

The outer cell is made of high-strength steel, a special nickel alloy, because it needs to resist the high pressures. For beam entry and exit diamond windows (thickness 1mm, diameter 6mm) are used. These windows guarentee for the HHP stability while cutting off as little intensity as possible. A third opening on the side of the cell allows a quick sample exchange without removing the windows. On the opposite side and on the top side of the cell drillings for the connection of the high pressure pump and the pressure sensor are present. A tubular system inside the cell can be flushed with a liquid to ensure a stable temperature. With this cell pressures of up to 5 kbar can be realized.

The inner sample cell is shown in figure 2. Wafers with surface dimensions of $8\times8\,\mathrm{mm}^2$ can be fixed with a little grub screw. The tube sealing has a flexible membrane. That way HHP can be applied to the sample

liquid without damaging the kapton windows on the sample tube. These kapton windows are for beam entry and exit and separate the sample liquid from the pressure transmitting liquid without cutting off too much of the beam's intensity. The whole sample cell has a length of about 30 mm and can carry a liquid sample volume of about 300 µl. A more detailed description of the functional principle can be found in reference [7].

Results

The experiment was dedicated to the investigation of protein adsorption at a hydrophobic surface. In figure 3 the results for pressure driven protein adsorption are shown. We used lysozyme as a model protein with a concentration of 0.1 mg/ml in buffer solution. As a buffer BisTris was chosen because of its stability throughout the investigated pressure range. The pH value was set to 7. Since Lysozyme is a rather stable protein, a destabilizing salt was added to the solution, that way the point where the protein unfolds was expected to be between 1 kbar and 5 kbar. At the left-hand side of figure 3 the obtained reflectivity curves for 1 bar and 5 kbar are shown. The corresponding electron density profiles are shown at the right-hand side. One can see the structure of the solid surface with a silicon dioxide layer on top of the silicon substrate and the OTS monolayer bound to the silicon dioxide. At 1 bar (blue curve) a small layer of protein is visible on top of the solid surface. After the pressure is increased to 5 kbar an additional layer occurs (red dotted curve). Also, the pressure induced increase of the electron density of the liquid phase can be recognized when looking at the far right end of the curves. The region of low electron density between the solid surface and the protein layer is characteristic for such a sample system and is called hydrophobic gap [5].

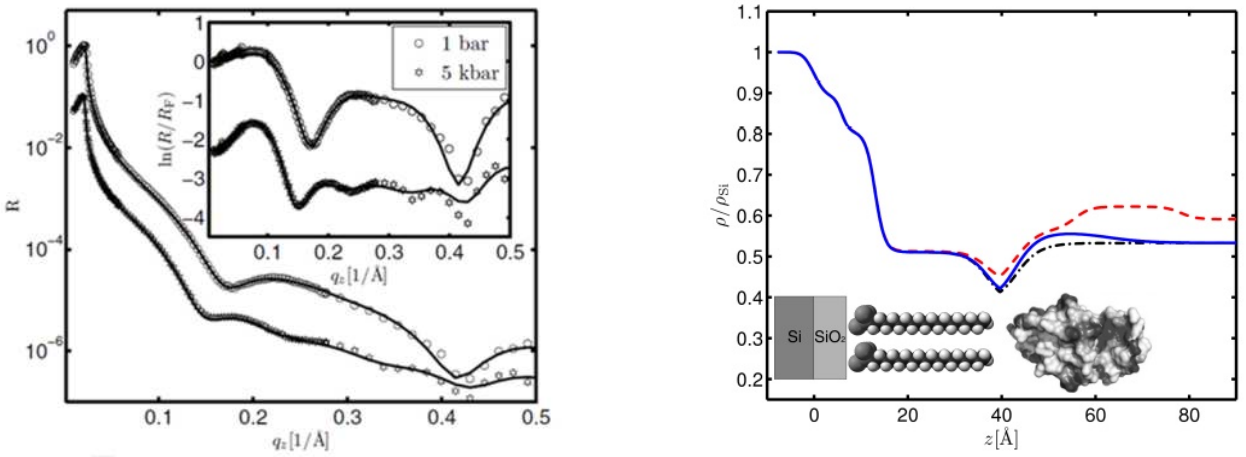

Figure 3: Reflectivity curves for the adsorption of lysozyme at a hydrophobic solid surface (left) with corresponding electron density profiles (right; blue: 1 bar, black: 1 bar with subtracted protein layer, red: 5 kbar)

The authors like to acknowledge the DELTA machine group for providing synchrotron radiation and technical support. The authors thank the NRW Forschungsschule, the BMBF (grant No. 05K10PEC) and the DFG (FOR1979) for financial support.

References

[1] D. G. Castner, B. D. Ratner, *Biomedical surface science: Foundations to frontiers*, Surface Science **500** (28-60), 2002

[2] B. Kasemo, *Biological surface science*, Surface Science **500** (656-677), 2002

[3] M. Tolan, *X-Ray Scattering from Soft-Matter Thin Films, Materials Science and Basic Research*, Springer-Verlag Berlin, 1999

[4] C. Czeslik et al., *Driving forces for the adsorption of enzymes at the water/silica interface studied by total internal reflection fluorescence spectroscopy and optical reflectometry*, Spectroscopy **16** (139-145), 2002

[5] M. Mezger et al., *On the Origin of the Hydrophobic Water Gap: An X-ray Reflectivity and MD Simulation Study*, JACS **132** (6735-6741), 2010

[6] C. Krywka, *Effect of Osmolytes on Pressure-Induced Unfolding of Proteins: A High-Pressure SAXS Study*, ChemPhysChem **9** (2809-2815), 2008

[7] F. J. Wirkert et al., *X-ray reflectivity measurements of liquid/solid interfaces under high hydrostatic pressure conditions*, J. Synchrotron Rad. **21** (doi:10.1107/S1600577513021516), 2014

Soft X-ray Spectroscopy

A photoelectron diffraction study of the Fe/GaAs(4×2)-interface

D. Handschak, F. Schönbohm, T. Lühr, C. Keutner, U. Berges, and C. Westphal
Experimentelle Physik I and DELTA - TU Dortmund, D-44221 Dortmund, Germany

November 2013

In this study we investigate a system of a (4×2)-reconstructed GaAs(001) substrate with a Fe adsorbate. This system is applied in the field of spintronics, which use the GMR (giant magneto resistance) effect [1, 2]. Especially the interface between this two layers has a strong influence on the efficiency of the effect [3]. The method of x-ray photoelectron diffraction (XPD) is an excellent tool to investigate this system, because it is chemical and interface sensitive. The angle-resolved measurement yields structural information due to scattering and diffraction effects of the photoelectron [4]. In combination with high-resolution XPS spectra of the elements at the surface we get chemical and structure information. The synchrotron light of beamline 11 (DELTA) allows recording spectra in high resolution in order to investigate surface and interface structures by varying the photon energy. The GaAs substrate is found in a well ordered (4×2)-reconstruction structure. An analysis of the As 3d and Ga 3d core level XPD pattern reveals that this base structure is not destroyed due to the Fe deposition.

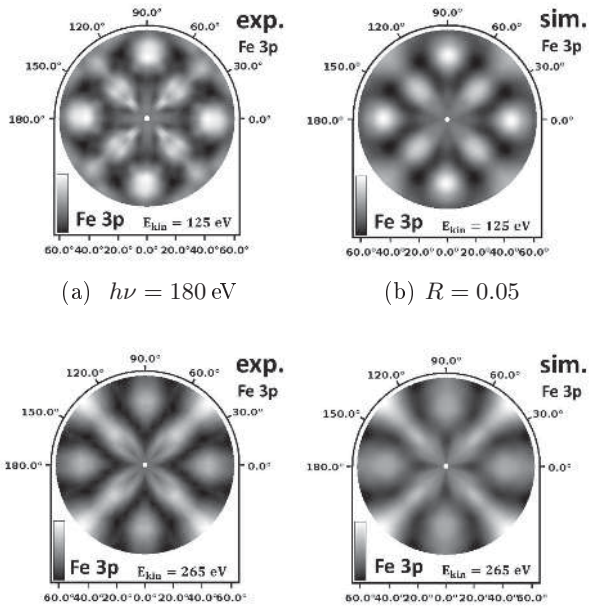

(a) $h\nu = 180\,\mathrm{eV}$ (b) $R = 0.05$

(c) $h\nu = 320\,\mathrm{eV}$ (d) $R = 0.07$

Figure 1: Comparison of experimental and simulated Fe 3p XPD pattern.

By analysing two XPD pattern of Fe 3p signal detected with two different photon energies we

found that the Fe/GaAs interface is formed by a pyramid-like structure of the iron layers. The strongest lateral shift is located in the first Fe monolayer with regard to the GaAs-substrate and decreases evenly to zero with every additional layer towards the surface. Thereby, the topmost layers are well-ordered in a bcc structure with the iron lattice constant of $a_{Fe} = 2.866\,\text{Å}$ [5].

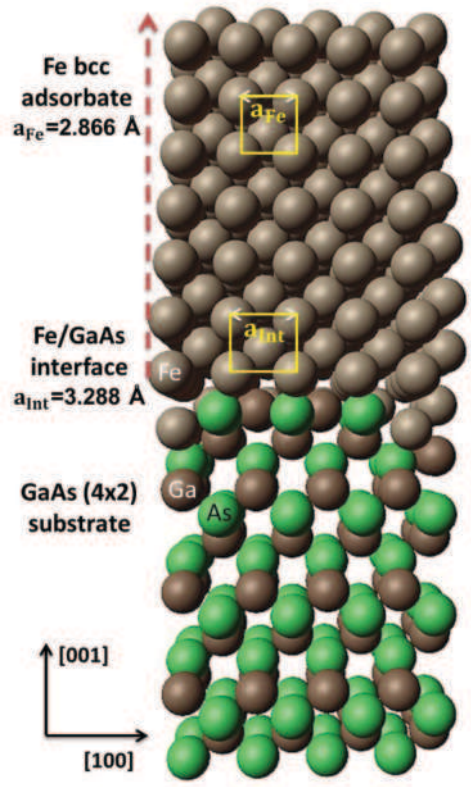

Figure 2: Schematic illustration of the Fe/GaAs(4×2)-structure model.

A schematic model of this interface structure is illustrated in Fig. 2 and is supported by the very low R-factors obtained within a comparison of experimental and simulated XPD pattern based on this model.

References

[1] M. N. Baibich, J. M. Broto, A. Fert, F. Nguyen Van Dau, F. Petroff, P. Etienne, G. Creuzet, A. Friederich, and J. Chazelas. Giant magnetoresistance of (001)fe/(001)cr magnetic superlattices. *Phys. Rev. Lett.*, **61**:2472–2475, 1988.

[2] G. Binasch, P. Grünberg, F. Saurenbach, and W. Zinn. Enhanced magnetoresistance in layered magnetic structures with antiferromagnetic interlayer exchange. *Phys. Rev. B*, **39**:4828–4830, 1989.

[3] Y. B. Xu, E. T. M. Kernohan, D. J. Freeland, A. Ercole, M. Tselepi, and J. A. C. Bland. Evolution of the ferromagnetic phase of ultrathin Fe films grown on GaAs(100)-4 × 6. *Phys. Rev. B*, **58**(2):890–896, 1998.

[4] C. Westphal. The study of the local atomic structure by means of x-ray photoelectron diffraction. *Surf. Sci. Rep.*, **50**(1), 2003.

[5] D. Handschak, T. Lühr, F. Schönbohm, S. Döring, C. Keutner, U. Berges, and C. Westphal. Structural investigation of the three-layer system mgo/fe/gaas(001) by means of photoelectron spectroscopy and diffraction. *Phys. Rev. B*, 88:045313, Jul 2013.

Magneto-Crystalline Anisotropy Detected by X-Ray Linear Dichroism in Reflection at the $L_{2,3}$ Edges of Fe

M. F. Tesch, C. Jansing, M. C. Gilbert, H.-Ch. Mertins, D. E. Bürgler[1] and C. M. Schneider[1,2]

Münster University of Applied Sciences, Stegerwaldstr. 39, D-48565 Steinfurt
[1] Forschungszentrum Jülich GmbH, Peter Grünberg Institut (PGI-6), D-52425 Jülich, [2] Fakultät f. Physik & Center for Nanointegration Duisburg-Essen (CeNIDE), Uni Duisburg-Essen, D-47048 Duisburg

Magneto-optical effects like the transversal magneto-optical Kerr-effect (T-MOKE) or the X-Ray magnetic circular dichroism (XMCD) are used as a powerful tool for the investigation of magnetic materials [1]. Because T-MOKE or XMCD are in lowest order linear in the magnetization they allow for the detection of ferromagnetic behavior. The X-ray magnetic linear dichroism (XMLD) belongs to a second class of magneto-optical effects which are quadratic in the magnetization [1], thus, allowing for the detection of antiferromagnetic order, something which is not possible by T-MOKE or XMCD [2]. Additionally, the XMLD effect is very sensitive to the crystal symmetry, especially to the magneto-crystalline anisotropy. Therefore it is suitable to obtain more information about the electronic structure than by T-MOKE or XMCD.

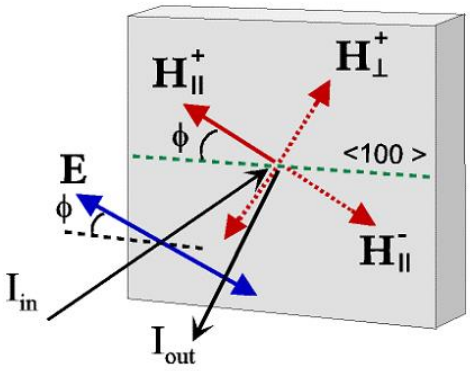

Fig 1: *Experimental geometry for XMLD measurements. (Details see text).*

First XMLD measurements at the Fe 2p edge [3] used total electron yield (TEY) technique to observe XMLD. TEY measurements with a strong applied magnetic field need a sophisticated experimental setup to avoid a disturbance of the measured photoelectrons by the varying magnetic field. Additionally only layers near the surface can be examined with TEY. To overcome these difficulties we performed for the first time XMLD in reflection (XMLD-R) measurements at the 2p edges of crystalline Fe using beamline 11 at DELTA. In contrast to the photon-in-electron-out method of TEY measurements the photon-in-photon-out detection method in XMLD-Reflection measurement geometry are unaffected by the applied magnetic field and allows also for the investigation of buried layers. In the experiment we used p-polarized light in near normal incidence. To overcome the low sample reflectivity in the Fe 2p region we used a photomultiplier tube in combination with a $Lu_3Al_5O_{12}:Ce$ phosphor screen to detect the reflected light. The sample was a 30 nm thin monocrystalline bcc Fe sample deposited by molecular beam epitaxy on a 150 nm Ag buffer layer on GaAs (001). To prevent oxidation the sample was capped with 3 nm Au.

The experimental geometry is shown in Fig. 1. The incoming linearly polarized light with an incident angle close to normal incidence (θ=85°) is reflected by the magnetized sample. The reflectance $R(H_{\perp}^{+}), R(H_{\parallel}^{+})$ is measured for two different applied fields, i.e $H_{\perp}^{+/-}$ for the magnetic field perpendicular to the polarization plane, i.e. the electric field vector *E,* and $H_{\parallel}^{+/-}$ for parallel orientation respectively to *E*. The varying magnetic fields $H_{//,\perp}^{+/-}$ can be applied by a fast switching compact magnetization device called *MiniMag* providing a magnetic flux density at the sample position of about *B* = 200 mT. For the experiments we used our new UHV-chamber "Extended MiniMag Apparatus" (E.M.M.A.). The angle ϕ of the electric field vector of the incoming linear polarized light and the

crystal axis can be tuned. For the magnetic easy axis <100> we set $\phi = 0°$ and for the magnetic medium hard <110> axis we set $\phi = 45°$.

The result are presented in Fig. 2. The top part shows the relative reflectivity of the sample. As expected resonantly enhanced reflectivity occurs at the Fe $2p_{3/2}$ edge near 715eV and at the $2p_{1/2}$ edge at about 730eV. The magnetization dependence is obtained from the corresponding asymmetry spectra. The T-MOKE asymmetry is plotted in the middle part of Fig. 2. It is deduced from the reflectance spectra as the normalized difference for the two opposite direction of the magnetic field perpendicular to the electric field of the light according to

$$A_{\text{T-MOKE}} = \frac{R(H_{\perp}^{+}) - R(H_{\perp}^{-})}{R(H_{\perp}^{+}) + R(H_{\perp}^{-})}.$$

Typical well pronounced structures are observed across the whole range from the $2p_{3/2}$ edge to the $2p_{1/2}$ edge. However, the dependence on the orientation of the crystalline axis is weak in T-MOKE spectra (red, black curves). Only a small difference appears at 715eV. In contrast the XMLD-R asymmetry spectra exhibit a strong dependence of the orientation between the crystal axis and the electric field vector of the polarized light. The XMLD-R asymmetry is deduced from the reflectance spectra (Fig. 2, top) by the normalized difference of the average reflectivity for the electric field oriented parallel and perpendicular to the electric field vector of the light, respectively, according to

$$A_{\text{XMLD-R}} = \frac{\left(R(H_{\parallel}^{+}) + R(H_{\parallel}^{-})\right) - \left(R(H_{\perp}^{+}) + R(H_{\perp}^{-})\right)}{\left(R(H_{\parallel}^{+}) + R(H_{\parallel}^{-})\right) + \left(R(H_{\perp}^{+}) + R(H_{\perp}^{-})\right)}.$$

The XMLD-R asymmetry (Fig.2, bottom) shows clear peaks at 715 eV, 719 eV and 728.5 eV for both, the magnetic easy and the magnetic medium axes (black, red curves). The strong dependence on the orientation of the crystal axes is found in the inversion of the two corresponding XMLD-R spectra at 719 eV and 728.5 eV. Only the peak at 715 eV is not changed. This is a striking demonstration of the applicability of the XMLD-R measurement method. In a next step these spectra will be used to verify band structure a*b-initio* calculation, done in cooperation with the University Uppsala (Sweden) and the Technical University Ostrava (Czech Republic). We acknowledge U. Berges, C. Keutner and D. Handschak for their support.

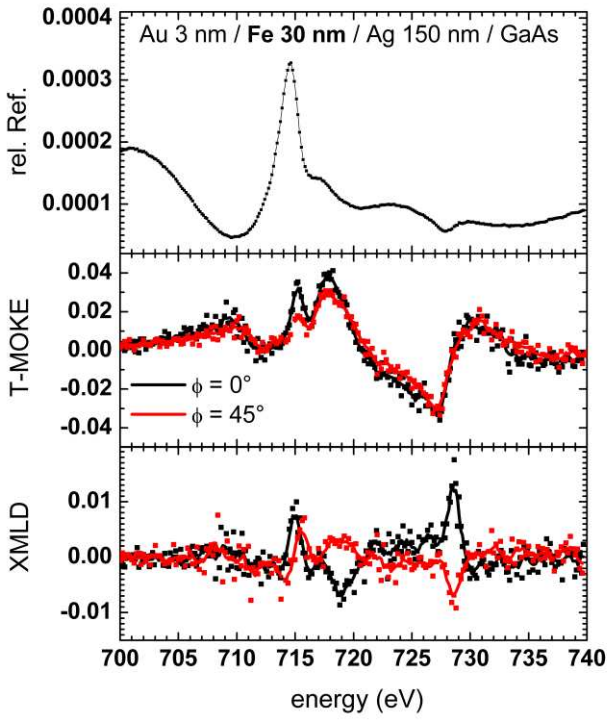

***Fig 2**: top: **r**elative reflectivity, middle: T-MOKE asymmetry, and XMLD asymmetry of a 30nm crystalline Fe film at near normal incidence for the easy axis <100> (black) and medium hard axis <110> (red).*

[1] J. Stöhr, H.C. Siegmann, *Magnetism*, Springer Series in Solid State Sciences, Berlin (2006)
[2] F. Nolting, D. Legut, J. Rusz et al., Phys. Rev. B **82**, 184415 (2010).
[3] J. Kuneš and P. M. Oppeneer, Phys. Rev. B **67**, 024431 (2003).

Grain size determination of multiphase steels via photoemission electron microscopy

P. Roese[1,2,*], C. Keutner[1,2], U. Berges[1,2], C. Westphal[1,2]

[1] Experimentelle Physik I - Technische Universität Dortmund, Otto-Hahn-Str. 4, D-44221 Dortmund
[2] DELTA - Technische Universität Dortmund, Maria-Goeppert-Mayer-Str. 2, D-44221 Dortmund
[*] corresponding author: peter.roese@gmx.de

Information about the steel composition can be used to assess characteristics of steel, like its formability. An important information for this assessment is the grain size. In order to gain more information on this grains, we performed experiments on two different steel alloys by using photoemission electron microscopy (PEEM). Therefore, the dual phase steel DP-K [1] and a retained austenite steel RA-K [2] were examined. Here, the photoelectric effect leads to an emission of electrons out of the steel. An electro-static lens system projects these electrons onto a fluorescent screen, yielding a image of the steel's surface.

The steels were provided by ThyssenKrupp Steel Europe AG. These multiple phase steels are mainly applied in modern automotive manufacturing for weight optimization. Further on, they can absorb a high amount of energy during deformation. These two properties are ideal for providing light weight and crash optimized car-body parts such as crash boxes or side rails.

The examined DP-K steel exhibits a high strength and good cold forming property as well as an excellent weldability. Furthermore, the RA-K retained austenite steel shows an even higher strength at stretching than the DP-K steel.

All samples were prepared by a new etching and polishing procedure [3].

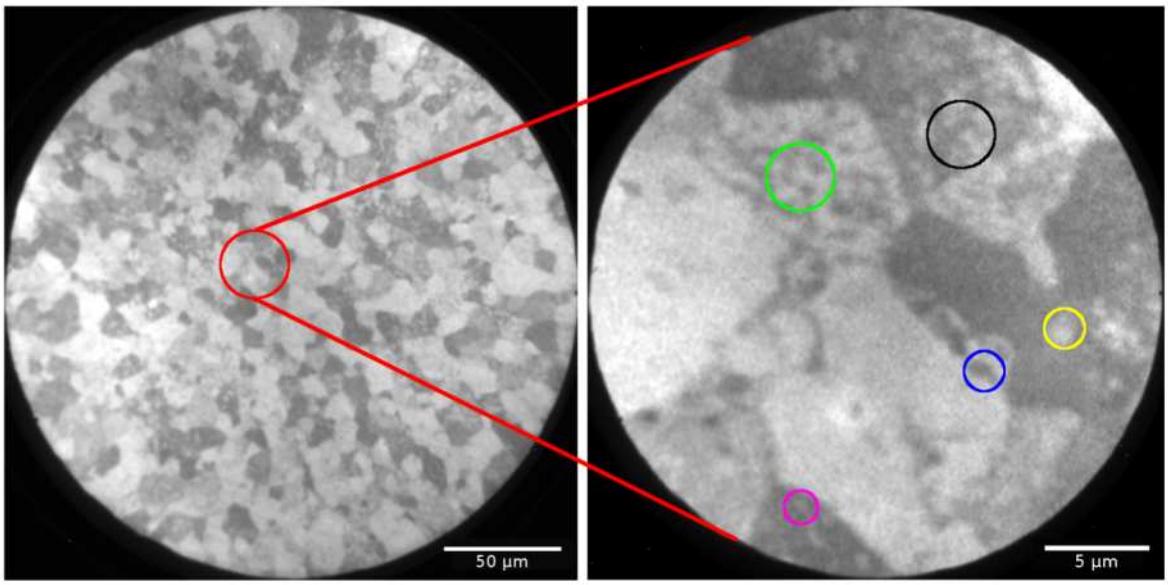

Figure 1: Left: Image of DP-K-steel, recorded via Hg-lamp. Right: Close-up view of the red area of the left image.

In these experiments two different light sources were used for photoemission excitation. Depending on the light source different contrast mechanisms can occur. On the one hand,

we used a Hg-lamp with a high resolution, utilizing mainly the work-function contrast. On the other hand, synchrotron radiation of DELTA was used. The achieved resolution by using synchrotron radiation is not as high as by using a Hg-lamp. However, synchrotron radiation can be used to examine the chemical composition of steel via energy dependent absorption.

Therefore, images recorded with the Hg-lamp were used to determine the grain size. An example for this can be seen in Figure 1. The image of DP-K steel shows areas with different grey levels, which point to differences in the chemical composition or to differences in the orientation of the crystals. These areas of different grey levels constitute the different grains of the steel. The grain sizes of the DP-K steel were about $10\,\mu m^2$. The images of RA-K steel look quite similar, hence they are not shown here. For this steel, grain sizes of $3\,\mu m^2$ could be determined.

Moreover, energy dependent absorption of steel probes were examined via synchrotron radiation of DELTA. Figure 2 shows energy dependent absorption of DP-K steel in areas of different grey levels. One can clearly see the absorption spectrum of iron. Nevertheless, these results did not allow inferences on other elements or iron compounds within the grains.

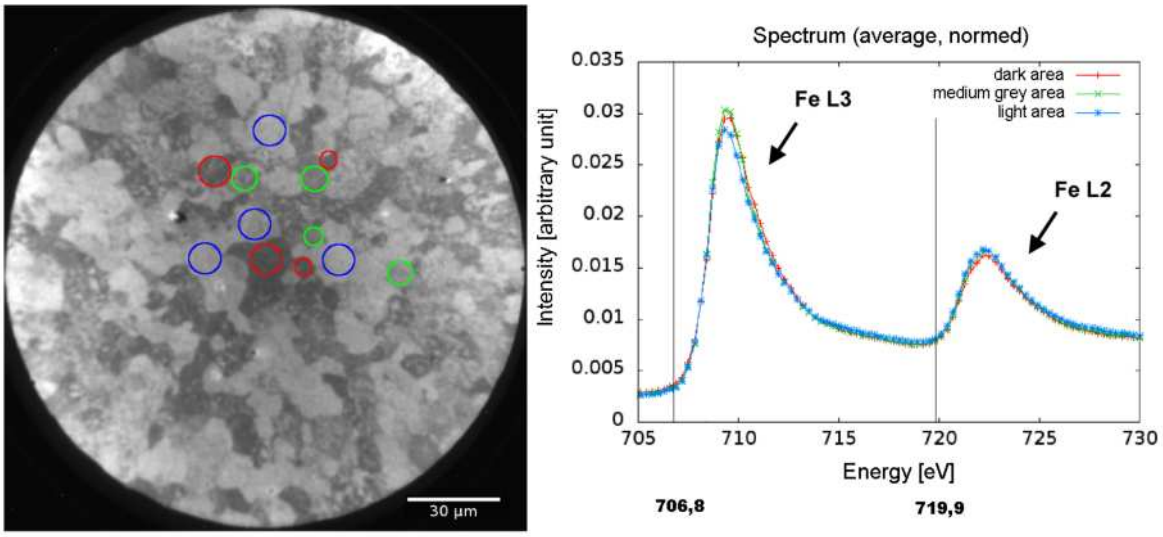

Figure 2: Left: image of DP-K steel. Right: absorption spectrum of the marked areas. One can see the absorption edges of iron Fe L_2 and Fe L_3.

Here, we could demonstrate the first steps toward a novel method of steel analysis. However, further efforts on enhancing the achievable resolution have to be developed, in order to access the grain boundaries with the primary differences in the composition.

Acknowledgement

We would like to thank the DELTA-staff for their support.

References

[1] Thyssen Krupp Stahl AG, *Dualphasen-Stähle DP-W und DP-K*, http://incar.thyssenkrupp.com/download/Broschueren/Dualphasen_Staehle_de.pdf (2009).

[2] Thyssen Krupp Stahl AG, *Restaustenit-Stähle RA-K*, http://incar.thyssenkrupp.com/download/Broschueren/Restaustenit_Staehle_de.pdf (2009).

[3] **P. Roese**, *Korngrössenbestimmung von Mehrphasenstählen mittels Photoemissionselektronenmikroskopie*, bachelor thesis, Technische Universität Dortmund (2013).

Thermal stability of thin HfO_2 films on Si(110)

F. Schönbohm[1,2,*], T. Lühr[1], D. Handschak[1], S. Döring[2], U. Berges[2], and C. Westphal[1,2]

[1] Experimentelle Physik 1 - Universität Dortmund, Otto-Hahn-Str. 4, D 44221 Dortmund, Germany
[2] DELTA - Universität Dortmund, Maria-Goeppert-Mayer-Str. 2, D 44227 Dortmund, Germany
[*] corresponding author: frank.schoenbohm@tu-dortmund.de

The temperature stability of ultra thin HfO_2 films on Si(110) surfaces was studied by means of x-ray photoelectron spectroscopy (XPS) and photoelectron diffraction (XPD). The HfO_2 films were grown by electron beam evaporation. Due to the evaporation process the silicon surface was oxidized forming a SiO_2 interface between the HfO_2 film and the Si(110) substrate. After evaporation the sample was stepwise annealed within the temperature range from 500°C up to 770°C. Fig. 1 a) and b) present the XPS spectra of the Si 2p and Hf 4f intensities recorded after the subsequent annealing steps. The signal of the Si 2p intensity is nearly constant up to annealing temperatures of 730°C, as shown in Fig. 1 a). After annealing at 770°C the silicon oxide components are completely removed while the Si 2p-bulk signal is increased.
In Fig. 1 b) the thermal development of the Hf 4f and the O 2s signals are presented. Up to an annealing temperature of 730°C the O 2s and Hf 4f signal intensities remain constant. After annealing at 770°C the O 2s intensity and the HfO_2 component of the Hf 4f signal are completely removed. In addition to that a new hafnium silicide component is formed on the sample. The $HfSi_2$ component is shifted by $\Delta E_{kin} \approx 3\,\mathrm{eV}$ to higher kinetic energies with respect to the HfO_2 signal. The new formed $HfSi_2$ component shows an asymmetric line shape compared to the line shape of HfO_2. This change is caused due to the transformation from an insulating HfO_2 film to metal-like $HfSi_2$. Therefore, the experimental spectra indicate a stable HfO_2 film for temperatures up to 730°C while oxygen was completely removed by an annealing at 770°C. SEM investigations showed that the new formed $HfSi_2$ is arranged in islands at the surface.

In order to investigate the internal atomic structure of the $HfSi_2$ islands an XPD pattern was recorded after annealing at 770°C. Fig. 2 a) shows an experimental XPD pattern of the Hf 4f signal recorded at a kinetic energy of $E_{kin} = 161.5\,\mathrm{eV}$. The pattern shows a twofold symmetry resulting from the twofold symmetry of the Si(110) substrate. For an quantitative structure analysis the experimental pattern had to be compared to a simulated pattern. As a start, the simulations were initialized with a known $HfSi_2$ structure obtained from literature. The structure was modified within a genetic algorithm in order to reduce and optimize the R-Factor. During the simulations it became clear that further adjustments to the structure had to be applied in order to optimize the agreement between experiment and the simulations. The local emitter environment contained Hf atoms which increased the R-Factor. Thus modifications of the structure were applied which resulted in a significant decrease of the R-Factor from $R \approx 0.130$ to a value of $R = 0.067$. Fig 2 b) compares the simulated diffraction pattern of the new structure with the experimental pattern of Fig 2 a). The pattern show a very good agreement since all main features displayed in the experimental pattern are presented in the simulated pattern, too. However, the simulated pattern contains a finer substructure which is not shown in the experimental pattern due to the limited angular experimental resolution.

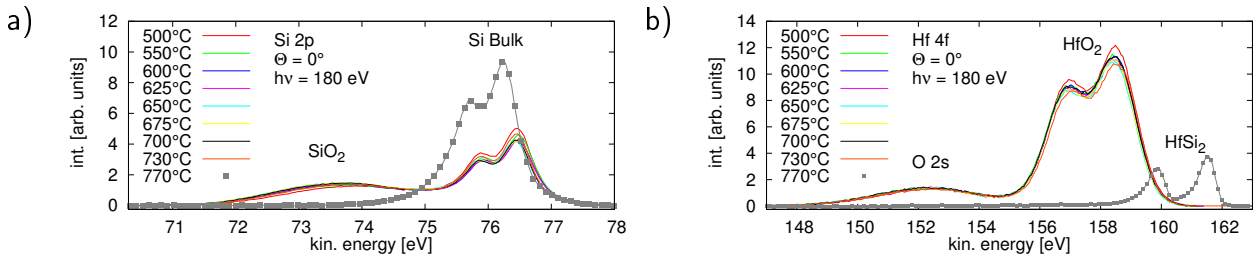

Figure 1: Si 2p a) and Hf 4f b) intensity as a function of temperature. For temperatures up to 730°C all spectra remain nearly constant. After annealing at 770°C spectra indicated by gray squares were recorded. Annealing at this temperature step removed any indication of oxygen from spectra, only Si and Hf signals were detected.

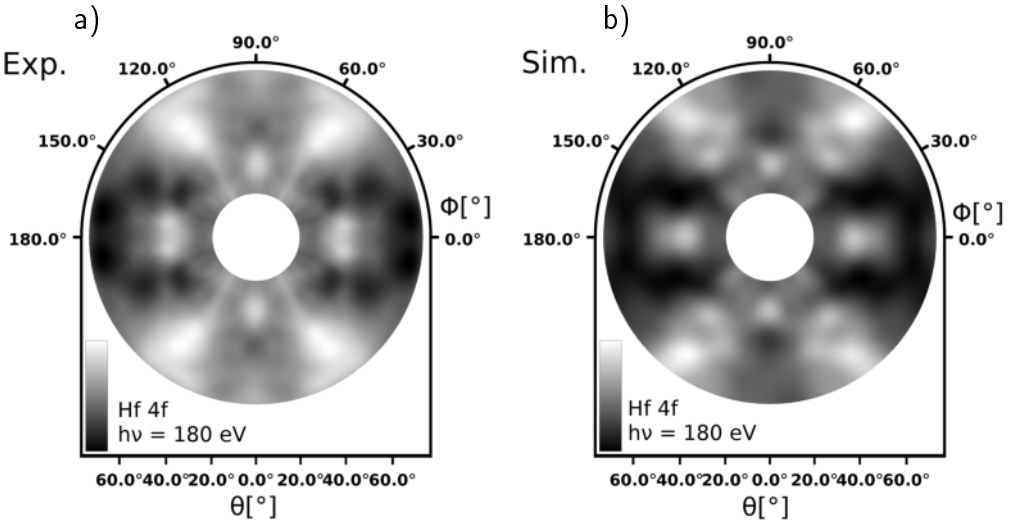

Figure 2: XPD pattern of the $HfSi_2$ islands on the Si(110) surface. The experimental pattern was recorded after annealing at 770°C a) and the simulated pattern was obtained for a modified C49 structure b).

Acknowledgments:
This work was supported by the Land Nordrhein-Westfalen, the NRW Forschungsschule and the Bundesministerium für Bildung and Forschung. Thanks go to the staff of DELTA for continuous support during the beamtimes.

X-ray Scattering

Strain in GaAs / (In,Ga)As core-shell nanowire heterostructures

A. Biermanns[1], E. Dimakis[2], L. Geelhaar[2] and U. Pietsch[1]

[1]Universität Siegen, Festkörperphysik, Walter-Flex Str. 3, 57072 Siegen
[2]Paul-Drude-Institut für Festkörperelektronik, Hausvogteiplatz 5–7, 10117 Berlin

The growth and synthesis of semiconductor nanowires (NWs) has attracted significant interest in recent years and meanwhile many technological applications have been demonstrated [Yang10]. Compared to thin film technology, the NW approach offers the possibility to form heterostructures between highly lattice-mismatched materials, because strain energy can be released at the NWs sidewalls without introducing defects in the bulk.
One possibility for the formation of heterostructures in the NW geometry is the growth of "core-shell" nanowires, in which a nanowire-core is surrounded by one or several different shells (Fig. 1). If the core and shell are composed of lattice-mismatched materials, mutual strain fields will be introduced in the system and depending on the mismatch and diameters of core and thickness of the shell(s), misfit dislocations can be introduced at the heterointerfaces, leading to a partial but spatially inhomogeneous relaxation of the system. Understanding the anisotropy of elastic interactions between core and shell and the relaxation mechanisms are crucial for device applications, as strain fields strongly affect the band structure and effective masses of the charge carriers.
Using beamline BL9 at DELTA, we have studied the strain-state of radial GaAs / (In,Ga)As core-shell nanowires, in which an (In,Ga)As quantum well (QW) is embedded within two GaAs layers (figure 1). The nanowires have been grown by molecular beam epitaxy (MBE) at the Paul Drude Institut für Festkörperelektronik, Berlin.

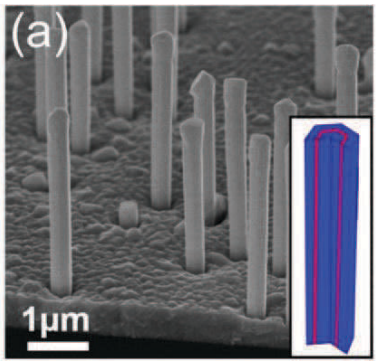

Figure 1:
Bird-eye-view SEM micrograph of (In,Ga)As/GaAs core-shell nanowires grown on Si(111). The inset shows a schematic of a core-shell nanowire in cross section, where the GaAs core (inner blue prism), the (In,Ga)As shell (red prismatic shell), and the GaAs cap shell (blue prismatic shell) can be distinguished.

The strain state of the same nanowires has been investigated using symmetric and asymmetric diffraction experiments in a coplanar geometry. The nanowires are grown along the [111] direction on a Silicon (111) surface, and the intensity distributions around the symmetric (111) as well as the asymmetric (422) reflections have been analysed. For the selected reflection, reciprocal space maps have been obtained using a 2dimensional Pilatus detector. Exemplarily, figure 2(a) shows line profiles through the GaAs (111) reflection for different QW thickness. With increasing QW thickness, we observe a continuous shift towards smaller momentum transfer of the diffraction maximum, from which an increasing tensile strain of up to 0.3% in the GaAs can be deduced. This trend is expected because the strain induced by lattice-mismatch is

shared between the GaAs core and the (In,Ga)As shell; and the thicker the shell, the more strain the core experiences. Exemplarily, fig. 2(b) shows a measurement around the asymmetric (422) reflection. The reciprocal space map shows the reflections of both Si substrate and the GaAs nanowires. Compared to the radial direction in reciprocal space (dashed line), the displacement of the GaAs reflection indicates a slight tetragonal distortion of the GaAs nanowires due to the (In,Ga)As quantum well. The results show that a detailed strain analysis is required in order to understand the emission properties and to investigate the limits of coherence within such heterostructures [Bie13].

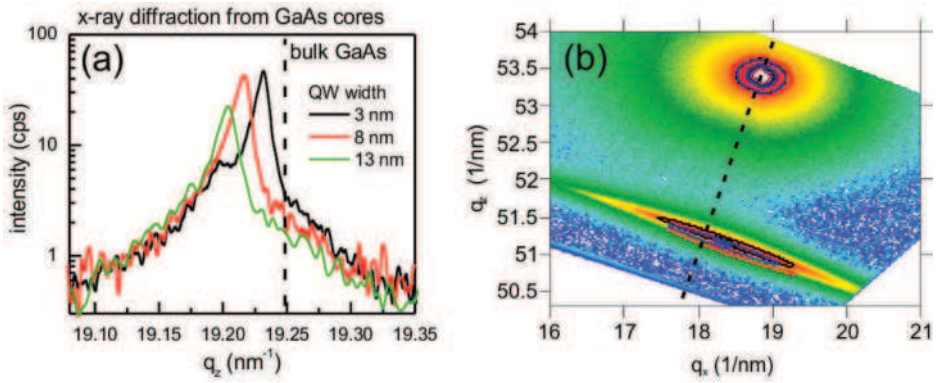

Figure 2: (a) XRD profiles through the (111) reflection of the GaAs nanowires, measuring an increasing axial tensile strain with increasing QW thickness. (b) reciprocal space map around the asymmetric (422) reflection. The upper reflection stems from the Si substrate. Dashed line indicates the radial direction in reciprocal space. The strain field in the NWs causes a tetragonal distortion of the NW lattice, leading to a displacement of the NW reflection from the radial line.

[Yang10] P. Yang, R. Yan and M. Fardy, NanoLetters **10**, 1529 (2010)

[Bie13] A. Biermanns, T. Rieger, G. Bussone, U. Pietsch, D. Grützmacher and M.I. Lepsa, *Applied Physics Letters* **102**, 043109 (2013)

Crystal structures of anhydrous rare earth metal nitrates $RE(NO_3)_3$ (RE = Sc, Lu) and acetates $RE(CH_3CO_2)_3$ (RE = Y, Sm – Er)

Ch. Heinrichs, U. Ruschewitz* and G. Meyer

Department für Chemie, Universität zu Köln, 50939 Köln, Germany
**email: uwe.ruschewitz@uni-koeln.de*

As no single crystals are available, the crystal structures of anhydrous rare earth metal nitrates and acetates were investigated by synchrotron powder diffraction at DELTA, Beamline 9 (BL09). All measurements were carried out at room temperature using the wavelength λ = 0.8157 Å (15.2 keV). Samples were sealed in capillaries of diameter 0.3 mm, 0.5 mm or 0.7 mm; a sample rotation was applied. The high resolution set-up with a scintillation counter was used for the measurements of "$Sc(NO_3)_3$", $Lu(NO_3)_3$, $Ho(CH_3CO_2)_3$ and $Y(CH_3CO_2)_3$. Additionally, for $Ho(CH_3CO_2)_3$ and $Y(CH_3CO_2)_3$ the new Pilatus detector was used to compare the quality of the measurements.

The XRPD pattern of "$Sc(NO_3)_3$" (**Fig. 1**) was indexed in a monoclinic unit cell with a = 8.5228(9) Å, b = 13.637(2) Å, c = 8.8254(9) Å and β = 119.287(5)°. The resulting unit cell volume is V = 894.6(2) $Å^3$ and $P2_1/c$ was found as a possible space group.[1] But despite the high-quality of the XRPD pattern no reasonable structure model could be developed using real space and direct methods (*ENDEAVOUR, FOX, EXPO*) until now.[1] One major problem is that the exact composition of "$Sc(NO_3)_3$" is not clear from elemental analysis.[1] Very recent investigations show that $Sc(NO_3)(OH)_2$ with Z = 10 might be the correct composition. New calculations based on this composition are on the way.

Due to strong absorption the quality of the XRPD pattern of $Lu(NO_3)_3$ (**Fig. 2**) does not have a comparable quality. The XRPD pattern was indexed in a monoclinic unit cell with a = 21.552(6) Å, b = 7.917(2) Å, c = 16.156(4) Å, β = 92.33(2)° and V = 2754(2) $Å^3$ with $I2/a$ being a possible space group (Z = 16). In the meantime new measurements have been performed at the ESRF (BM01b) using a shorter wavelength. Based on these measurements the crystal structure of $Lu(NO_3)_3$ was solved and refined.[1]

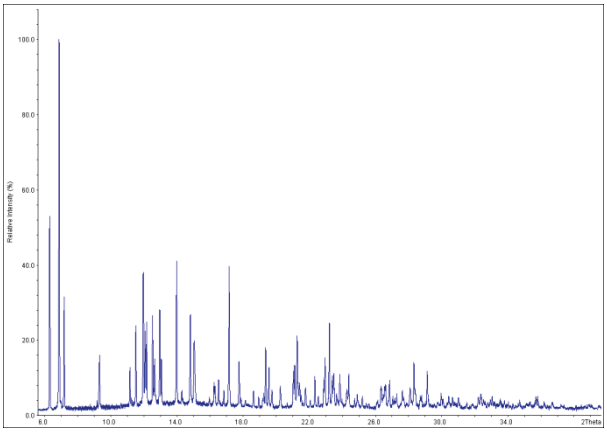

Figure 1: XRPD pattern of "$Sc(NO_3)_3$" (BL09, scintillation counter).

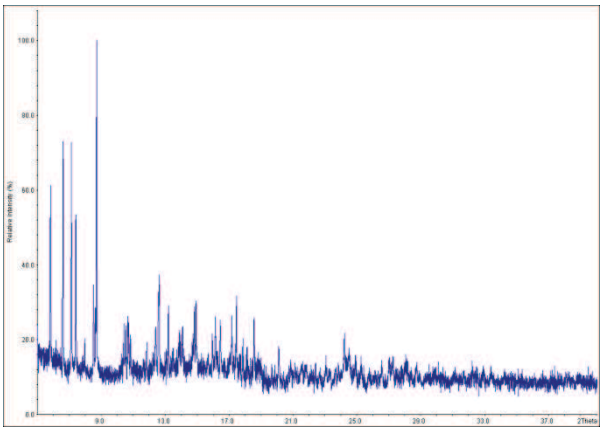

Figure 2: XRPD pattern of $Lu(NO_3)_3$ (BL09, scintillation counter).

In **Fig. 3** two XRPD patterns of $Y(CH_3CO_2)_3$ measured with a scintillation counter (blue) and the new Pilatus detector (red) are shown. Obviously, the resolution with the Pilatus detector is almost as good as with the scintillation counter. But with the new Pilatus detector the time for a measurement can be reduced from 6 – 8 h to only 1 h with almost comparable statistics. This leads the way for using the set-up with the Pilatus detector for temperature dependent measurements.

Similar XRPD patterns were obtained for $Ho(CH_3CO_2)_3$ and $Y(CH_3CO_2)_3$.[1] The XRPD patterns of $Y(CH_3CO_2)_3$/$Ho(CH_3CO_2)_3$ were indexed in orthorhombic unit cells with a = 8.212(2) Å/8.205(2) Å, b = 14.549(4) Å/14.546(2) Å and c = 7.848(3) Å/7.838(2) Å.[1] From the volume V = 937.7(6) $Å^3$/935.5(4) $Å^3$ Z = 4 was calculated. The reflection conditions reveal *Cccm* as a possible space group.[1] As Y^{3+} and Ho^{3+} have very similar ionic radii, the very similar cell parameters are not surprising and isostructural crystal structures are expected. In **Fig. 4** the electron density map of a structure solution of $Y(CH_3CO_2)_3$ (*Superflip*: charge flipping algorithm implemented in *JANA2006*) is shown.[1],[2] From these calculations the positions of the Y^{3+} cations are very clear, while the positions of the acetate anions are still somewhat uncertain. Nevertheless, an approximate structure model can be developed from these investigations.

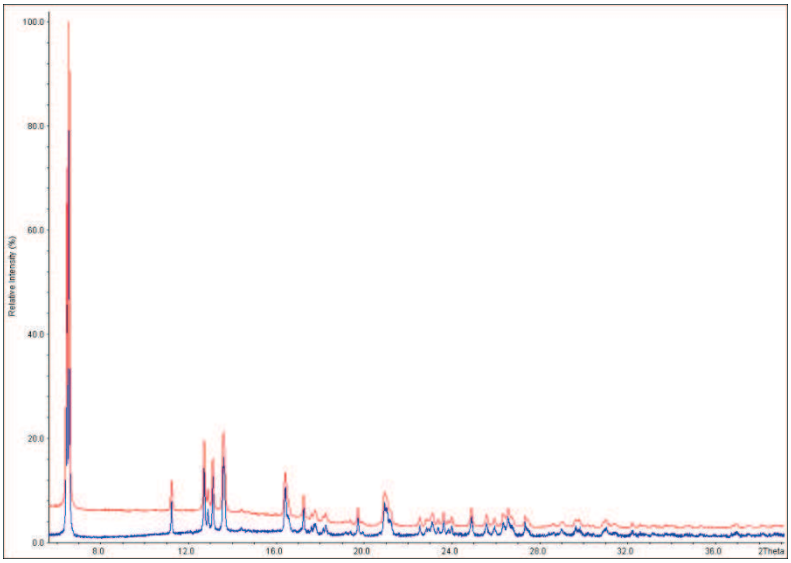

Figure 3: XRPD pattern of $Y(CH_3CO_2)_3$ (BL09, scintillation counter (blue) vs. Pilatus detector (red)).

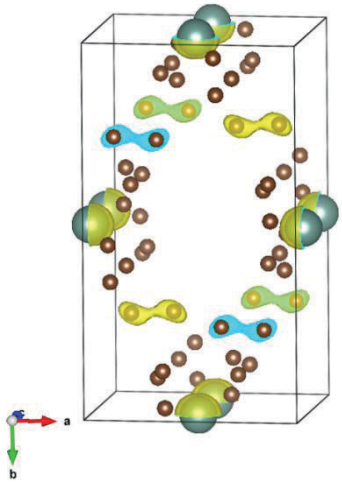

Figure 4: Electron density map of $Y(CH_3CO_2)_3$ (*Superflip*)[2].

References

[1] Ch. Heinrichs, *Synthese und Charakterisierung wasserfreier Seltenerdmetall-Nitrate, -Acetate und -Oxyacetate*, PhD thesis, Köln, **2013**, submitted.

[2] V. Petricek, M. Dusek, L. Palatinus, *JANA2006*. Institute of Physics, Academy of Sciences of the Czech Republic, Praha, **2006**.

DELTA User report 2013

Identification and characterization of unknown phases in thin film materials libraries of ternary systems

Proposer: Prof. Dr.-Ing. Alfred Ludwig
Co-proposers: Amin Janghorban, Sigurd Thienhaus, Hayo Brunken, Matthias Wambach, Sara Borhani Haghighi, Pio John Buenconsejo, Sven Hamann

Introduction

The scientific background of this investigation is combinatorial materials science for the discovery and development of new materials [1]. Ternary and quaternary systems are fabricated in the form of thin film materials libraries by combinatorial sputter deposition processes. We aim at identifying unknown intermetallic phases in ternary and quaternary systems as well as to understand how functional properties change with composition and structure. Synchrotron X-ray diffraction measurements are most suitable for combinatorial materials science as they allow the analysis of phases in thin film materials libraries with highest spatial resolution combined with short measurement times. The spatial resolution of our in-house automated XRD system is about 5 mm x 3 mm, which is only sufficient for primary screening, however to measure 342 compositions of a ternary system on a 100 mm diameter materials library takes at least 48 h. Therefore we can use the in-house system for the pre-characterisation of the materials libraries, whereas we used the synchrotron measurement time for detailed analysis, e.g. the precise identification of new phases. Complementary to the XRD characterisation we use resistivity mapping for identifying regions of interest on the materials libraries. These identified regions were characterised by the synchrotron measurements. We want to precisely identify the single phase regions, for this we need to be able to determine smallest amounts of precipitation phases that are not detectable using conventional X-ray diffraction techniques.

Experimental

Thin film materials libraries of various functional materials (Superalloy, Thermoelectric, Li-ion Battery and Shape Memory Alloys) were characterized in the BL09 station. The beam spot was reduced to 1 mm in order to obtain high spatial resolution. A glancing incident beam (at 5° incident angle) was used to reduce the appearance of the substrate on the diffracted spectra. The diffracted beams were recorded using a 2D-area detector and polycrystalline Si was used as calibration standard. Raw data were converted using fit2d software. To carry out high-throughput synchrotron diffraction experiment, the materials library was placed on top of an x-y-z stage. The system was programmed to automatically record sequentially different measurement regions within the travel distance limit of the x-y plane.

Summary of Results

High-Throughput Synchrotron Diffraction Experiment

Thin film SMAs are attractive for micro-sensor/actuator applications. In the Au-Cu-Al system an 18-carat gold jewelry known as `Spangold` ($Au_{45}Cu_{30}Al_{25}$, in at.%) and other limited composition variants were reported to exhibit the shape memory behavior. We investigated a wide composition range in this system by preparing 100 mm diameter Au-Cu-Al thin film materials library deposited on an oxidized Si substrate (**Fig. 1a**). We discovered that there are more compositions with shape memory properties (within the black dashed line boundary in **Fig. 1a**). In order to obtain high quality structure data high-throughput Synchrotron diffraction analysis of about 120 selected measurement regions were made. A sample XRD pattern from one of the measured regions in shown in **Fig. 1b**, revealing the coexistence of martensite (M) phase and precipitates. XRDsuite software was used to facilitate the visualization of large amount of diffraction patterns collected from the high-throughput Synchrotron diffraction experiment. This is made by plotting the intensity of a selected diffraction peak, which represents the phase, over composition. As an example the diffraction peak intensity distribution of (111)M martensite is shown in **Fig. 1c** where red, green and blue color gradient corresponds to high, medium and low peak intensity, respectively. Using this approach we were able to perform experiments on various libraries of functional materials, such as Superalloys, Thermoelectrics, Shape memory alloys and Li-ion Batteries. Two examples showing the advantage of using the Synchrotron diffraction facility over our in-house conventional XRD system are given below.

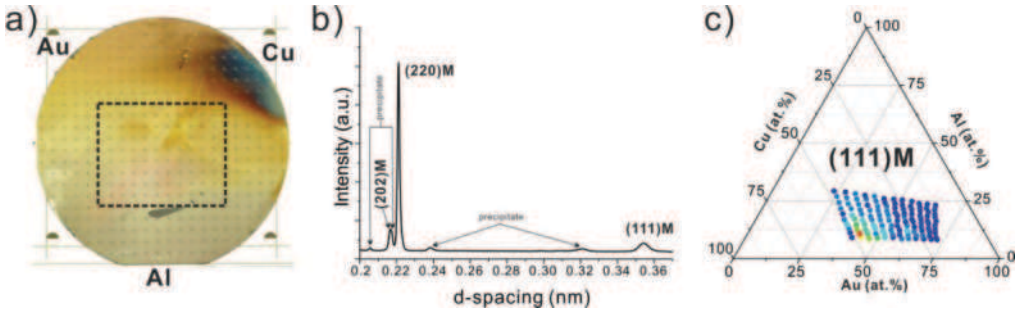

Fig. 1: (a) Au-Cu-Al materials library annealed at 500°C for 1h, (b) Synchrotron diffraction pattern taken at one of the measurement regions, and (c) peak intensity profile of (111)M martensite peak visualized using XRDsuite.

Au-Cu-Al Shape memory alloy (SMA)

The basis of SMA functional property is the reversible structure transformation between the parent phase (bcc or ordered B2/DO3/$L2_1$) and martensite phase (orthorhombic B19 or tetragonal BCT). Using a conventional XRD system (Philips Panalytical Xpert PRO, Cu-K_{α}) the patterns (**Fig. 2a**) revealed the martensite (M) phase and precipitate phase. The diffraction peak close to d-spacing = 0.215 nm is a convolution of the precipitate and (202)M peaks. In contrast, using Synchrotron radiation these peaks are clearly shown to be more separated (**Fig. 2b**) and the (220)M peak is visible. The c/a of the martensite can now be accurately measured, and this value has been shown to correlate very well with the functional properties. Data for the other compositions are currently being analyzed and will be used to support the explanation of interesting phenomena discovered in the Au-Cu-Al materials library.

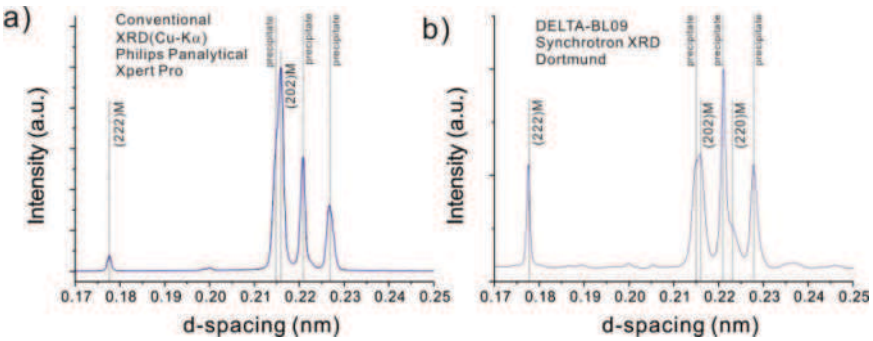

Fig. 2: Functional and structural properties of a new Au-Cu-Al SMA. (a) Electrical resistance measured during thermal cycle (blue-cooling, red-heating) showing the phase transformation characteristics. Structure characterization measured using (b) conventional XRD and (c) Synchrotron radiation.

Li-ion Battery

The structure and texture of thin film electrode materials plays a significant role in the battery performance and cycle life. $LiFePO_4$ has attracted a lot of attention as a cathode (positive electrode) material. The olivine structure of LFP allows one dimensional diffusion of Li ions. Therefore in a thin film cathode, comparison of a polycrystalline, non-textured film to a textured film becomes important. When the film is more randomly oriented a better probability of Li intercalation/de-intercalation exists. To study the electrochemical performance of these thin film cathode materials, a current collector is usually deposited prior to film deposition. In the sample studied here, a Si (100) single crystal coated with 1.5 µm of SiO_2 (as diffusion barrier) was used as substrate. 200 nm of Pt and 10 nm of Cr were deposited on top of the substrate as current collector and adhesion layer respectively. 200 nm of LFP was sputtered on top of the current collector and annealed ex-situ in O_2/N_2 i.e. dry air, mixture. From conventional XRD system (Philips Panalytical Xpert PRO, Cu-K_{α}), overlapping of some peaks from the Pt/Cr current collector and LFP thin film are observed (**Fig. 3a** and **3b**). This effect is eliminated when using Synchrotron radiation. Also peak splitting and peak shoulders of various planes which were not detected using the conventional XRD system are clearly shown and separated via synchrotron radiation (**Fig. 3c**). This phenomenon has significant importance when studying layered compounds with R-3m space group, where presence of peak splitting is an indication of formation of layered structure or basal distortions. This effect is the subject of future studies.

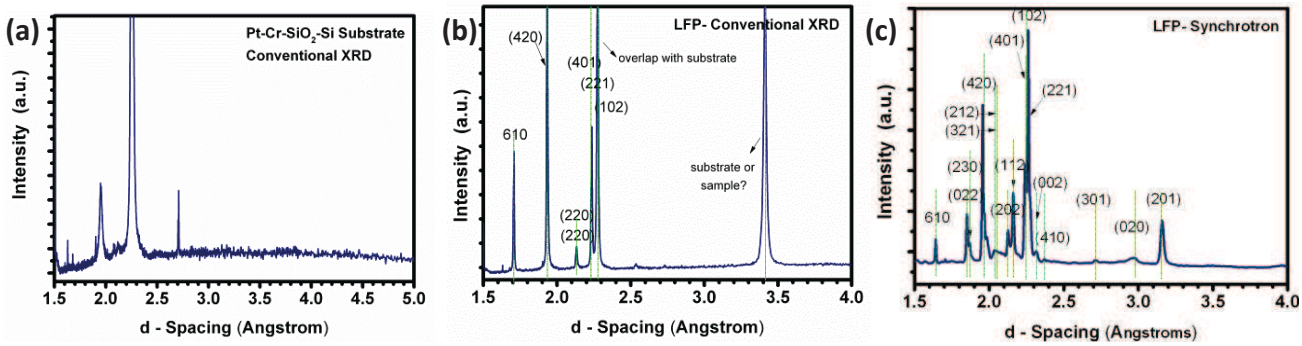

Fig. 3: Structural studies of 200 nm $LiFePO_4$ films on Pt/Cr/SiO_2/Si substrates (a) Conventional XRD spectrum of Pt/Cr/SiO_2/Si. Structure characterization of $LiFePO_4$ (b) conventional XRD and (c) Synchrotron radiation.

Reference

[1] A. Ludwig, R. Zarnetta, S. Hamann, A. Savan, S. Thienhaus (2008), Development of multifunctional thin films using high-throughput experimentation methods, International Journal of Materials Research 99 (10), 1144-1149.

Temperature and pressure dependence of the supramolecular structure of 2-Ethyl-1-hexanol and 4-Methyl-3-heptanol

T. Büning, C. Sternemann, C. Gainaru, M. Paulus, K. Mende, F. Wirkert, I. Kiesel, J. Möller, J. Nase, S. Bauer, R. Böhmer, M. Tolan

Fakultät Physik/DELTA, Technische Universität Dortmund, 44221 Dortmund, Germany.

Monohydroxy alcohols can be considered as the simplest organic hydrogen-bonded liquid. Hydrogen bondings are essential for the structure of e.g. alcohols, aqueous solutions and water. They play a major role for many biophysical and biochemical processes. Monohydroxy alcohols, like 2-Ethyl-1-hexanol (2E1h) and 4-Methyl-3-heptanol (4M3h) create supramolecular structures due to hydrogen bondings via OH groups. These structures strongly depend on the position of the OH group in 2E1h and 4M3h, which results in different dielectrical absorption strength in the MHz to GHz regime related to the so called Debye process [1]. In chain building monohydroxy alcohols, the single dipole moments are summed up which causes high absorption strength. In ring like supramolecular structures, single dipole moments almost annihilate each other and only a weak Debye process can be observed. The temperature and pressure dependent behavior of these structures is not completely understood [2,3]. Dielectrical experiments are sensitive to microscopic dynamics, but a direct measurement of structural arrangements on a molecular scale is not possible. To obtain information about changes in the supramolecular structure, wide angle x-ray scattering experiments were performed at the beamline BL 9 at DELTA, using a PILATUS detector for temperature dependent measurements and a MAR 345 detector for pressure dependent measurements.

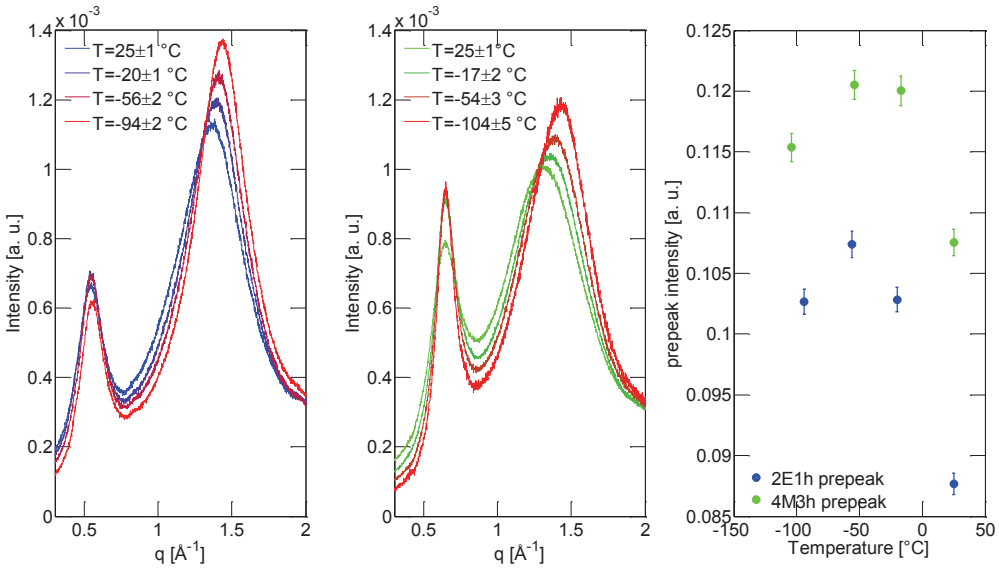

Fig. 1: Temperature dependent structure factor of 2E1h (left) and 4M3h (right) in the range from -94 °C/-104 °C to room temperature and the intensity of the prepeak plottet against temperature.

In figure 1, the temperature dependent structure factors of 2E1h and 4M3h are shown. The observed prepeak around $q \approx 0{,}6\ \text{Å}^{-1}$ can be correlated with typical intermolecular oxygen-oxygen distances arising from a separation of supramolecular structures by the carbon chains [4]. The effective length of the carbon chain in 4M3h is smaller than in 2E1h and thus, the prepeak is observed at larger wave vector transfer q. The main peak is related to the intermolecular carbon distances in the liquid and

can be observed for both alcohols at similar *q*. This means that the molecules are of similar size. The slightly different *q*-values of the main peaks position, arises from a different packing of the molecules due to the different position of the OH-groups. The carbon chains are closer packed and more parallel to each other in 2E1h. The shift of the main peak to higher *q*-values with decreasing temperature can be interpreted as a decrease of the distances between the molecules by thermal contraction. The integrated intensity of the prepeak increases in 2E1h and 4M3h with decreasing temperature until -25 °C, that indicates an increasing number of molecules in supramolecular arrangements [5]. An increase of the Debye process in 2E1h and a decrease of the alpha-process, which is due to the dipole moment of a single molecule, in 4M3h was found. Both is interpreted as an increase of the number of molecules in supramolecular arrangements [1,2,6]. At deeper temperatures the intensities seem to stay at a constant value, the dielectric measurements show minor changes as well. Further measurements for low temperatures are necessary to confirm these results.

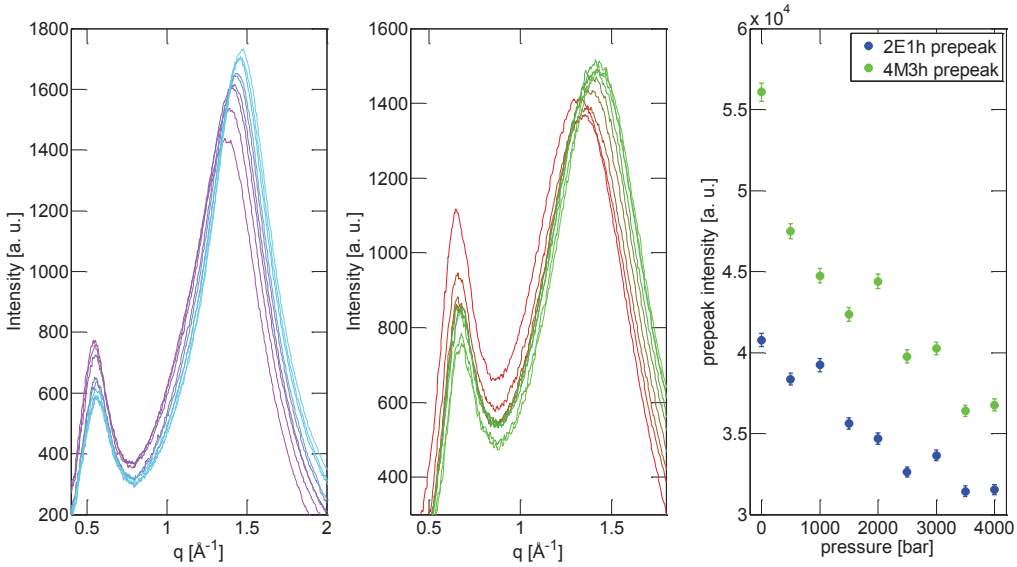

Fig. 2: Pressure dependent structure factor of 2E1h (left) and 4M3h (right). The pressure increases from 1 bar to 4000 bar in steps of 500 bar and the intensity of the prepeak plottet against pressure.

Applying pressure to the monohydroxy alcohols results in decreasing prepeak intensities in both alcohols, which indicates a break up of supramolecular structures. Dielectric measurements show a reduction of the Debye process in 2E1h and an increase of the Debye process in 4M3h which is interpreted as an increase of small chainlike structures consisting of two or three molecules [7]. We conclude that the chains in 2E1h are getting shorter and the ring-like structures in 4M3h are breaking up into ring fragments with larger effective dipole moment.

[1] C. Gainaru et al.: Broadband mechanical spectroscopy reveals that monohydroxy alcohols are singly hydrogen bonded supramolecular polymers, 2013.
[2] S. Bauer, K. Burlafinger et al. J. Chem. Phys. 138(9):094505 2013.
[3] S. Pawlus, M. Wikarek et al. J. Chem. Phys. 103:064501, 2013.
[4] M. Tomsic, A. Jmnik et al. J. Phys. Chem. B, 111:1738-1751, 2006.
[5] A. Hedoux, Y. Guinet et al. J. Chem. Phys. 138:214506 2013.
[6] C. Gainaru: private Kommunikation, 2013.
[7] S. Pawlus, M. Wikarek et al. J. Chem. Phys. 103:064501, 2013.

We would like to thank the DELTA machine group for providing synchrotron radiation and technical support, Thomas Büning thanks the BMWF project 05K13PE2 for financial support, and we acknowledge the support by the cluster of excellence RESOLV.

Simultaneous structural and electrical characterization of Hex-5T-Hex oligothiophene thin films

Eduard Mikayelyan, Linda Grodd, Dr. Souren Grigorian and Prof. Ullrich Pietsch

-conjugated semiconducting oligomers are attracting attention due to the low cost processing methods and their high electrical conductivity. Conjugated polymers and oligomers are providing relatively high field effect mobility, excellent luminescence properties and are promising for applications as flexible displays, solar cells, etc. [1].

The GIXD experiment was realized in order to characterize as-prepared oligomer thin films. The Hex-5T-Hex oligomer consists of two hexyl groups attached to both sides of quinquethiophene backbone (Fig.1). It was found that 3-dimensional crystallization of Hex-5T-Hex oligomer follows the 2-dimensional crystallization of 5T based oligomer self-assembled monolayer (SAM), that is the reflections (010), (020) and (120) (Fig.2a) in the in-plane direction are well pronounced and fit to reflections found for 2d crystallization of SAMs [1,2]. The peaks along the out-of-plane direction correspond to a spacing which is larger than one full molecule length (Fig.2b). Two orthorhombic unit cells were suggested in order to explain the 3d crystallization of Hex-5T-Hex oligomer.

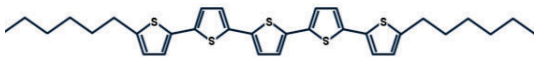

Figure 1: Chemical structure of PMS250 – Hex-5T-Hex oligomer

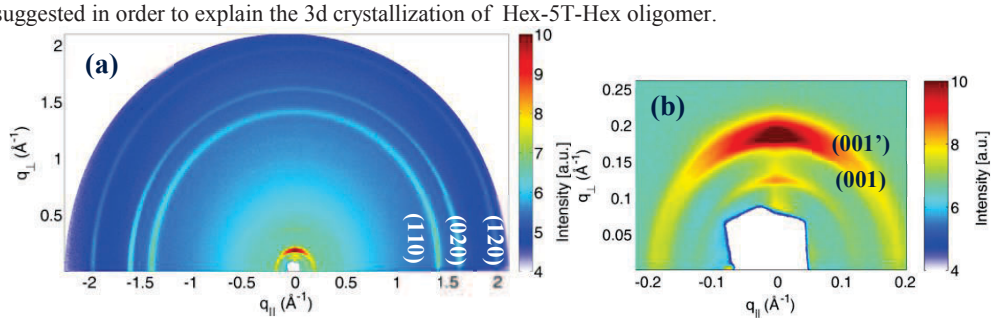

Fig. 2. (a)2d GIXD pattern obtained for Hex-5T-Hex thin film, (b) zoomed reflections for smaller q values

The aim of the second part of the study was to correlate the structural with the electrical properties of the system during film formation by casting from solution under applied electric field along in-plane direction. It was found that the evolution of both the electrical and the structural signals show the same functional characteristics. Using preliminary data of in-situ characterization no delay was observed between structural and electrical current maxima for Hex-5T-Hex oligomer (Fig.3). This is in contrast to thiophene based P3HT polymers for which the current was getting its maximum just before the film gets completely dry which was associated to so called gel-like state [3]. It is an on-going research to understand the crystallization and charge carrier transport processes. Both will help to optimize respective devices which are based on oligothiophenes.

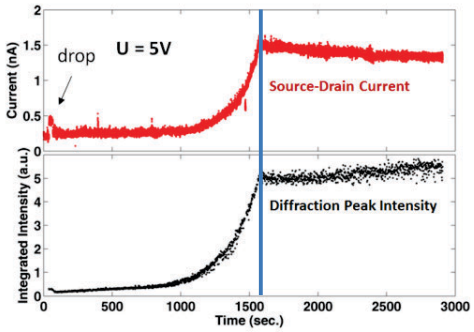

Fig. 3. Curves illustrating both current and the integrated intensity of (001') peak evolution during film formation process.

References

[1] Mathijssen S. G. J. et al., *Nature Nanotechnology* **2009**, 4, 674 – 680
[2] Agina E. V. et al., *Langmuir* **2012**, 28 (46), 16186–16195
[3] Grodd L. et al., *Macromolecular Rapid Communications* **2012**, 33(20), 1765–1769

Protein Adsorbates on Hydrophobic Surfaces

Jonas Heppe♣, Hendrik Hähl★, Christian Kreis♣, Christian Spengler♣, Mischa Klos♣, Michael Paulus♦, Metin Tolan♦ and Karin Jacobs*♣

♣ Experimentalphysik, Universität des Saarlandes, D-66041 Saarbrücken
♦ Fakultät Physik/DELTA, TU Dortmund, D-44221 Dortmund
★Institute of Physical Chemistry, University of Zurich, CH-8057 Zurich
* email: k.jacobs@physik.uni-saarland.de

Introduction

A surface that comes into contact with a protein solution will quickly be covered by adsorbed proteins. This protein adsorbate acts as a starting ground for later biofilm development. So to study this very first adsorption process is of great interest in biomedicine and technical applications.
In former studies, we could show that not only the surface influences the adsorption process, also the subsurface composition of the substrate plays an important role [1]. The subsurface composition mainly dominates the interaction potential for longer distances and therefore determines the kinetics of the adsorption process, the surface chemistry, however, is responsible for the short-range part of the potential and determines for instance whether the proteins denature. It was found that on samples that were rendered hydrophobic by a silane coating proteins strongly denature [2]. The applied surfaces differ not only in surface energy, which is the property that defines whether a surface is hydrophobic or -philic, but also in their atomic structure. It is not clear whether the strong denaturation found on the silanes is only due to their low surface energy or also enhanced by the structure.
In this study, different surfaces (hydrophobic and hydrophilic) have been brought into contact with protein solutions. As adsorbates we used hydrophobins (HFB), a special kind of amphiphilic proteins,[3]. They show very unusual linear adsorption kinetics at the air/water interface. The question is if the adsorption behaviour can be reproduced at the solid/liquid interface and by which parameters it is influenced (surface enery, steric and electrostativ interactions).
Hereby, hydrophobic silane coated surfaces and hydrophilic silicon oxide surfaces were used. Furthermore mutants of the hydrophobins are used which are altered in geometry or charge. As previous studies have shown [4, 5], XRR is well-suited for the study of adsorbed protein films at solid/liquid interfaces.

Experiments and Results

The XRR measurements were performed at the BL9 at the synchrotron radiation source DELTA in Dortmund. Beam energies of 27 keV were used. For *in situ* measurements the sample substrates were situated in a closed Teflon cell with windows especially designed for XRR. The cell was flushed with 5 ml acetate buffer at pH 5. Before the injection of the proteins a measurement of the empty cell was done to collect reference data. Then the protein solution was injected. After that two to three 45 minutes long runs were done to ensure to reach a stationary state. Only minor differences in the last two runs support this. Therefore only this data was used for evaluation. Because of the complex layer system of the hydrophobic OTS samples, also reference data in air of the uncovered wafers were taken. The XRR measurements were intended to give a comparison between the different HFB wild types and its mutants concerning their adsorption behaviour on different substrates. As wild type proteins we used HFBI and HFBII. HFBI-DK and HFB-DCBD are mutants of the associated proteins which are modified in their charge respectively in their geometry. As surfaces to cover bare silicon wafers with a native silicon oxide layer (2 nm) and OTS-coated wafers were used.
The measured reflectivities on OTS could be modeled by assuming a single layer of hydrophobins. Out of the fitted XRR data, electron density profiles (Fig. 2) were calculated. They show a clear difference between the two wild type proteins HFBI and HFBII on OTS. For HFBII the protein volume fraction in the adsorbate

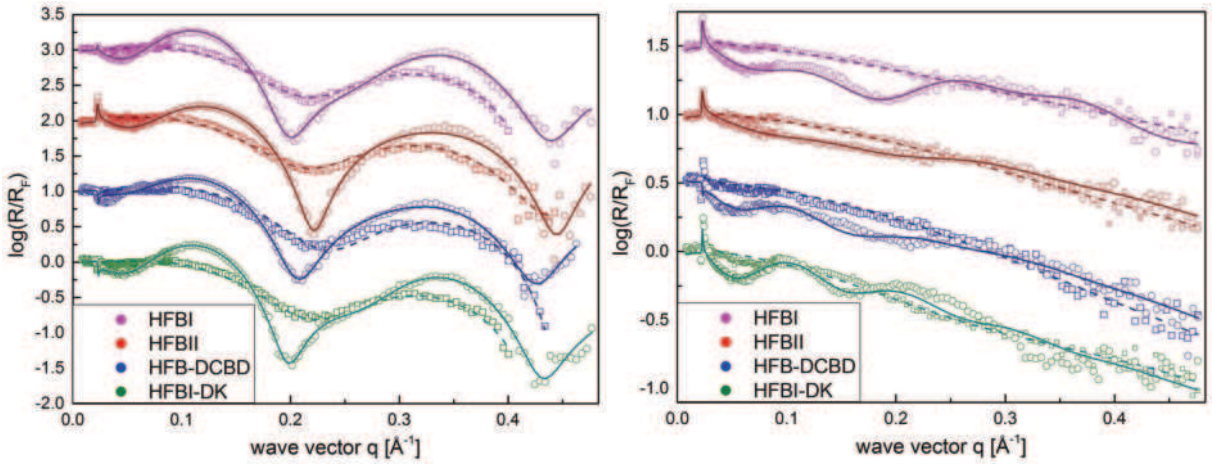

Fig. 1: Reflectivity divided by Fresnel-Reflectivity of HFBI, HFBII, HFB-DCBD and HFBI-DK on (a) hydrophobic and (b) hydrophilic surfaces. The squares show the reference data of a bare substrate. Protein covered surfaces are plotted with open circles. The best fit is given as a solid line. All curves are artificial shifted for better overview.

decreases quicker than for HFBI. Between HFBI and its mutant (HFBI-DK) no significant difference is observable. Electrostatic interaction does not play a big role, which corresponds to ellipsometry data. HFB-DCBD shows a reduced adsorbed amount in comparison to the wild types.
On silicon oxide a final modelling is still on the way since less pronounced fringes complicate the fitting procedure. The fitting of the data shown in figure 2b assumes a monolayer of proteins. With this assumption

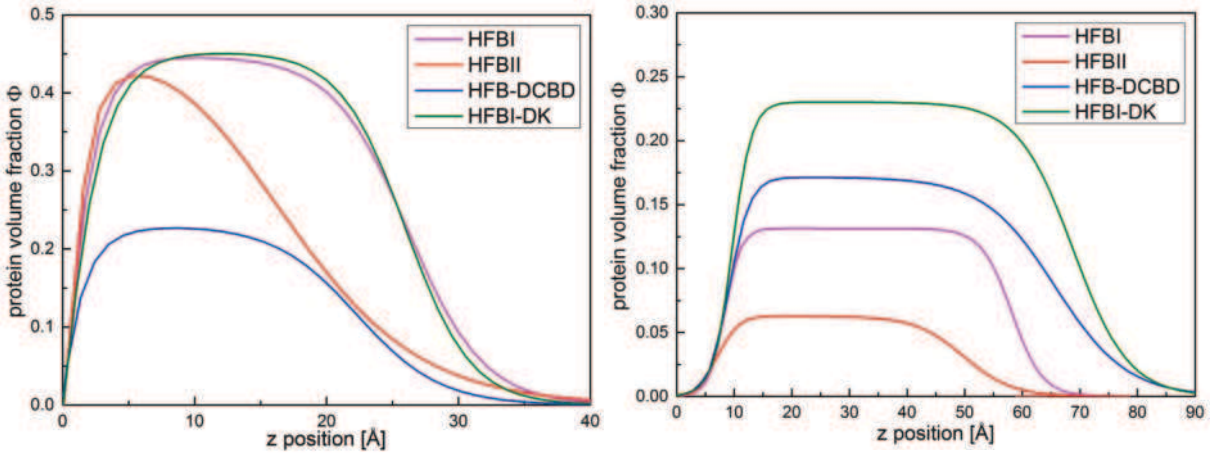

Fig. 2: Protein volume fraction of the hydrophobin adsorbates on (a) hydrophobic and (b) hydrophilic surfaces. The area beneath the curves represents the adsorbed amount of proteins.

the resulting layer is thicker than on OTS but the protein volume fraction in the adsorbates is lower. Similar results have been obtained for BSA, lysozyme and alpha-amylase [2].

Conclusion

Using high energy X-ray reflectivity, protein adsorbates of hydrophobins on hydrophobic and hydrophillic substrates were measured. Not only the substrate was altered also the nature of the proteins was modified. The obtained data appear promising. A detailed analysis, however, is still in progress.

Acknowledgments

The DELTA machine group is gratefully acknowledged for providing synchrotron radiation and technical support. We thank the VTT TECHNICAL RESEARCH CENTRE OF FINLAND for providing

hydrophobins. We would like to thank the Bundesministerium für Bildung und Forschung and the Deutsche Forschungsgemeinschaft for financial support under grant number GRK 1276.

References

[1] M Bellion, L Santen, H Mantz, H Ha¨hl, A Quinn, A Nagel, C Gilow, C Weitenberg, Y Schmitt, K.Jacobs, J. Phys.: Condens. Mat. 20, 404226 (2008).

[2]H. Hähl, F. Evers, S. Grandthyll, M. Paulus, C. Sternemann, P. Loskill, M. Lessel, A. K. Hüsecken, T. Brenner, M. Tolan and K. Jacobs, "Subsurface influence on the structure of protein adsorbates revealed by in situ X-ray reflectivity“; Langmuir 28 (2012) 7747–7756

[3] T.J. Hakala, P. Laaksonen, V. Saikko, T. Ahlroos, A. Helle, R. Mahlberg, H. Hähl, K. Jacobs, P. Kuosmanen, M.B. Linder and K. Holmberg, "Adhesion and tribological properties of hydrophobin proteins in aqueous lubrication on stainless steel surfaces“; *RSC Advances* **2** (2012) 9867

[4] F Evers, K Shokuie, M Paulus, S Tiemeyer, C Sternemann, C Czeslik, M Tolan. Eur. Phys. J.: Spec. top. (2009) 167, 185.

[5] F. Evers, K Shokuie, M Paulus, C Sternemann, C Czeslik, M Tolan, Langmuir 24, 10216 (2008).

Ad- and desorption mechanisms of model proteins and the complex protein fibronectin

Irena Kiesel, Michael Paulus, Julia Nase, Karin Rüster, Kolja Mende, Thomas Büning, Florian J. Wirkert, Christian Sternemann, Metin Tolan

Fakultät Physik/DELTA, Technische Universität Dortmund, 44227 Dortmund, Germany

Proteins adsorbed at solid-liquid interfaces are an important research topic[1–3], as they play a key role in biofilm formation or in functional applications like biosensors. Many studies discuss the influence of pH value[4], salt concentration[5], subsurface influence[6], or pressure[7] on protein adsorption. We have investigated the influence of temperature on proteins at solid-liquid interfaces in different environments, namely pure buffer and protein solution. This experimental approach allowed analysing different de- and adsorption mechanisms of the well-known model proteins lysozyme (Lys), ribonuclease A (RNase A) and bovine serum albumin (BSA). Therefor, we used the 27 keV x-ray reflectivity set-up at the beamline BL9 at DELTA, Dortmund.[8] The volume fraction profiles of these three protein layers and the detailed experimental approach were discussed in the user report of 2012[9].

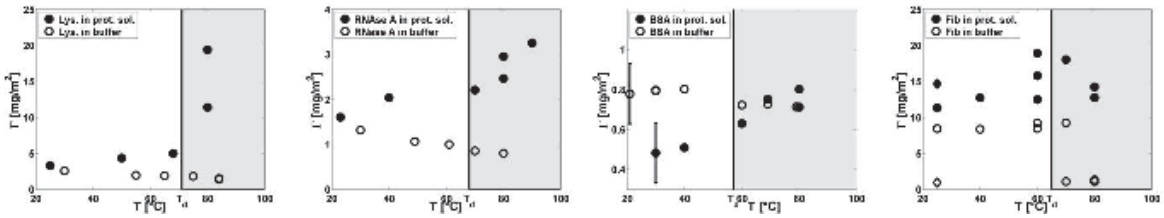

(a) (b) (c) (d)

Fig. 1: Adsorbed amount per area of a) Lys, b) RNase A, c) BSA, and d) Fib in protein solution and pure buffer during heat treatment.

The adsorbed protein amounts Γ of Lys, RNase A and BSA in the two different environments are shown in fig. 1a-c. For these three proteins in protein solution, the increase of Γ with temperature indicates an entropy driven adsorption process. Conformation changes lead to an entropy gain. The enhanced protein adsorption above the denaturation temperature T_d for Lys and RNase A could be explained by an unfolding of these “hard” proteins.[10] The desorption of the protein layers in buffer with increasing temperature are kinetically driven: the mobility of the adsorbed proteins at the interface is enhanced with increasing temperature and they can desorb more easily from the surface.

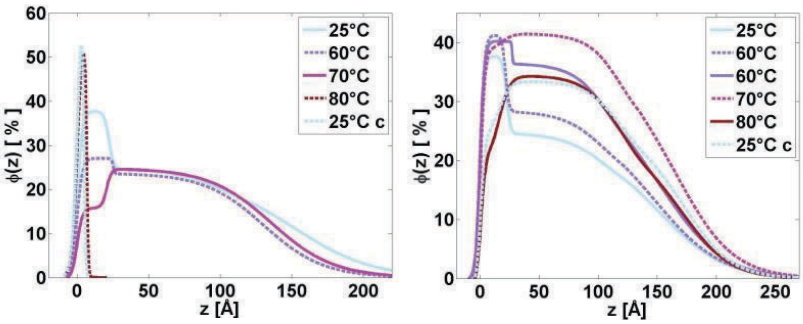

Fig. 2: Volume fraction profiles of fibronectin in a) pure buffer and b) in protein solution during heat treatment.

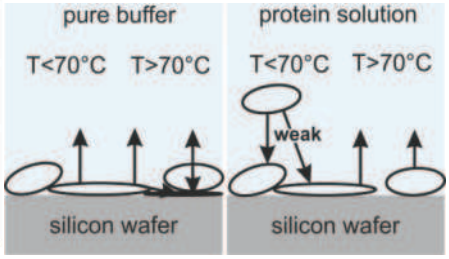

Fig. 3: Temperature and shape dependent de- and adsorption of fibronectin

A relevant protein for implant surfaces or wound dressings is fibronectin (Fib). It is involved in the formation of blood clots to stop bleeding. Fib is a complex and bigger protein than the often as models used proteins Lys, RNase A, and BSA. We repeated the same experimental procedure as for the first three proteins with fibronectin. The adsorbed amount in fig. 1d already indicates a more complex behavior of Fib in comparison with the smaller proteins. However, there are some similarities, such as an increased adsorption in protein solution in the regimes close to the denaturation temperature, and a desorption in buffer solution. The diamonds indicate the measurements at room temperature after one heat cycle. The adsorbed amount does not change during cooling.

The volume fraction profiles of fibronectin (fig. 2a+b) show two different regions, one with a thickness of 20 Å, and the other with a thickness of 150 Å. It is well known, that fibronectin has two stable conformations, one elongated shape with a diameter of 20 Å and a length of 1200 Å, and the other form, which is more globular, with a diameter between 150 Å and 350 Å.[11,12] These two different conformations are well described by the volume fraction profiles. These two conformations play a major role in the heat induced behavior. In pure buffer, the volume fraction of the 20 Å thick part decreases with increasing temperature, which means, that the proteins with a diameter of 20 Å desorb, whereas the 150 Å thick layer remains constant. At 80°C both layers collapse into a very thin layer and desorb partly. This is explainable by a complete unfolding of the protein.

In protein solution, the two different layers are observed, too. As already seen in the adsorbed amount, an adsorption occurs up to 70°C for both layers, although the layer density growth of the 20 Å thick layer is only weak. A very different behavior in comparison to the smaller model proteins is observed above 70°C: The proteins desorb in the protein solution, whereas this behavior is more pronounced for the 20 Å thick layer. Fig. 3 illustrates the temperature and shape dependent ad- and desorption of fibronectin at the solid-liquid interface.

In both environments, no change is observed in the measurements at 25°C after heating (indicated by 25°C c).

In summary, we observe temperature induced ad- and desorption for all four proteins. For the simpler model proteins, we can distinguish between thermodynamic and kinetic mechanisms. The de- and adsorption of fibronectin is influenced by the presence of two different conformations.

(1) Kasemo, B. *Surf. Sci.* **2002**, *500*, 656–677.

(2) Baszkin, A.; Norde, W. *Physical Chemistry of Biological Interfaces*; 1st ed.; CRC Press, 1999.

(3) Richter, A. G.; Kuzmenko, I. *Langmuir* **2013**, *29*, 5167–5180.

(4) Evers, F.; Shokuie, K.; Paulus, M.; Sternemann, C.; Czeslik, C.; Tolan, M. *Langmuir ACS J. Surfaces Colloids* **2008**, *24*, 10216–10221.

(5) Höök, F.; Rodahl, M.; Kasemo, B.; Brzezinski, P. *Proc. Natl. Acad. Sci.* **1998**, *95*, 12271–12276.

(6) Hähl, H.; Evers, F.; Grandthyll, S.; Paulus, M.; Sternemann, C.; Loskill, P.; Lessel, M.; Hüsecken, A. K.; Brenner, T.; Tolan, M.; Jacobs, K. *Langmuir* **2012**.

(7) Wirkert, F. J.; Paulus, M.; Nase, J.; Möller, J.; Kujawski, S.; Sternemann, C.; Tolan, M. *J. Synchrotron Radiat.* **2013**, *21*.

(8) Paulus, M.; Lietz, D.; Sternemann, C.; Shokuie, K.; Evers, F.; Tolan, M.; Czeslik, C.; Winter, R. *J. Synchrotron Radiat.* **2008**, *15*, 600–605.

(9) *http://www.delta.tu-dortmund.de/cms/de/Forschung/User_Reports/index.html*

(10) Jackler, G.; Steitz, R.; Czeslik, C. *Langmuir* **2002**, *18*, 6565–6570.

(11) Lehnert, M.; Gorbahn, M.; Rosin, C.; Klein, M.; Koeper, I.; Al-Nawas, B.; Knoll, W.; Veith, M. *Langmuir* **2011**, *27*, 7743–7751.

(12) Engel, J.; Odermatt, E.; Engel, A.; Madri, J. A.; Furthmayr, H.; Rohde, H.; Timpl, R. *J. Mol. Biol.* **1981**, *150*, 97–120.

Acknowledgement:
We would like to thank the DELTA machine group for providing synchrotron radiation and technical support.
This work was financial supported by the BMBF (project 05K10 PEC) , DFG (TO 169/17-1) and the
Cluster of Excellence RESOLV (EXC 1069).

Self-Assembled Monolayer Characterization of Silanes on Silicon Substrates

Mischa Klos♣, Matthias Lessel♣, Sabrina Haefner♣, Joshua McGraw♣, Michael Paulus♦, Metin Tolan♦ and Karin Jacobs*♣

♣ Experimentalphysik, Universität des Saarlandes, D-66041 Saarbrücken

♦ Fakultät Physik/DELTA, TU Dortmund, D-44221 Dortmund

♣ email: k.jacobs@physik.uni-saarland.de

Introduction

Silanes form smooth and homogenous self-assembled monolayers (SAM) on top of silicon substrates [1]. The silanes adhere to the substrates by forming covalent bonds with SiO_2 groups at the surface. SAMs of silanes are often used as hydrophobic substrates in various studies concerning surface roughness, surface energy, slippage [2], and protein, or bacterial adsorption [3,4]. Three different types of silanes are used to create a set of model surfaces which differ only in chain length while maintaining all other surface parameters such as roughness, surface energy, water contact angle and homogeneity. The fabrication process of these surfaces was optimized over several years in our group. The resulting surfaces were characterized using macroscopic methods such as contact angle measurements and atomic force microscopy to determine the roughness and homogeneity of the SAM [5]. We also use ellipsometry to measure the overall layer thickness. Thin polymer films of polystyrene, polyvinylpyridin and polymethylmetacrylate where prepared on top of theses substrates. For further insights to the structure and the formation of the silane layer and the overlying polymer on the silicon substrate, we performed X-ray reflectometry (XRR) measurements at the BL9 at DELTA.

Experiments and Results

To characterize the coated silicon wafers by XRR, three different types of hydrophobic silanes were prepared on top of silicon substrates with a native (2 nm) silicon oxide layer: Dodecyltrichlorosilane (DTS), Hexadecyltrichlorosilane (HTS) and Octadecyltrichlorosilane (OTS). In figure 1 it is shwon that these silanes differ only in their chain lengths. The wet chemical procedure used is the same in all three cases [5]. Measurements were performed at beamline BL9 of the synchrotron light source DELTA in a $\theta - 2\theta$-geometry. A photon energy of 12.4 keV (corresponding to a photon wavelength of $\lambda = 1.00$ Å) was used.

The specular reflectivity is measured as a function of the wave vector transfer perpendicular to the surface given as $q_z(\theta)$, where θ is the angle of incidence. The obtained data are shown in Figure 2a. The measured reflectivity is modeled as a result of the electron density profile (EDP) $\varrho_{el}(z)$ of the sample, where z is the axis perpendicular to the sample surface. The EDP is constructed using a three slab model. For the reflectivity calculation using Parratt's [6] formalism, the profile is sliced into layers thinner than 0.1 Å with an uniform electron density. The EDP giving the best fit to the reflectivity data is shown in Figure 2b. The results demonstrate the high quality of the OTS-SAM: The electron density of the tail group of 0.359(9)$Å^{-3}$ indicates a dense layer [7] of silane molecules. More than four silane chains per square nanometer are observable, which exhibits a nearly perfect order of the chains compared to MD-simulations [8]. For the overall dimensions of this layer, the EDP calculates a thickness of 20.7(1) Å, which is in excellent agreement with the bare length of the OTS tail group [9]. This result confirms the assumption of an *all trans* confirms confirms the assumption of an *all-trans* configuration of silane molecules on the SiO_2-substrate with a tilt angle of 14(7)°. DTS- and HTS-SAMs feature the same high order as OTS surfaces. However, we

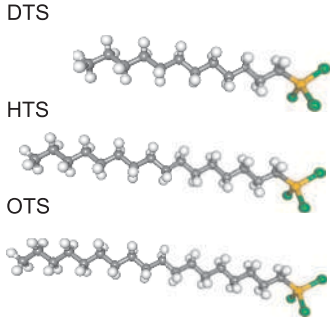

Fig. 1: Ball and stick model of alkyl-silane molecules. The represented atoms are: hydrogen (white), carbon (gray), silicon (orange), chlorine (green). Models are created with BALLView [10].

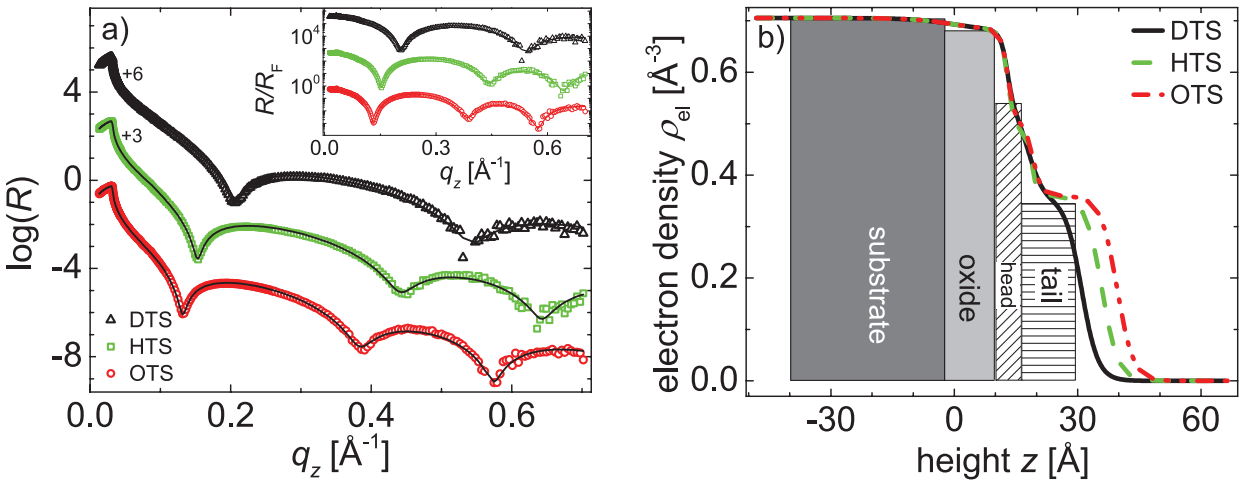

Fig. 2: a) Reflectivity R vs. scattering vector q_z (shifted for better visibility). Inset: Reflectivity normalized to the Fresnel reflectivity RF of a bare silicon wafer without roughness. The solid black line is the best fit of the model for the effective density. b) Electron density profiles corresponding to the fits shown in a). Boxes in the background schematically represent the layer thicknesses and average electron densities.

find that with decreasing silane chain length the ratio of observed SAM layer thickness to theoretical chain length decreases, which indicates an increasing tilt angle [7].

Conclusion

We have characterized the quality and revealed the structure of silane SAMs produced using a wet chemical technique. With XRR it was possible to confirm the dense packing of the layers and the *all-trans* configuration. Furthermore, we could measure the different tilt angles of the three silane coatings. This information would be difficult to obtain using techniques other than X-Ray reflectivity methods. In addition to various macroscopically obtained quantities, the XRR data completes the characterization providing structural insights to the nature of this widely used model system.
In addition to the investigations described here, we have performed a large variety of measurements with thin polymer films on these substrates. The evaluation of this more complicated layer system is not yet fully done.

Acknowledgments

The DELTA machine group is gratefully acknowledged for providing synchrotron radiation and technical support. We would like to thank the Bundesministerium für Bildung und Forschung and the Deutsche Forschungsgemeinschaft for financial support under grant number GRK 1276.

References

[1] Schreiber, F. Structure and growth of self-assembling monolayers. Prog. Surf. Sci. 2000, 65, 151–257.

[2] Bäumchen O.; Fetzer R.; Klos M.; Lessel M.; Marquant L.; Hähl H.; Jacobs K.; Slippage and nanorheology of thin liquid polymer films; J. Phys.: Condens. Matter 24 (2012) 325102

[3] Hähl H.; Evers F.; Grandthyll S.; Paulus M.; Sternemann C.; Loskill P.; Lessel M.; Hüsecken A.K.; Brenner T.; Tolan M.; Jacobs K.; Subsurface influence on the structure of protein adsorbates revealed by in situ X-ray reflectivity. Langmuir 28 (2012) 7747–7756

[4] P. Loskill, H. Hähl, N. Thewes, C. T. Kreis, M. Bischoff, M. Herrmann and K. Jacobs, Influence of the subsurface composition of a material on the adhesion of staphylococci. Langmuir 28 (2012) 7242

[5] Lessel, M.; Bäumchen O.; Klos M; Hähl H;Fetzer R.; Seemann R.; Paulus M; Jacobs K; Self-assembled silane monolayers: An efficient step-by-step recipe for high-quality, low energy surfaces, arXiv:1212.0998

[6] Parratt, L. G. Surface studies of solids by total reflection of X-rays. Phys. Rev. 1954, 95, 359–369.

[7] Tidswell, I. M.; Ocko, B. M.; Pershan, P. S.; Wasserman, S. R.; Whitesides, G. M.; Axe, J. D. X-ray specular reflection studies of silicon coated by organic monolayers (alkylsiloxanes). Phys. Rev. B 1990, 41, 1111–1128.

[8] Ewers, B. W.; Batteas, J. D. Molecular Dynamics Simulations of Alkylsilane Monolayers on Silica Nanoasperities: Impact of Surface Curvature on Monolayer Structure and Pathways for Energy Dissipation in Tribological Contacts. J. Phys. Chem. C 2012, 116, 25165–25177.

[9] Wasserman, S. R.; Tao, Y. T.; Whitesides, G. M. Structure and reactivity of alkylsiloxane monolayers formed by reaction of alkyltrichlorosilanes on silicon substrates. Langmuir 1989, 5, 1074–1087.

[10] Hildebrandt, A.; Dehof, A. K.; Rurainski, A.; Bertsch, A.; Schumann, M.; Toussaint, N.; Moll, A.; Stockel, D.; Nickel, S.; Mueller, S.; Lenhof, H. P.; Kohlbacher, O. BALL - biochemical algorithms library 1.3. BMC Bioinformatics 2010, 11, 531.

Phase Transformation during Sparc-Plasma-Consolidation and Solution Annealing of a Metal Matrix Composite

A. Mohr[1,*], A. Röttger[1], M. Windmann[1],W. Theisen[1]
[1]Lehrstuhl Werkstofftechnik, Ruhr-Universität Bochum, Universitätsstraße 150, 44801 Bochum, Germany
*e-Mail: mohr@wtech.rub.de

Wear and corrosion cause high financial damages in industrial processes. One opportunity to reduce wear of components against coarse abrasives can be found in the use Metal Matrix Composites (MMC). The advantage of MMC materials can be found in the mixing of different metal matrices and hard phases, thus a materials design can be achieved [1]. Therefore, the microstructure of MMC can be optimized with regard to the required mechanical, physical and tribological properties in consideration to the existing tribo-system. One material which is used for wear and corrosion resistance parts can be found in the MMC named FerroTitanit® Nikro128, produced by "Deutsche Edelstahlwerke GmbH". FerroTitanit® Nikro128 is characterized by a huge amount of TiC-particles (approx. 44 vol%) which are finely distributed in a corrosion resistant soft-martensitic Fe-base matrix. The chemical composition of Nikro128 is given in table 1.

Tab 1: Chemical composition of the material Nikro128 in mass%. [2]

Material	Cr	Co	Ni	Mo	Fe	TiC
Nikro128	13.5	9.0	4.0	5.0	bal.	30.0

Conventionally, FerroTitanit® Nikro128 is produced by admixing pure metal powder with TiC-particles and the following compaction of the powder mixture by sintering technique [1]. The aim of the present study is to use the Sparc-Plasma-Consolidation (SPC) as a novel and economic technique for powder compaction of Nikro128. The SPC process is shown in Figure 1. Thereby, 10 g of Nikro128 powder mixture was filled into a ceramic die and uniaxially pre-compressed with two CuCoBe punches with a load of 352 MPa. In addition, a current discharge leads to the formation of a liquid phase inside the powder mixture, as a result of joule heat formation. Compaction is promoted by the formed liquid phase, which infiltrates the pores between the powder particles in the powder bed, resulting in a dense microstructure within 5 ms [3]. In this work, the admixed powder was compacted by a mechanical pressure of 352 MPa and two time-shifted electric impulses of 12 kJ and 56 kJ.

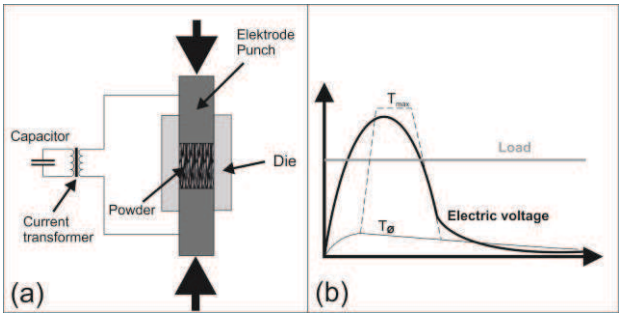

Fig 1: (a) Schematic picture of the SPC process, (b) SPC process parameter [5]

Due to the high heat and cooling rate during compaction, diffusion processes can be neglected. On this account, a further solution annealing to achieve the required materials properties is needed, promoting a homogeneous microstructure of the compacted pure powder mixture of FerroTitanit Nirko 128 by diffusion processes. Solution annealing of the SPC-compacted pure powder mixture was performed at 1200°C for 2 h and 4 h in argon atmosphere. Microstructure of the SPC-compacted and heat treated samples were analyzed by Scanning Electron Microscope (SEM). Prior to microstructural analyzes, phase composition was investigated by ex-situ diffraction measurements with synchrotron radiation (λ= 0.45919 Å) at electron storage ring Delta BL9 at the TU Dortmund. The microstructure of the SPC-compacted Nikro128 sample is shown in figure 2. Beside a low residual porosity, which is located at the particle interfaces, a fine distribution of the TiC particles can be observed (dark grey phase). In addition, different phases in the microstructure can be identified which are marked by different shades of grey. These different phases constitute the respective pure powder particles which are separated with a clear boundary from each other. Regarding the EDS results, the admixed pure element particles and the TiC-particles can be observed separately, thus no diffusion during SPC-densification between the respectively particles occurs. Therefore, the inner cohesion of the SPC-densified microstructure can be traced back to a welding of the several particles at their contact points. The results of the diffraction measurements of the SPC compacted sample are shown in Figure 3a. The microstructure in SPC-compacted state consists of TiC and pure alloying element particles. On this account this result is in a good agreement with the aforementioned

EDS-investigation because the formation of new phases due to diffusion processes cannot be observed. To achieve a homogeneous microstructure with a finely distribution of the alloying elements, solution annealing at 1200 °C for 2 h was performed. As a result, formation of the phases α- (nickel-martensite) and γ-Fe (austenite) beside TiC (Figure 3b) could be observed in the microstructure of Nikro128 in solution annealed condition. Thereby, all alloying elements are dissolved in the α-γ-metal matrix and no additionally Cr-, Mo-rich carbides or intermetallic phases were found. Thermodynamic calculations confirm a complete austenitic metal matrix at 1200 °C. This austenitic metal matrix is only stable at high temperature and transforms at lower temperature to nickel-martensite with a high dislocation density. The results of the phase analysis show that the austenitic phase is too stable to transform completely into soft-martensite during quenching.

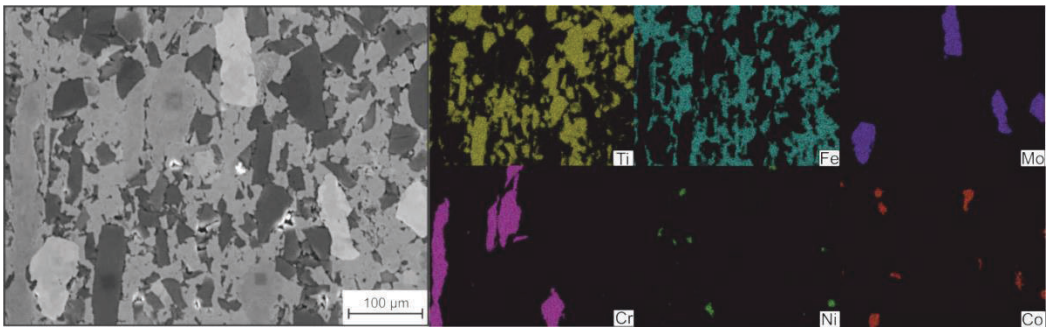

Fig 2: SEM picture of an SPC compacted Nikro128 mixture and an EDX mapping.

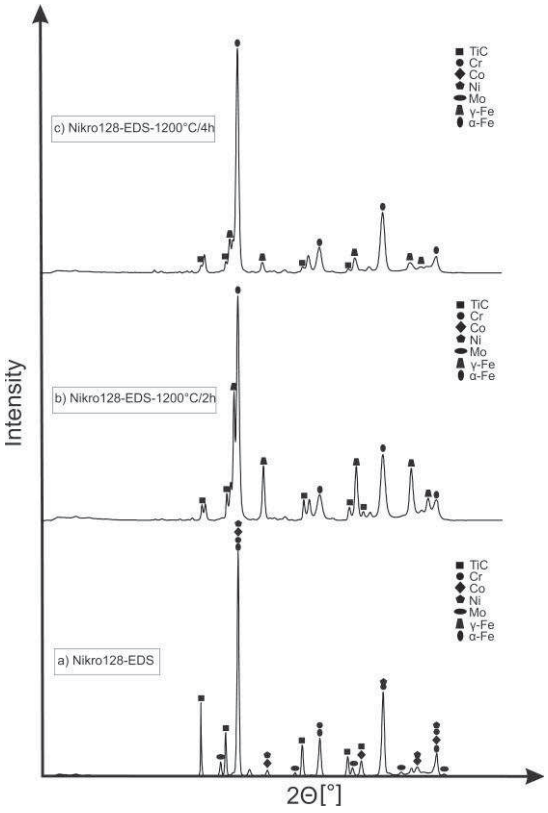

Fig 3: Diffraction patterns of the Nikro128 SPC -compacted and in solution-annealed condition.

This result can be explained by γ-Fe stabilizing alloying elements like Ni and Co. After a solution annealing at 1200°C for 2 h, these slow diffusing elements are not distributed homogeneously in the metal matrix. On this account, austenite stability differs in the microstructure, locally. Thereby, regions with higher Ni and Co-content possess a high austenite stability which counteracts a transformation of the metal matrix to soft-martensite during quenching. An increase in dwell time from 2 to 4 h reduces austenite stability by a more pronounced Ni and Co-diffusion (Figure 3c), counteracting locally high concentrations of Ni and Co in the microstructure of the SPC-densified and solution annealed Nikro128. However, retained austenite after a solution annealing of 4 h at 1200 °C can be still observed (Figure 3c). This result confirm that a completely homogenous distribution of the respectively elements could not be achieved even after 4 h at 1200 °C.

The results confirm the possibility to compact the material Nikro128 by means of SPC-technique. Thereby, distinct diffusion processes and the formation of new phases do not occur during SPC-compaction. Only the surface of the pure powder particles are partially melted due to a current discharge which results to a welding of the packed bed consisting of the admixed pure metal and hard phase powders. A solution annealing at a temperature of 1200 °C for 2 h or 4 h leads to a nickel-martensitic/austenitic matrix with TiC due compensation in the locally difference of the chemical composition as a result of strong diffusion processes of the elements. Thereby, volume fraction of the phase austenite decreases with increasing dwell time. No intermetallic phases are measured.

References:

[1] H. Hill, 2012, Neuartige Metallmatrixverbundwerkstoffe (MMC) zur Standzeiterhöhung verschleißbeanspruchter Werkzeuge in der polymerverarbeitenden Industrie, Dissertation, Ruhr-Universität Bochum

[2] Deutsche Edelstahlwerke GmbH, 2007, Datenblatt Ferro-Titanit®

[3] P. Schütte, 2012, Aufbau einer Kurzzeitsinteranlage zur Herstellung verschleißbeständiger Verbundwerkstoffe, Dissertation, Ruhr-Universität Bochum

Refining the crystallization procedure of sI structured TMO clathrate hydrates and H_2S / THF double clathrate hydrates

H. Nelson, F. J. Wirkert, C. Sternemann, M. Paulus, M. Tolan and R. Böhmer

Fakultät für Physik, Technische Universität Dortmund, 44221 Dortmund, Germany

Clathrate hydrates are compounds formed by at least two different substances with water molecules arranging in a cage-like st**r**ucture and thus enclosing the other type of molecules.[1] In nature clathrates occur as methane hydrates in permafrost areas and on the ocean floors. These materials are of special interest because, on the one hand, they may be harvested as a fossil fuel and, on the other hand, they could exert a major impact on the earth climate because methane is one of the strongest greenhouse gases known.[2]

In this study, we continue measurements undertaken during the previous year,[3] where we analyzed the ice content of several sII structured clathrate hydrates of different guest molecules. We prepared Trimethylene oxide (TMO) clathrate hydrates and hydrogen sulfide (H_2S) / tetrahydrofuran (THF) double clathrate samples and analyzed their structure with x-ray diffraction (XRD) measurements. Again the measurements were carried out utilizing the MAR345 XRD setup at beam line BL9 at Delta TU Dortmund. For the experimental details see reference 3

Trimethylene oxide (TMO) hydrates are unique because they can form two differently structured clathrate hydrates.[4] The sII structure involves a water to guest ratio of 17:1, whereas a ratio of 7.7:1 is present in the sI structure. The guest molecules have just the right diameter to be enclathrated in the large cages of the cubic structure sI as well as in those of the cubic structure sII. For TMO hydrates the smaller cages usually stay empty. The different clathrate hydrate structures are shown in Fig. 1.

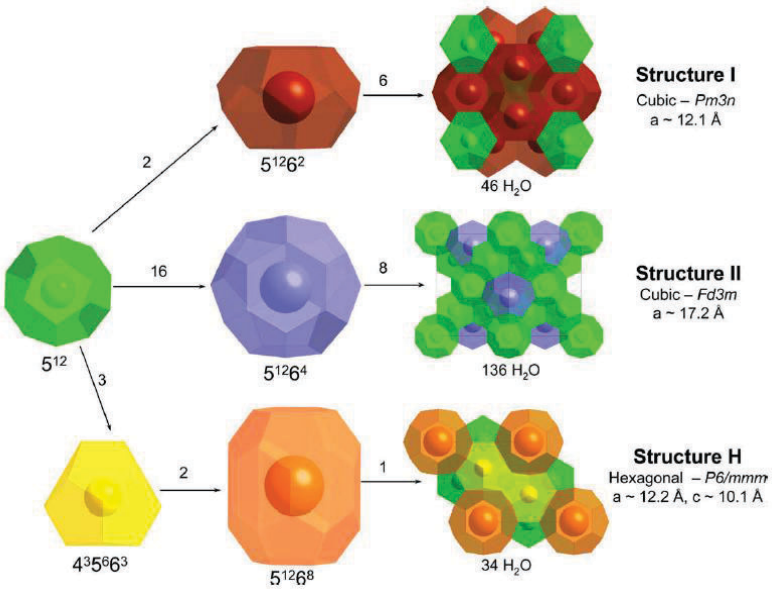

Fig. 1:
Cage structures of common clathrate hydrates. TMO only occupies the large cages of structure sI and structure sII, whereas H_2S is incorporated into the small cages of the sII structured THF hydrate. (Picture taken from Ref. 1)

The crystallization of neat sI structured TMO hydrates is challenging as always also some sII structured regions crystallize within the sample. To prevent the growth of sII structured hydrates the water-guest ratio was decreased to about 6.3:1.[5] Utilizing XRD-measurements we determined the ratio of the two competing hydrate structures in samples of composition TMO · 7.7 D_2O and TMO · 6.5 D_2O. In Fig. 2 the diffraction patterns of both samples are shown. Because the diffraction peak at 2θ = 3° stems only from the sI structure one can directly assess that the sI content in TMO · 6.5 D_2O (blue curve) is significantly larger than for TMO · 7.7 D_2O (red). For both samples we fitted a superposition of the diffraction patterns of two structures. The fraction of crystals with sI and sII structures was treated as the only adjustable parameter. We obtain a sI to sII ratio of about 40 to 60 wt% for TMO · 6.5 D_2O and 20 to 80 wt% for TMO · 7.7 D_2O. So even for increased guest concentrations the samples are mostly sII structured and we were not able to prepare neat sI structured TMO hydrates as described by reference 5.

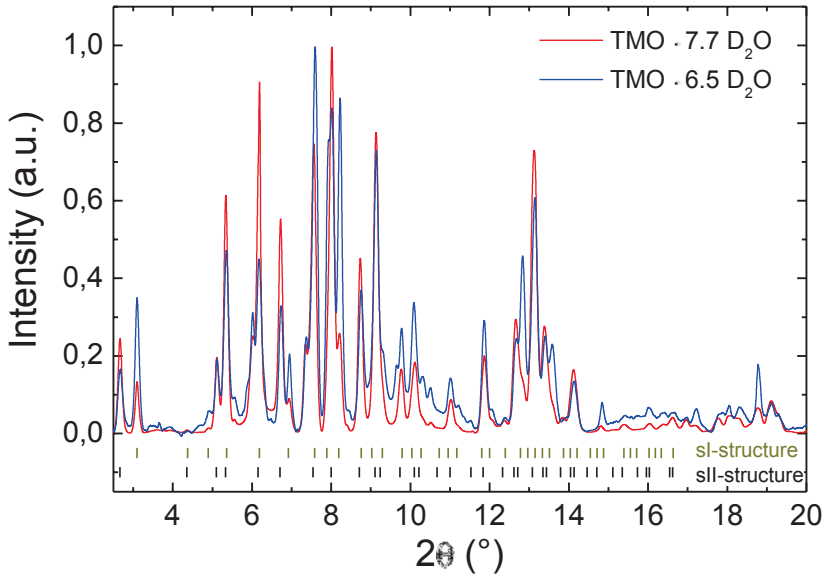

Fig. 2:
Diffraction patterns of nominally sI structured TMO hydrates with different guest to water concentrations. For TMO · 6.5 D_2O (blue) the sI content is significantly larger, see e.g. the diffraction peaks at 2θ = 3°.

Another interesting hydrate system is the double clathrate of hydrogen sulfide (H_2S) and tetrahydrofuran (THF) which crystallizes in the sII structure, see Fig. 1. The large cages are occupied by THF molecules whereas about half of the smaller cages are filled with H_2S molecules leading to a rather stable structure with a melting temperature of up to 21 °C for (THF + H_2S) · 17 H_2O.[6] Measuring the clathrate structure via XRD diffraction we were able to show that our preparation method leads to an incomplete filling of the small cages and enabled us to estimate the fraction of cages filled with H_2S. In Fig. 3 the diffraction pattern (black) of our sample and a calculated curve (red) are shown. The H_2S molecule in our analysis was approximated by an isoelectronic spherical atom, i.e., by an argon atom. We varied the filling factor of small cages in which the argon / H_2S species can reside and compared the overall squared deviations χ^2 between the fit and our data, see inset in Fig. 3. Our data is best described by a small-cage occupancy of about 10 %. Because there are twice as many small cages than large cages in structure sI hydrates, our samples can be described by the formula (0.2 H_2S + THF) · 17 H_2O.

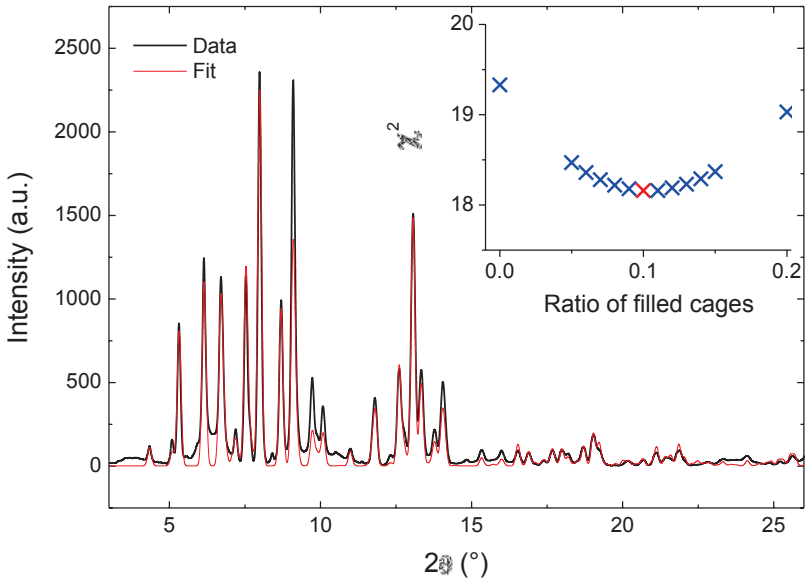

Fig. 3:
Diffraction pattern of (THF + H_2S) · 17 H_2O clathrate hydrate of structure sII. The best fit is obtained for 10 % of the small cages filled with H_2S, see inset.

The authors acknowledge the DELTA machine group for providing synchrotron radiation and technical support. HN is grateful to the DFG (BO 1301/7) for financial support. FJW likes to thank NRW Forschungsschule and BMBF (05K10 PEC) for financial support.

References

[1] T. Strobel, K. Hester, C. Koh, A. Sum and E. Sloan, *Chem. Phys. Lett.* **478**, 97 (2009).

[2] V. Krey et al., *Environ. Res. Lett*. **4**, 034007 (2009).

[3] See page 74-75 of Delta User report 2012:
http://www.delta.tu-dortmund.de/cms/de/Forschung/User_Reports/index.html.

[4] L. Carbonnel and J.-C. Rosso, *J. Solid State Chem.* **8**, 304 (1973).

[5] A. J. Rondinone, B. C. Chakoumakos, C. J. Rawn and Y. Ishii, *J. Phys. Chem. B* **107**, 6046 (2003).

[6] T. R. Keßler and M. D. Zeidler, *J. Mol. liquids* **129**, 39 (2006).

Thermoresponsive Behavior of Metal-Organic Frameworks monitored by in-situ XRD

Andreas Schneemann, Sebastian Henke, Inke Schwedler, Christian Sternemann, Michael Paulus and Roland A. Fischer

Metal-organic frameworks (MOFs) are porous materials consisting of metal clusters bridged by organic linkers. Among their outstanding properties are very high surface areas and pore volumes, making them interesting materials for gas adsorption or separation. One of the most unique features of these materials, which is not found for other porous materials like zeolites, mesoporous silicas or activated charcoals is a so called 'flexibility' characterized by a structural change upon exposure to an outer stimulus.[1, 2] Such a stimulus can for example be generated by the sorption of a guest molecule from the liquid or gaseous phase or by temperature changes[3] (Figure 1).

Figure 1: Schematic depiction of the reversible structural transformation of MOFs of the type $[M_2(BME\text{-}bdc)_2(dabco)]_n$ as a response to a heating/ccoling cycle.

In our previous studies we mainly focused on the adsorption of polar molecules in frameworks of the type $[M_2(fu\text{-}bdc)_2(dabco)]_n$ (with M^{2+} = Cu^{2+}, Co^{2+}, Ni^{2+}, Zn^{2+}; fu-bdc = functionalized benzenedicarboxylate; dabco = diazabicyclo[2.2.2]octane),[4, 5] namely $[Co_2(BME\text{-}bdc)_2dabco]_n$ (**1**), $[Ni_2(BME\text{-}bdc)_2dabco]_n$ (**2**), $[Cu_2(BME\text{-}bdc)_2dabco]_n$ (**3**), and $[Zn_2(BME\text{-}bdc)_2dabco]_n$ (**4**) (with BME2,5-bis(methoxy)ethoxybenzenedicarboxylate). These frameworks undergo a structural change from a large pored (**lp**) form to a narrow pored (**np**) form after removal of the solvent accommodated in the pore space during synthesis (Figure 2 Right; This process is referred to as activation of the pore space). This is due to interactions of the alkoxy sidechains dangling into the pores. From our previous experiments at Beamline BL9 we got a deep insight into the structural transition of the samples during loading of the contracted pore with CO_2. And indeed, a (stepwise) transition back from the **np** to the **lp** is observed. Interestingly, it was observed in TG-DSC studies (Thermogravimetric Analysis coupled with Differential Scanning Calorimetry;) that the activated material shows a phase transition from an **np** form to a **lp** form, this phenomenon is observed for all materials **1-3** (Figure 2 Left)**.**

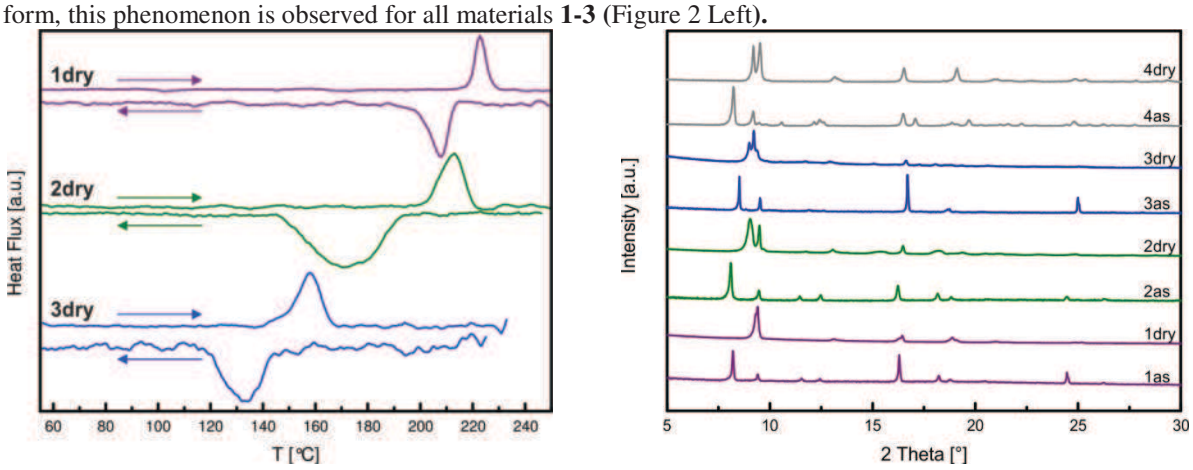

Figure 2: Left: Differential Scanning Calorimetry of the samples 1-3. The peaks symbolize the phase transitions from **np** to **lp** and vice versa; **Right:** Powder X-ray Diffraction Patterns of the functionalized frameworks in the as-synthesized and in the dry form.

From the DSCs we learn that for all three compounds differences in the phase transition temperature are observed. The cobalt containing material **1dry** has a phase transition from the **np** to the **lp** at around 220 °C, the nickel containing material **2dry** at around 210 °C and the copper containing material **3dry** at around 150°C. The closing is occurring at a slightly lower temperature than the opening. At the Delta Beamline BL09 we measured Variable Temperature XRD (VTXRD) and were able to monitor the phase transition from the change of the powder X-ray diffraction pattern during a heating/cooling cycle (Figure 3). Interestingly, for all three samples a slow pore-swelling is observed and the material is slightly expanding until a certain threshold temperature is reached. Upon reaching of this temperature the framework expands drastically and switches from the **np** to the **lp** form. We observe an increase in the switching temperature compared to the DSC measurements, however this is attributed to the difference in atmosphere. The DSCs are measured under an inert gas stream and the PXRDs under dynamic vacuum. The behavior of the materials is explained as follows: In all the materials the flexible sidechains of the linker are interacting with each other, leading to a contraction of the pore after the activation process. If the material is heated, the movement of the sidechains gets stronger and interactions of adjacent sidechains leads to the transition from the np to the lp phase of the material. The transition temperatures depend on the nature of the metal centre. Copper is present as Cu^{2+} (d^9 electron configuration), which is preferably forming square planar complexes. This means by switching back to the **lp** form (square planar) from the **np** form (distorted square planar) a energetical minima is reached and the transition temperature is much lower. Ni and Co are predominantly found in octahedral complexes and the transition temperature is more dependent on the movement on the movement of the organic sidechains than on the metal centre reaching a beneficial coordination environment, hence, the transition temperature is higher.

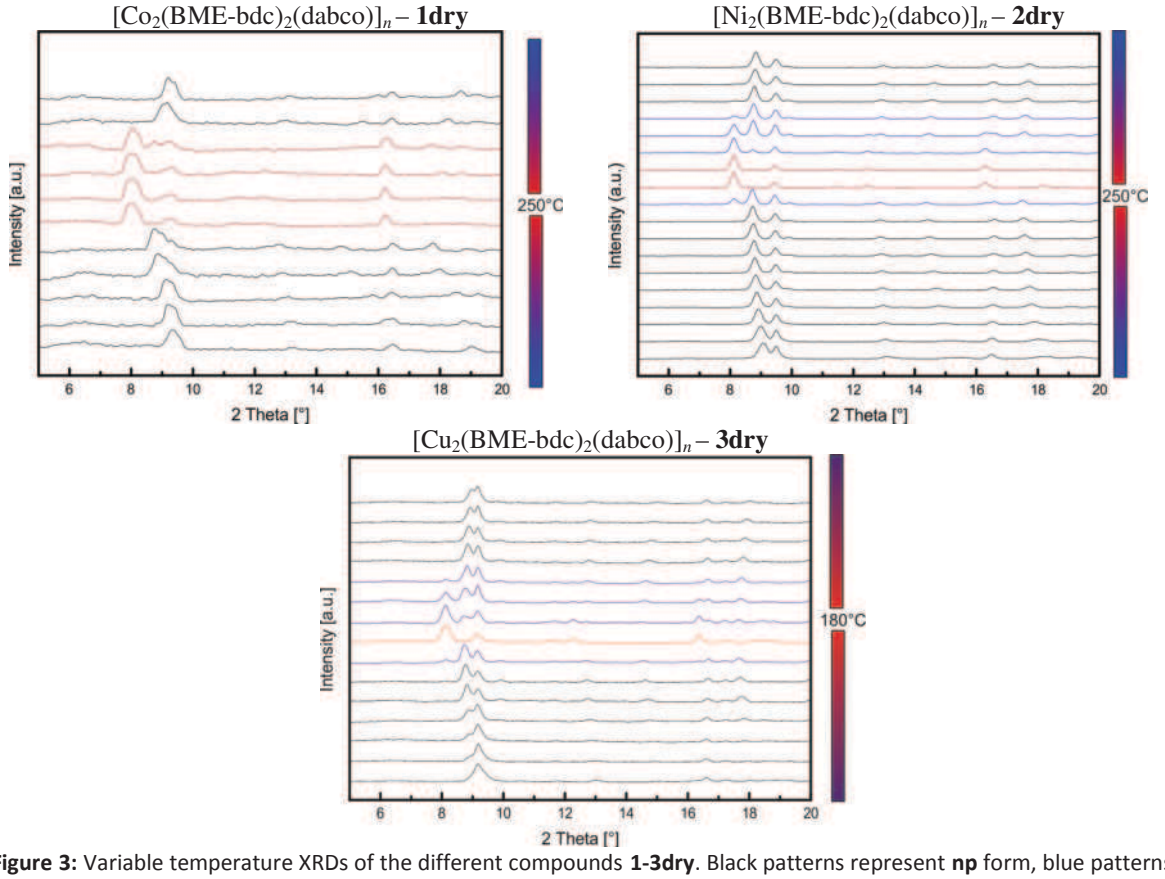

Figure 3: Variable temperature XRDs of the different compounds **1-3dry**. Black patterns represent **np** form, blue patterns a mixed phase and red patterns the **lp** form.

[1] S. Horike, S. Shimomura, S. Kitagawa, *Nat. Chem.* **2009**, *1*, 695.

[2] G. Ferey, C. Serre, *Chem. Soc. Rev.* **2009**, *38*, 1380.

[3] S. Henke, A. Schneemann, R. A. Fischer, *Adv. Funct. Mater.* **2013**, Ahead of Print.

[4] S. Henke, D. C. F. Wieland, M. Meilikhov, M. Paulus, C. Sternemann, K. Yusenko, R. A. Fischer, *CrystEngComm* **2011**, *13*, 6399.

[5] S. Henke, A. Schneemann, A. Wuetscher, R. A. Fischer, *J. Am. Chem. Soc.* **2012**, *134*, 9464.

Precipitation of $M_{23}C_6$ in nitrogen containing high-alloyed austenitic steels

S. Peperkorn*, S. Weber, W. Theisen
Lehrstuhl Werkstofftechnik, Ruhr-Universität Bochum, Universitätsstraße 150, 44801 Bochum, Germany
*E-Mail: peperkorn@wtech.rub.de

Charge-cycle-valves in combustion engines are highly stressed by different types of load. Particularly exhaust valves suffer of high thermal, chemical, mechanical and tribological loads. Since the valve head made of the austenitic steel X50CrMnNiNbN21-9 is stressed with thermal loads and mechanical stresses, the valve face is mainly subjected to tribological stresses [1]. The prevention of high wear at the valve face is conventionally reached by applying a hard facing layer of the alloy X200CrNiMoSi29-12-6 on the valve head by plasma transfer arc (PTA) welding. The nominal composition of the hard facing alloy is shown in ***Table 1***.

***Table 1*:** Nominal composition of hardfacing and substrate alloys in mass-%

Alloy	C	N	Cr	Ni	Mo	Si	Mn	Fe
X200CrNiMoSi29-12-6	2,0	---	29,0	12,0	5,5	1,25	1,0	bal.
X200-M	0,29	---	16,7	12,1	3,3	1,5	1,3	bal.
X200-M+N	0,29	0,17	16,7	12,1	3,3	1,5	1,3	bal.

Within the hardfacing alloy, a high amount of chromium carbides (> 20 vol.-%) leads to a high wear resistance, while a high amount of soluted chromium in the matrix leads to an excellent corrosion and oxidation resistance. A new process for hard facing valve heads is the super solidus liquid phase sintering. Therfore, a spheroidal powder is filled in a ring-shaped form and sintered to full density at temperatures slightly higher than the solidus of the hardfacing alloy (***Figure 1***).

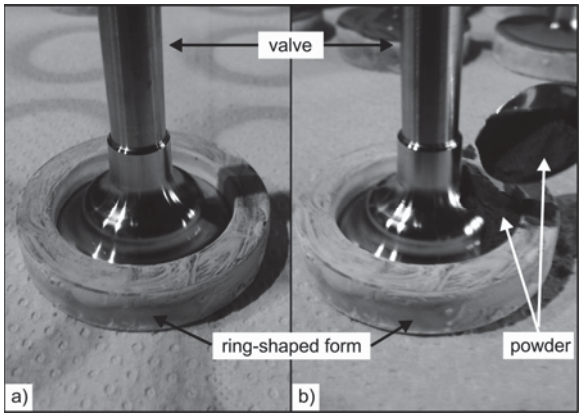

Fig. 1: a) Valve head with ring b) with powder

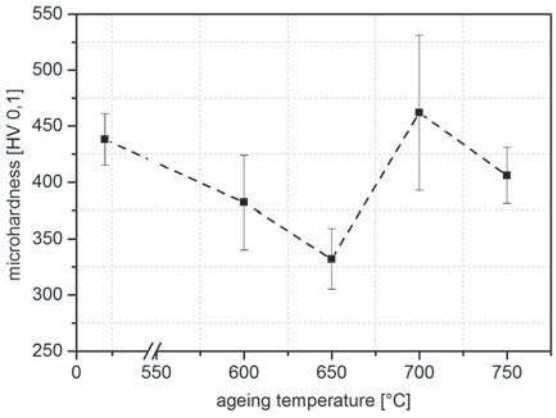

Fig. 2: Microhardness after heat treatment

Heat treatments have shown an increase in hardness by precipitation hardending (***Figure 2***). Interstitial and substitutional elements as carbon and nitrogen or chromium and molybdenum effect are generally responsible for hardening of the matrix. It is also known, that during heat treatment of the alloys in ***Table 1*** Cr-rich carbides and nitrides precipitate. This precipitation leads to a depletion of alloying elements in the matrix and a lowering the contribution of solid solution hardening, while carbides and nitrides at the same time increase the hardness due to precipitation hardening. So, there are two competing processes to observe during tempering of the hardfacing alloy, both of them being related to the final properties of the material. To investigate the occurring processes, in-situ observations of the precipitation kinetics have been carried out with synchrotron radiation (λ= 0.45919Å) at Delta BL9. The samples have been stepwise heated to temperatures between 25°C and 925°C with a dwell time of 5 minutes.

Because of the high amount of hardphases in the hard facing layer an observation of the precipitation of carbides and nitrides is exceedingly difficult. Therefore, two carbide-free model alloys X200-M and

X200-M+N corresponding to the chemical composition of the X200CrNiMoSi29-12-6 metal matrix were produced in laboratory scale (***Table 1***).

The in-situ S-XRD measurements show, that above temperatures of 600°C in the alloy X200-M a precipitation of the chromium-rich $M_{23}C_6$ carbide from the supersaturated alloy takes place (Fig. 3). With the addition of nitrogen as a second interstitial alloying element (X200-M+N), the onset of precipitation is significantly shifted by almost 200K to 795°C (***Figure 4***). Thus it can be stated, that a comparatively small concentration of nitrogen as an alloying element exerts a significant influence on the onset of precipitation. This result can be attributed to a more homogenous distribution of substitutional chromium in the matrix by nitrogen-promoted short-range ordering [2]. Additionally, at temperatures above 825°C the nitride Cr_2N precipitates and leads to a lowering of the functional properties of grain boundaries. Temperatures exceeding 800°C thus should be avoided in technical service of nitrogen-alloyed valve head coating.

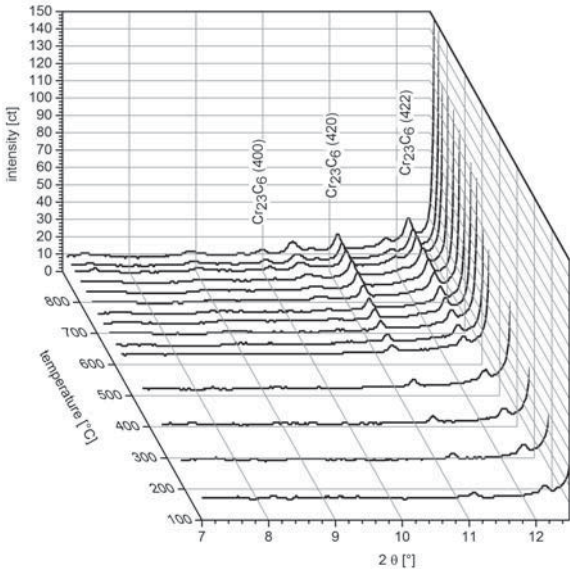

Fig. 3: Temperature dependent phase analysis of the matrix-alloy X200-M

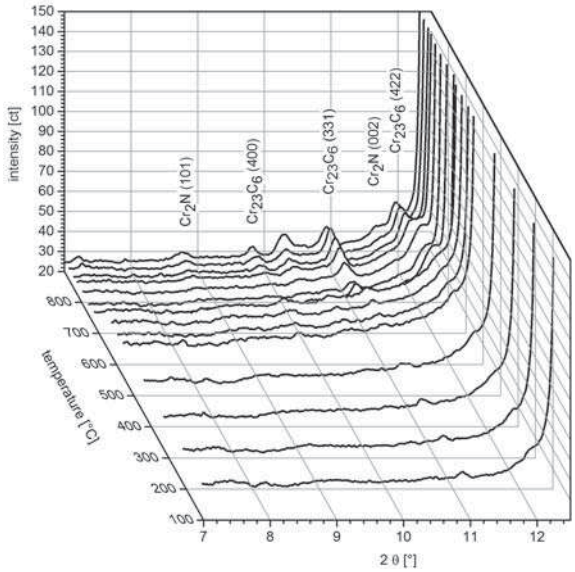

Fig. 4: Temperature dependent phase analysis of the nitrogen alloyed composition X200-M-N

With the S-XRD measurements it was possible to identify precisely the onset of precipitation and the types of precipitates. The opportunity to observe the occuring effects in-situ leads to an enormous gain in the knowledge about the precipitationkinetics and gives the possibility to apply atmospheres for avoiding outgassing of nitrogen In general, the measurements help in understanding the kinetics of carbide and nitride precipitation in supersaturated austenitic steels and are the basis for the specification of heat treatments.

References:

[1] Streich, Wolf-Dietrich: Reihe 5, Grund- und Werkstoffe, Kunststoffe. Bd. 625: Eignung neuer stickstofflegierter Stähle für Ventile in Verbrennungsmotoren: Univ., Diss. Bochum. Als Ms. gedr. Düsseldorf : VDI-Verl, 2001. ISBN 3183625059

[2] Berns, H. ; Escher, C. ; Gavriljuk, V.G. ; Shanina, B.: Zur Warmfestigkeit austenitischer Ventilstähle mit hohem Stickstoffgehalt. In: Materialwissenschaft und Werkstofftechnik 31 (2000), S. 273 - 279

[3] Mújica Roncery, Laís ; Weber, Sebastian ; Theisen, Werner: Development of Mn-Cr-(C-N) Corrosion Resistant Twinning Induced Plasticity Steels: Thermodynamic and Diffusion Calculations, Production, and characterization. In: Metallurgical and Materials Transactions A 41 (2010), Nr. 10, S. 2471-2479

Influence of silicon on the formation of intermetallic phases in an AlSi10Fe3 coating deposited on the high strength steel 22MnB5

M. Windmann*, A. Röttger, W. Theisen
Lehrstuhl Werkstofftechnik, Ruhr-Universität Bochum, Universitätsstraße 150, 44801 Bochum, Germany
*e-Mail: windmann@wtech.rub.de

In the last decade, special attention has been paid on the reduction of CO_2 emissions in the automotive industry to meet the requirements related to the global warming. Especially the development of new material concepts for automotive bodyworks, with the aim to reduce the weight of the cars, has been a central element of the research [1]. Presently, the development of automotive bodyworks goes towards multi material systems, to reduce the weight and therefore CO_2 emission on the one hand side and to meet the high safety requirements on the other hand side. Body structures, which do not require a high strength or stiffness (for example the cowl), are produced by the use of light metals (aluminium or magnesium alloys). In contrast, for safety relevant body structures (A and B-pillar), high strength steel still features light weight character due to its higher strength-to-density ratio compared to aluminium or magnesium alloys. A commonly for safety relevant body structures used steel is the boron alloyed 22MnB5, which reaches its high strength (1500-1800 MPa) in a direct press hardening process [2]. To avoid oxidation of the 22MnB5 during press hardening, an AlSi10Fe3 oxidation protection coating is deposited on the steel prior to the press hardening by hot dipping. During the austenitization in the press hardening process (6 min at 920°C), a thin Al_2O_3 layer is formed on the Al-base coating and inhibits further oxidation of the coated steel. In addition, the heat input during the autenitization leads to diffusion processes and the formation of intermetallic Al_xFe_y phases at the steel - Al-base coating interface. The formed intermetallic phases are characterized by a high hardness (1000-1100 HV) and low fracture toughness (K_{IC} = 1 MPa/m$^{1/2}$) [3,4]. On this account, the phases of type $Al_{13}Fe_4$, Al_5Fe_2 and Al_2Fe should be mentioned, which are formed in the press hardening process and lead to a cracking and out breaking of coating particles during quenching and forming in the press hardening tool. In former investigations we found, that the formation of cracks can be reduced by transforming the aforementioned brittle phases into the softer and more ductile phase of type AlFe [5]. The transformation of the brittle phases $Al_{13}Fe_4$, Al_5Fe_2 and Al_2Fe into the more iron rich phase AlFe can be achieved by different adjustments of the press hardening process. One solution is to increase the austenitization dwell time or temperature to enhance iron diffusion into the Al-base coating and support the formation of the iron rich phase AlFe. Keeping the press hardening parameters constant, a development in the chemical composition of the coating features a possibility to optimize the phase formation in the coating. G. Eggeler et al. found that silicon strongly influences the diffusion processes at steel – Al-base coating interfaces, during a heat treatment [6]. Silicon decreases the diffusion kinetic of iron and aluminium in the intermetallic phases and therefore counteracts their growth. Aim of the present study is to accelerate the diffusion of iron into and aluminium out of the coating to achieve a faster transformation of the brittle intermetallic phases into the iron rich phase AlFe, by decreasing the silicon content in the coating. In this regard, the phase formation in a conventionally by ThyssenKrupp Steel produced AlSi10Fe3 coating was compared with those in a lower silicon alloyed AlSi1.5Fe3 coating, which was produced by the Dortmunder Oberflächencentrum (DOC).

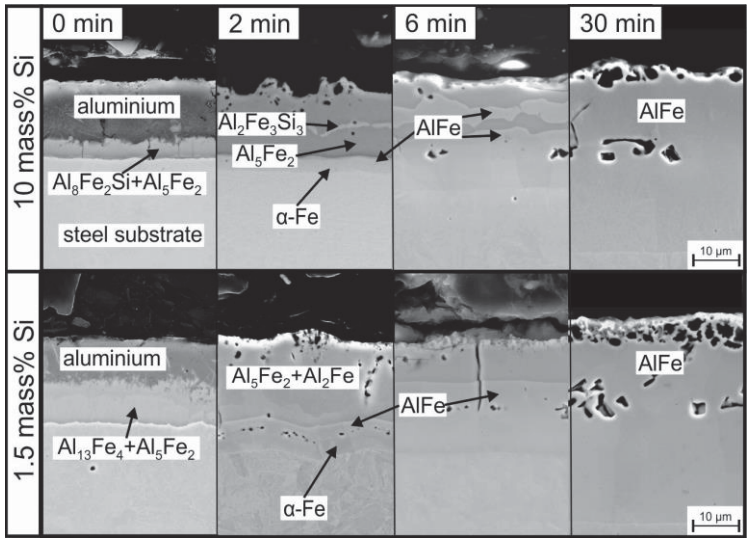

Fig. 1: SEM micrographs of the phase formation in AlSiFe coatings after different dwell times at 920°C

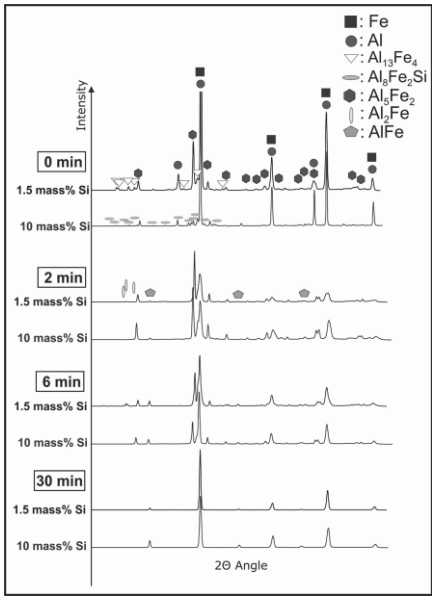

Fig. 2: Synchrotron measurements of the intermetallic phases in the coatings

Fig. 1 shows the formation of intermetallic phases in both coatings for different austenitization dwell times. The identification of the formed phases was achieved by synchrotron measurements at the DELTA in Dortmund (Fig. 2). The conventionally used AlSi10Fe3 coating (14-18 µm) is characterized by a multilayered seam of the ternary and binary intermetallic phases Al_8Fe_2Si and Al_5Fe_2 at the steel-coating interface in the initial state after hot dipping (t_{Aus} = 0 min). In contrast to these results, only binary phases of type $Al_{13}Fe_4$ and Al_5Fe_2 are formed in the low-silicon coating AlSi1.5Fe3 (13-17 µm). The absence of ternary $Al_xFe_ySi_z$ phases in the AlSi1.5Fe3 coating is attributed to the low silicon content of 1.5 mass%, which is completely solved in the binary Al_xFe_y phases. The thickness of the intermetallic phase seam was measured to 8-9 µm in the AlSi1.5Fe3 coating and 4-6 µm in the AlSi10Fe3 coating. The lower intermetallic phase seam thickness in AlSi10Fe3 can be explained by the inhibitation of diffusion processes in the intermetallic Al_xFe_y phases by silicon, which counteracts their growth. This phenomenon was discussed in several publications [5,6].

During the austenitization of the press hardening procedure, further diffusion processes occur at the steel substrate-AlSiFe coating interface. The diffusion of silicon and aluminium towards the steel substrate and iron into the coating leads to an increase of the iron content in the coating and the formation of more iron rich intermetallic phases. This process strongly depends on the alloyed silicon content in the coating, due to its aforementioned inhibiting effect on the diffusion kinetic of iron and aluminium in the intermetallic phases. Fig. 1 shows, that the AlSi10Fe3 coating is completely transformed into the binary phase Al_5Fe_2 and the ternary phase $Al_2Fe_3Si_3$ after an austenitization time of t_{Aus} = 2 min, while the AlSi1.5Fe3 coating is characterized by the formation of the binary phases Al_5Fe_2 and Al_2Fe. With increasing dwell time and iron enrichment, the phase AlFe is formed at the steel-coating interface in both coatings and grows towards the coatings. Until an austenitization dwell time of t_{Aus} = 4 min, the volume fraction of phase AlFe is higher in the low-silicon coating AlSi1.5Fe3 (Fig. 3), due to the faster diffusion of iron and aluminium in the intermetallic phases, compared to the AlSi10Fe3 coating. After t_{Aus} = 4 min, the influence of silicon on the AlFe formation seems to be reserved. The volume fraction of AlFe faster increases in the AlSi10Fe3 coating. This can be explained by the transformation of the ternary phase $Al_2Fe_3Si_3$ into AlFe after a dwell time of t_{Aus} = 4 min, which is not formed in the AlSi1.5Fe3 coating. Subsequently, the phase of type AlFe grows from the steel-coating interface as well as from the transformed $Al_2Fe_3Si_3$ phase in the middle of the AlSi10Fe3 coating, while it only grows from the steel-coating interface in the AlSi1.5Fe3 coating due to the absence of phase $Al_2Fe_3Si_3$. Consequently, after a dwell time of t_{Aus} = 4 min, the transformation of the coating into phase AlFe is accelerated in the more silicon rich AlSi10Fe3 coating.

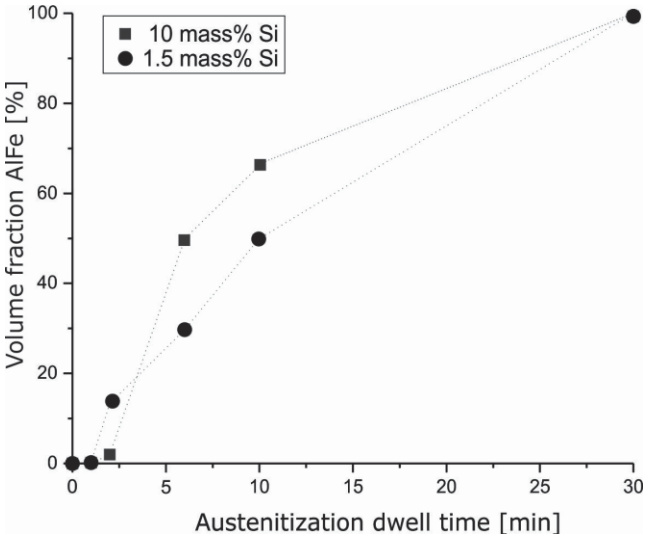

Fig. 3: Evolution of the volume fraction of phase AlFe as a function of the dwell time in the Al-base coatings

Thus, the transformation of the coating into intermetallic phases during the austenitzation process of the steel substrate can be divided into two periods. During the first two minutes of the austenitization time, silicon inhibits the transformation of the coating into intermetallic phases. After t_{Aus} = 2min, the transformation of the brittle intermetallic phases into the iron rich and more ductile phase AlFe can be accelerated by increasing the Si content to 10 mass% due to the formation of the ternary phase $Al_2Fe_3Si_3$, which transforms into AlFe after t_{Aus} = 2 min.

We gratefully thank the Delta machine group for providing synchrotron radiation beam time and acknowledge the staff of Beamline BL9 for their support and help during the experiments.

References:

[1] W.S. Miller , L. Zhuang, J. Bottema, A.J. Wittebrood, P. De Smet, A. Haszler, A. Vieregge:, Material Science and Engineering A280 (2000), pp. 37-49
[2] A. Barcellona, D. Palmeri, Metall. Mater. Trans., A, 40 (2009), pp. 1160-1174
[3] S. Kobayashi, T. Yakou, Mater. Sci. Eng., A, 338 (2002), pp. 44-53
[4] U. Köster, W. Liu, H. Liebertz, M. Michel, Journal of Non-Crystalline Solids 153/154 (1993), pp. 446-452
[5] M. Windmann, A. Röttger, W. Theisen, Surf. Coat. Technol. 226 (2013), pp. 130-139
[6] G. Eggeler, W. Auer, H. Kaesche, J. Mater. Sci., 21 (1986), pp. 3348-3350

Vulcanized Fiber and its production

Karin Rüster[1], Dominik Dumke[2], Michael Paulus[1], Christian Sternemann[1], Julia Nase[1], Johannes Möller[1], Kolja Mende[1], Irena Kiesel[1], Dorothee Wieczorek[2] and Metin Tolan[1]

[1] Fakultät Physik / DELTA, Technische Universität Dortmund, D-44221 Dortmund, Germany
[2] Fakultät Maschinenbau, Technische Universität Dortmund, D-44221 Dortmund, Germany

Vulcanized fiber is a material of various applications, for example it is used as an insulator in the electrical industry, and can be found in welding shields. As it is made from renewable resources, it gained increasing interest in recent years.

There are two ways to produce vulcanized fiber: mercerisation and parchmentising. Raw paper is soaked with alkaline (mercerisation) or acidic solution (parchmentising), pressed to interconnect the layers, rested for a certain time, and washed out in steps of descending concentrations. During this process the material's properties change. The material becomes harder, stiffer, and thicker due to multiple layering and structural changes which can be analysed by x-ray diffraction (XRD). Paper consists mostly of cellulose I_α [1] and I_β [2], which transforms to cellulose II [3] during the process of mercerisation [4]. The structural change during the process of parchmentising by zinc chloride was examined.

In order to study the material and the structural changes during the production process, the raw paper and the vulcanized fiber were analysed by XRD. In addition, different production steps were studied, where the paper was soaked in a solution of 70% zinc chloride solution, pressed, and washed out in different steps of diverse concentrations. The experiments were performed at beamline BL9 at DELTA [5] with a photon energy of 27 keV using a MAR345 image plate detector.

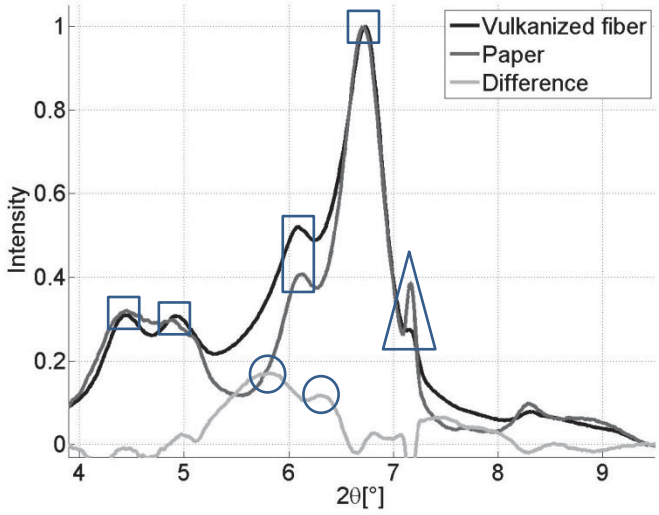

Figure 1: Diffraction pattern of Hornex vulcanized fiber (VF) produced by Ernst Krüger GmbH and Co. KG and paper the difference between these two spectra. Squares mark cellulose I, circles mark cellulose II and triangles mark iron oxide which is contained in the samples.

Figure 1 shows diffraction patterns of the final vulcanized fiber, the raw paper and its difference. The sample material of the vulcanized fiber is called Hornex and was produced by Ernst Krüger GmbH and Co. KG. The measured data of the paper has accordance to the patterns of cellulose I_α and I_β as expected (see figure 2). The pattern of the vulcanized fiber shows cellulose I too. The difference points out changes in the interval around 2θ = 5.2° and 6.7° which may be due to the formation of cellulose II. We expect a structural change from

cellulose I to cellulose II is expected during mercerization and parchmentising. The measurements show that during parchmentising, only a small part of cellulose I is transformed into cellulose II. Further data analysis is in progress.

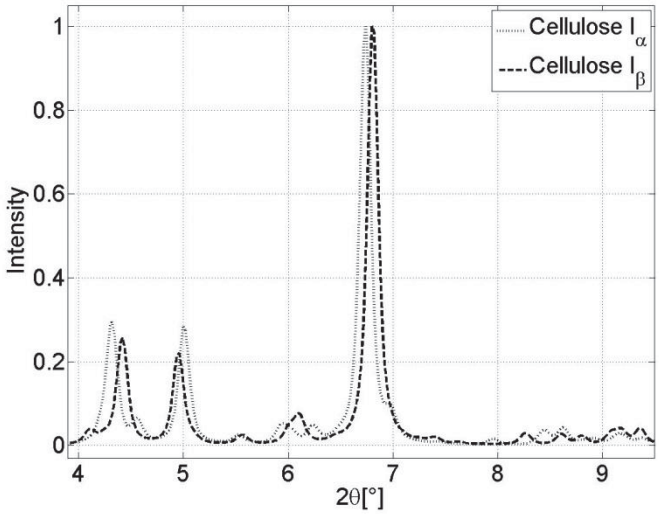

Figure 2: Simulated diffraction pattern of cellulose I_α [1] and I_β [2].

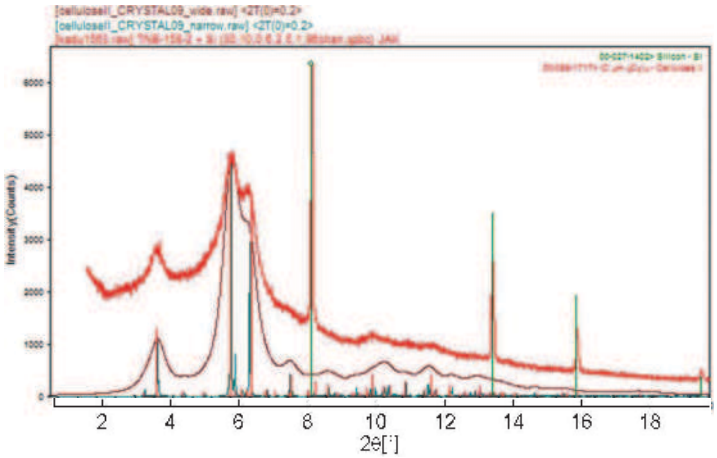

Figure 3: Observed and calculated powder patterns of cellulose II [3]. The x-axis is rescaled to fit the used Energy of 27 keV.

References

[1] Yoshiharu Nishiyama, Junji Sugiyama, Henri Chanzy, Paul Langan; "Crystal Structure and Hydrogen Bonding System in Cellulose I alpha from Synchrotron X-ray and Neutron Fiber Diffraction", J. AM. CHEM. SOC., 125, 14300-14306 (2003)

[2] Yoshiharu Nishiyama, Paul Langan, Henri Chanzy; "Crystal Structure and Hydrogen-Bonding System in Cellulose I beta from Synchrotron X-ray and Neutron Fiber Diffraction", J. AM. CHEM. SOC., 124, 9074-9082 (2002)

[3] James A. Kaduk, Thomas N. Blanton; "An improved structural model for cellulose II", Powder Diffr., 28, 3, 194-199 (2013)

[4] Yoshiharu Nishiyama, Shigenori Kuga, Takeshi Okano; "Mechanism of mercerization revealed by X-ray diffraction", J. Wood Sci., 46, 452-457 (2000)

[5] C. Krywka, C. Sternemann, M. Paulus, N. Javid, R. Winter, A. Al-Sawalmih, S. Yi, D. Raabe and M. Tolan, J. Synchrotron Rad. 14, 244 (2007).

Analysis of Particle-Particle Interaction Potentials of Nanoscaled Systems in Aqueous Solutions

J. Schulze[a], J. Möller[a], J.Nase [a], M. Paulus[a], M. Tolan[a], R. Winter [b]

[a] *Fakultät Physik/DELTA, TU Dortmund, Otto-Hahn-Str. 4, D-44227 Dortmund, Germany*

[b] *Physikalische Chemie I, Fakultät für Chemie und chemische Biologie, TU Dortmund, Otto-Hahn-Str. 6, D-44227 Dortmund, Germany*

The influence of pressure on the protein-protein interaction potential in dense protein solutions was studied intensely in recent years. Previous studies revealed a non-linear pressure dependence of the attractive part of the pair interaction potential $V(r)$ of proteins [1]. Furthermore, the addition of the biologically relevant osmolyte trimethylamine-N-oxide (TMAO) has been shown to cause a shift of the minimum of the attractive part of $V(r)$ [2]. To understand in detail the effects of pressure and cosolvents on the particle-particle interaction potential, we focus on well-defined model systems, i.e., highly concentrated silica nanoparticle solutions (e.g., Ludox AM). Negatively charged silica nanoparticles have an easily tunable, well-defined surface. For example, decreasing the pH of the solvent leads to a lower electrostatic repulsion between the particles.

Small-angle X-ray scattering (SAXS) is an ideal and well known technique for the investigation of non-crystalline solutions. The pressure dependent SAXS experiments were performed at beamline BL 9 of

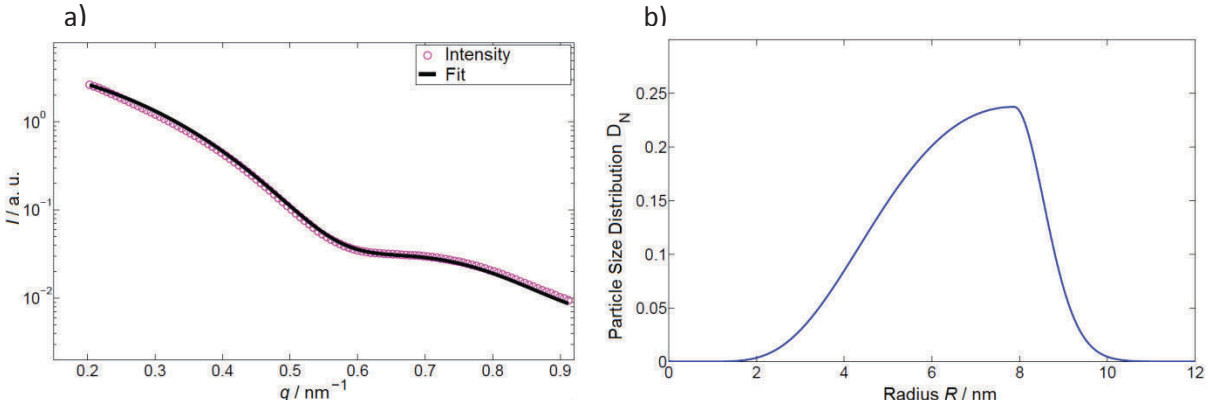

Figure 1a) Intensity *I* of a diluted nanoparticle solution of Ludox AM (corresponds to the form factor *P*(*q*)). b) Related size distribution.

DELTA with a photon energy of 10 keV.

While the form factor P(q) (see Fig. 1) contains information about the particle form and its size distribution, the structure factor S(q) (see Fig. 2) depends on the interaction between the particles. For silica nanoparticles, the obtained S(q) implies a strong repulsive potential, caused by the negative charge on the surface of the particles. The strong effect of the electrostatic interaction on the structure factor can be demonstrated by a variation of the solution pH. This is shown Figure 2a: An increase of pH (causing a stronger electrostatic repulsion) yields an increase of the amplitude of the first maximum and a shift of its position in q to lower values.

Figure 2b depicts the pressure dependent shift of the first maximum in q, utilizing a 15 wt% nanoparticle solution and the pressure stable buffer BisTris. The data indicate a slight shift of the first maximum to lower values. Thus, despite the pressure-induced compression of the solvent, the most likely

intermolecular distance between the particles seems to increase slightly with pressure (Fig. 2b). This might be due to an increased electrostatic repulsion between the nanoparticles upon compression.

In a second step, TMAO was added to the system at a concentration of 1 M. The resulting pressure dependent shift of the first maximum of S(q) is shown in Fig. 2 (green points). However, a significant change compared to the system in pure buffer solution cannot be determined. Further osmolyte concentrations will be explored in the future.

a) b)

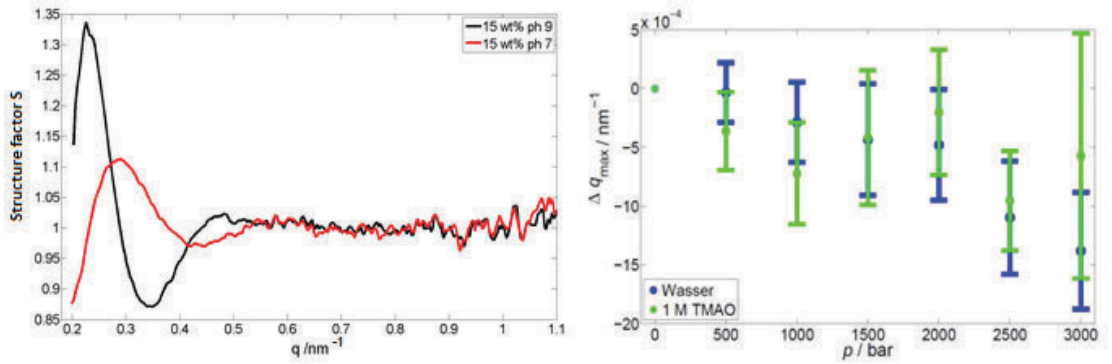

Figure 2: a) Structure factor of silica nanoparticle solutions at pH 9 (black) and 7 (red), b) pressure dependent shift of the position of the structure factor maximum q_{max} .

We would like to thank the DELTA machine group for providing synchrotron radiation and technical support. J.Schulze (project 05K13PE) and J. Möller (project 05K10PEC) acknowledge the BMBF. The authors acknowledge DFG-FOR1979 and RESOLV (EXC 1069) for financial support.

References:

[1] Schroer, M.A.; Zhai, Y.; Wieland, F.; Sahle, C.J.; Nase, J.; Paulus, M.; Tolan, M.; Winter, R.: Angew. Chem. 50(48), 2011, 11413-11416.

[2] Schroer, M.A.; Markgraf, J.; Wieland, D.C.F.; Sahle, Ch.J.; Möller, J; Paulus, M.; Tolan, M.; Winter, R.: Phys. Rev. Lett. 106(17), 2011, 178102.

Beamtime Report, DELTA, Beamline 9

T. Zander [1], D.C.F Wieland [1], M. Wang [2], A. Raj [2], A. Dedinaite [2], R. Willumeit [1]

[1] *Helmholz-Zentrum Geesthacht, Institute of Materials Research, D-21502 Geesthacht*
[2] *KTH Royal Technical Institute, Department of Chemistry, SE-100 44 Stockholm*

We studied structural assemblies of hyaluronan (HA) supported 1,2-dipalmitoyl-sn-glycero-3- phosphocholine (DPPC) bilayers at the solid-liquid interface by means of X-ray reflectivity measurements at different pressures and temperatures conditions to shed light on the mechanisms providing superior lubrication in articular joints.
The lubrication system in articular joints is a complex entity were different constitutes of synovial fluid interact with each other providing friction coefficients which are the lowest in nature even under high loads and shear rates [1]. It is thought that not individual components, but rather association structures, due to synergistic effects, are responsible for the low friction coefficients. Former studies indicate that the self organization of phospholipids and macromolecules (e.g. HA) on the cartilage is a key factor [2, 3]. The obtained experimental data will help to understand how this layers change on a increase of pressure and, thus, help to better understand the mechanisms providing the exceptional good friction properties in joints.

The measurements were performed at the Beamline Bl9 at the synchrotron source DELTA ,Dortmund, making use of the new high pressure sample cell [4]. An x-ray energy of 27keV was used. The samples were investigated in a pressure range from 1bar up to 1kbar at two different temperature, $39°C$ and $55°C$, respectively.
For the experiment we probed DPPC and a DPPC/HA composition on Si-Wafers in a 150mM NaCl-Solution. DPPC was purchased from Avanti Polar Lipids and HA with a molecular weight of $1500kDa$ was purchased from Creative PEGWorks. For the DPPC/HA composition we first let DPPC adsorb to the Si surface. In a second step we let HA adsorb on top of this structure.

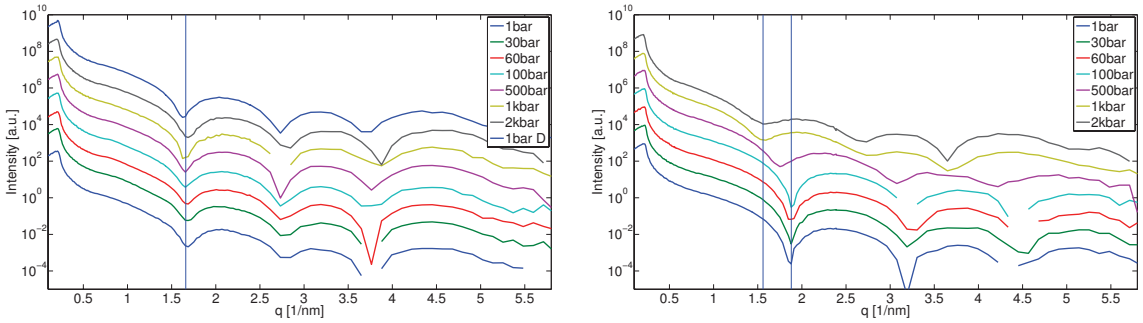

Figure 1: *XRR curves of DPPC without HA at different pressures at* $39°C$ ***(left)*** *and* $55°C$ ***(right)***. *The vertical blue lines indicate the position of the first minimum.*

Figure 1 shows X-ray reflectivity curves of the pure DPPC system. At $39°C$ (fig. 1 left) the curves do not change significantly during the pressure cycle. The first minimum always stays at the same position, i.e. the thickness of the structure does not change. This does not hold for the curves recorded at $55°C$ (fig. 1 right). Here a clear shift of the first minimum to smaller q-values can be observed as pressures exceeds 500bar. This indicates an increase of the thickness of the layer structure. Comparing the position of the first minimum for the two temperatures it can be observed that at $39°C$ and at $55°C$ ($p < 500bar$) a different layer thickness is present. In contrast the measurements at $55°C$ at pressures above 500bar show a similar layer thickness as the measurements at at $39°C$.

An example for a fit of a curve measured on pure DPPC system ($T = 39°C$, $p = 30bar$) is shown in figure 2 left. In figure 2 right the corresponding density profile is shown. It can be seen that the measured intensity curve can be described by a bilayer model.

Figure 3 shows X-ray reflectivity curves of DPPC with adsorbed HA ($M_W = 1500kDa$) at different

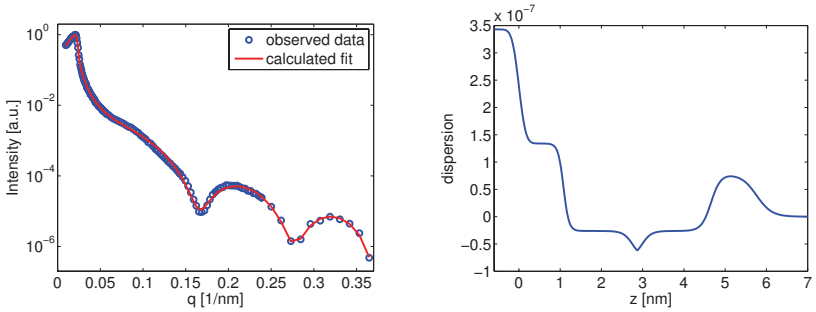

Figure 2: ***Left:*** *Fit of the XRR-curve of pure DPPC at* $39°C$ *and 30 bar with a bilayer model.* ***Right:*** *Corresponding calculated density profile.*

pressures and temperatures. At $39°C$ (fig. 3 left) the curves do not change significantly with changing pressures. This is very similar to the measurements on pure DPPC. However, the curves recorded at $55°C$ show a shift of the first minimum at pressures above $500bar$.

Compared to the curves of pure DPPC (fig. 1) the oscillation of DPPC with HA (fig. 3) are not as

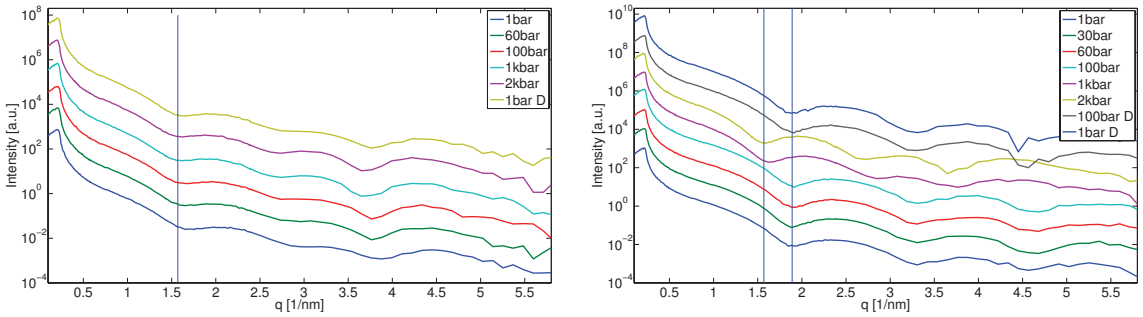

Figure 3: *XRR curves of DPPC with HA1500 at different pressures at* $39°C$ ***(left)*** *and* $55°C$ ***(right)****. The vertical blue lines indicate the position of the first minimum.*

pronounced as without HA.

The observation made for the pure DPPC system can be explained by a phase shift of the phospholipid bilayer. At $39°C$ the lipids are in the rippled phase $P_{\beta'}$ [5]. This changes as the temperatures is raised to $55°C$, at this temperature the lipids are in the liquid crystalline phase L_α. In the L_α phase the lipids have a higher mobility and the alkyl-groups are disorderd. This leads to a shrinking of the overall layer thickness as the tail groups are able to increase their tilt angle with respect to the interface. As the pressure exceeds 500bar at $55°C$ the phospholipds undergo a phase change from L_α back to $P_{\beta'}$ [6].

[**1**] Klein (2006) *Proc. Inst. Mech. Eng. J J. Eng. Tribol.* **220**, 691-710 [**2**] Hills (1989) *J. Rheumatol.* **16**, 82-91 [**3**] Liu et al. (2012) *Soft Matter*, **8**, 10241 [**4**] Wirkert et al. (2013) *J. Phys. Conf. Ser.* **425**, 202006 [**5**] Koynova (1998) *Biochim. Biophys. Acta - Rev. Biomembranes* **1376**, 91-145 [**6**] Seddon et al. (2006) *Phil. Trans. R. Soc. A* **364**, 2635-2655

Hard X-ray spectroscopy

Surface sensitive EXAFS experiments of heat-treated steels

D. Lützenkirchen-Hecht[a], D. Wulff[b], R. Wagner[a], U. Holländer[b]

a) Fachbereich C - Physik, Bergische Universität Wuppertal, Gaußstr. 20, 42097 Wuppertal, Germany.
b) Institut für Werkstoffkunde, Institut für Werkstoffkunde (Materials Science), Leibniz Universität Hannover, An der Universität 2, 30823 Garbsen, Germany.

The reduction of iron oxides is important not only for the production of metallic iron, but also for the preparation of iron containing catalysts for ammonia synthesis [1-3] and fluxless brazing processes. In the latter case the oxide layers on iron and stainless steels (Fe-Cr-Ni alloys) need to be removed while heating up such parent metals together with deposited braze metal in a furnace applying temperatures between 900 and 1150°C typically [4, 5]. Usually, metals and alloys are covered by oxide layers at elevated temperatures, and therefore the gas atmosphere during the heat treatment has to be carefully controlled in order to avoid a substantial oxidation, and reducing gases are often used to avoid oxidation. Furthermore, also the influence of the time is important. In the interesting temperature range, the literature suggests that the reduction of Fe_2O_3 to Fe metal proceeds via Fe_3O_4 intermediates in a two step reaction according to $3Fe_2O_3 + H_2 \rightarrow 2Fe_3O_4 + H_2O$ (step 1), and $Fe_3O_4 + 4H_2 \rightarrow 3Fe + 4H_2O$ (step 2). While the first step appears to be exothermic, the reduction to Fe metal in step 2 is endothermic [6]. Depending on the exact conditions employed during the reduction (e.g. gas compositions and pressures, temperatures, etc.), different kinetics have been observed, and also the form of the iron oxide sample (powder, pellet, particle and crystallite size, etc.) influences the reaction [1]. Furthermore, the formation of a stable FeO-phase must also be considered for T>600 °C [7], and alloyed metal impurities (in the case of steel samples) as well as dopants (in the case of the catalysts) also affect oxidation and reduction processes (see e.g. [3, 6]).
While thermoanalytical techniques such as temperature programmed reduction are convenient to study those reactions if bulk materials are considered, the investigation of the surface oxide layers and their decomposition reactions are much more difficult. In this case, surface sensitive methods compatible to the reaction conditions are required. With the final goal to perform in-situ studies during the temperature treatments, we have performed first ex-situ surface sensitive EXAFS measurements of heat-treated steel samples. The experiments were performed at beamline BL10 at the DELTA storage ring, employing a Si(111) channel-cut monochromator, and N_2- and Ar-filled ionization chambers as detectors for the incident and the reflected intensities.

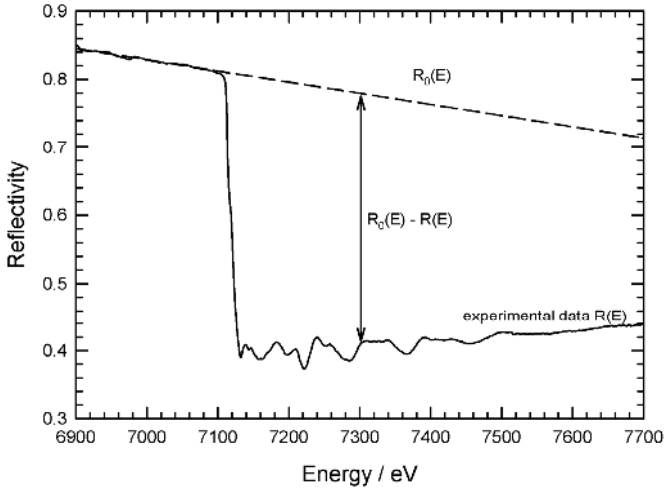

Fig. 1:
Reflection mode EXAFS spectrum of a steel sample at the Fe K-edge for an incidence angle Θ=0.1°. The sample was first heated at 600°C for 25 min. and subsequently treated at 900°C in a N_2 / SiH_4-mixture for 25 min. For the data evaluation, the pre-edge background $R_0(E)$ was extrapolated into the post-edge region of the spectrum and subtracted from the data. The difference $R_0(E)$-R(E) was used as a measure for the absorption.

As can be seen in Fig. 1, high quality reflection mode data may be obtained at Bl10. For the further data analysis, the difference $R_0(E)$-$R(E)$ was used as a measure for the absorption, and the extracted data are compared to those of reference compounds in Fig. 2.

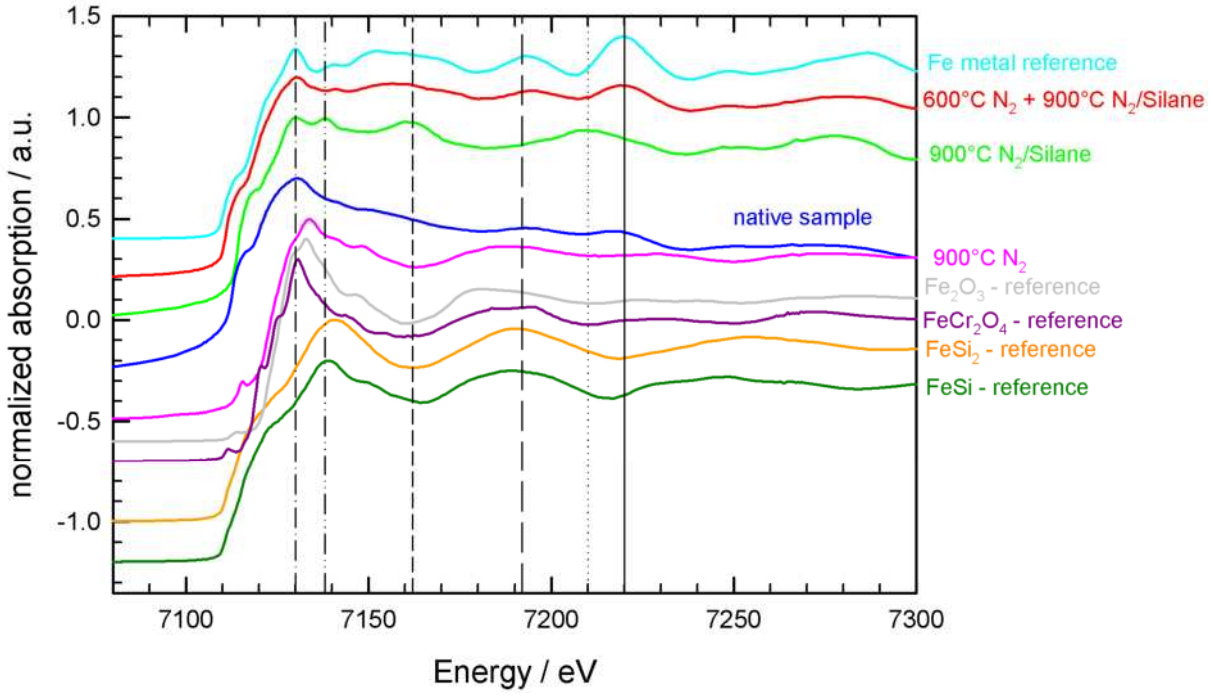

Fig. 2:
Comparison of the Fe K-edge X-ray absorption data of several heat-treated steel samples with those of a native (i.e. air-exposed) sample and several Fe reference compounds as indicated. The vertical lines represent characteristic features for metallic Fe, Fe-Si and Fe-O reference compounds.

This comparison shows that the oxide layers can be successfully removed by a heat-treatment in a N_2/SiH_4 atmosphere at 900°C, i.e. the obtained spectrum resembles well that of metallic iron. In contrast, substantial differences are detected if the pre-treatment in a pure N_2-atmosphere at 600°C is omitted, in this case features characteristic for Fe-Si compounds are detected. In addition, if only a treatment in pure N_2 is performed at 900°C, intense contributions of oxidic Fe-species may be observed. A more detailed analysis of the present data is currently under way [8].

References

[1] O.J. Wimmers, P. Arnoldy, J.A. Moulijn. J. Phys. Chem. 90 (1986) 1331.
[2] H. Jung, W.J. Thompson, J. Catal. 128 (1991) 218.
[3] G.A. Somorjai. Surface Chemistry and Catalysis; Wiley-Interscience: New York (1994) Chapter 7.
[4] F.-W. Bach, K. Möhwald, U. Holländer, C. Roxlau. SCIB - Self-Cleaning Inert-Gas Brazing - Ein neues Verfahren zum flussmittelfreien Hartlöten korrosionsbeständiger Konstruktionswerkstoffe. 8. Int. Kolloq. Hart- und Hochtemperaturlöten und Diffusionsschweißen, Düsseldorf: DVS-Verlag, DVS-Ber. 243 (2007) 235.
[5] F.-W. Bach, K. Möhwald, U. Holländer. Key Eng. Mat. 438 (2010) 73.
[6] M.V.C. Sastri, R.P. Viswanath, B. Viswanath. Int. J. Hydrogen Energy 7 (1982) 951.
[7] J.M. Quets, M.E. Wadsworth, J.R. Lewis, Trans. Metal. Soc. AIME 218 (1960) 545.
[8] D. Lützenkirchen-Hecht, D. Wulff, R. Wagner, U. Holländer. J. Mat. Sci. (2013), in preparation.

Temperature dependent EXAFS investigations of Zinc at DELTA BL10

D. Lützenkirchen-Hecht, T. Nikolova, R. Wagner, R. Frahm

Fachbereich C-Physik, Bergische Universität Wuppertal, Gaußstr. 20, 42097 Wuppertal, Germany

The extended X-ray absorption fine structure technique (EXAFS) has furthered our basic understanding of crystalline and amorphous substances, glasses and liquids owing to its ability to specify the accurate local short range structure around the X-ray absorbing atom (see, e.g. [1]). The ability of EXAFS to elucidate precisely the structural environment of a selected anion or cation is especially useful if the atom has a specific bond geometry such as in many humic or other organic solutions, and it can be applied in situ in high-temperature and high-pressure environments that are important in geochemical and environmental processes such as metal transport and ore formation [2-4].

In present study, we have investigated the temperature dependent EXAFS of metallic zinc. High-quality EXAFS data of a zinc metal foil were measured from liquid nitrogen temperature (77 K) close to the melting point of Zn (660 K). The main idea of those experiments are observations of anharmonic lattice vibrations making use of the inherent short range order sensitivity of the EXAFS method [5, 6]. For this purpose, a liquid nitrogen bath cryostat as well as a high temperature cell (Anton Paar domed hot stage DHS 1100 with controller TCU 200) have been installed at DELTA BL10. Transmission mode EXAFS spectra were collected using N_2- and Ar-filled ionization chambers for the incident and the transmitted intensities. In Fig. 1 photos of the set-ups used at BL10 for low and high temperature measurements are shown, respectively.

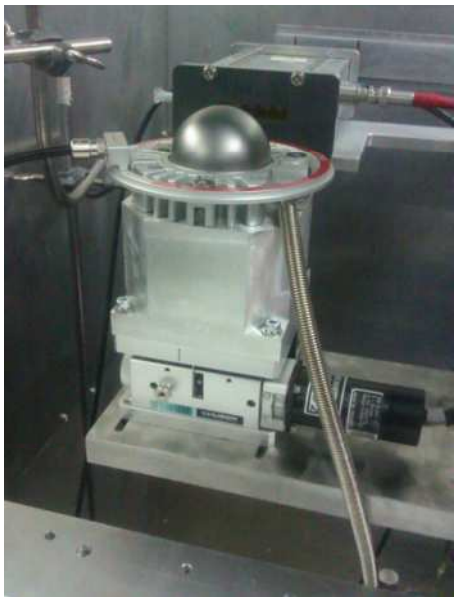

Fig. 1:
(a) Setup for low temperature EXAFS measurements at BL10 with the liquid nitrogen crystat installed at the downstream end of the EXAFS table. (b) High temperature chamber (domed hot stage) mounted on the diffractometer with a z-table for positioning the sample within the X-ray beam.

In Fig. 2, the raw data measured at 77 K as well as some selected k^3-weighted EXAFS functions $\chi(k)*k^3$ are presented for different temperatures. As can be seen, the amplitude of the EXAFS functions decreases dramatically with increasing temperature. A detailed evaluation of the data is currently in progress, preliminary fit results show a substantial increase of anharmonic contributions for temperatures above ca. 250 K [7].

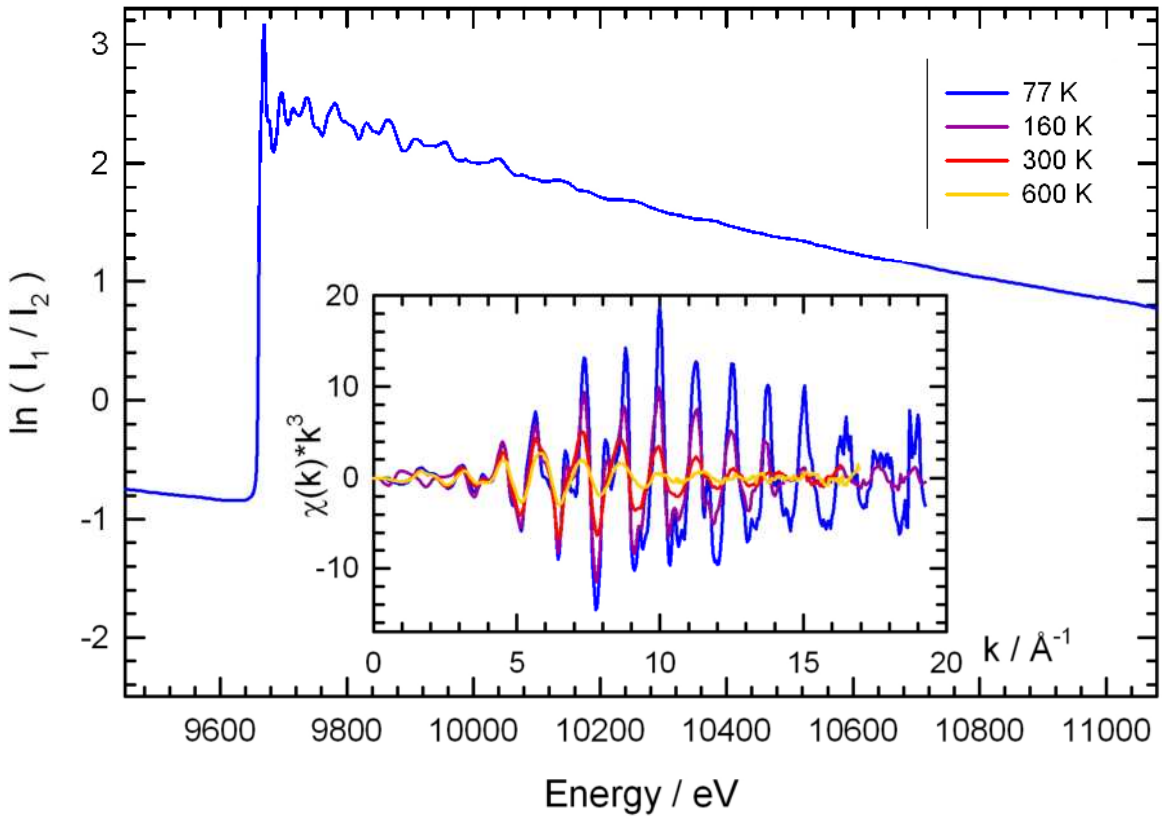

Fig. 2:
X-ray absorption spectrum of a Zn metal foil at the K-edge measured at 77 K within ca. 40 minutes. In the insert, the extracted and k^3-weighted X-ray absorption fine structure $\chi(k)*k^3$ is presented for some selected temperatures as indicated.

References

[1] D.C. Koningsberger, R. Prins (eds.) X-ray absorption: Principles, Applications, Techniques of EXAFS, SEXAFS and XANES. John Wiley & Sons: New York (1988).
[2] J.M. Charnock, C.M.B. Henderson, T.M. Seward. J. Synchrotron Rad. 6 (1999) 607.
[3] E.H. Oelkers, D.M. Sherman, K.V. Ragnarsdottir, C. Collins. Chem. Geol. 151 (1998) 21.
[4] T.M. Seward, C.M.B. Henderson, J.M. Charnock, B.R. Dobson. Geochim. Cosmochim. Acta 60 (1996) 2273.
[5] N. van Hung, T.S. Tien, L.H. Hung, R. Frahm. Int. J. Mod. Phys. B 22 (2008) 5155
[6] M. A. Karolewski, R.G. Cavell, R.A. Gordon, C.J. Glover, M. Cheah, M.C. Ridgway. J. Synchrotron Rad. 20 (2013) 555.
[7] T. Nikolova, Bachelor Thesis, Universität Wuppertal (2013).

XANES-investigations of ligand-stabilized gold nanoclusters

C. Helmbrecht[a], D. Lützenkirchen-Hecht[b], R. Wagner[b], W. Frank[a]

[a] Institut für Anorganische Chemie und Strukturchemie II, Heinrich-Heine-Universität Düsseldorf, Universitätsstr. 1, 40225 Düsseldorf, Germany.
[b] Fachbereich C-Physik, Bergische Universität Wuppertal, Gaußstr. 20, 42097 Wuppertal, Germany

Au metal nanoparticles with a size between ca. 2 to 100 nm have been well-studied in the past, in particular with regard to their unique optical properties (see e.g. [1-3]). In contrast, only few information is available about particles in the subnanometer range which show molecular-like HOMO-LUMO transitions. In any case, these small gold nanoclusters (AuNC) need protecting capping molecules in order to prevent agglomeration and growth to larger structures. In the present study, we investigate gold nanoclusters with different capping agents like thiols, amines and phosphines. Their synthesis requires an excess of ligands and results in concentrations of the AuNC around 10 ppm. These conditions substantially complicate any investigation of the clusters structure or electronic properties. In particular nanospecies smaller than about 3-5 nm can no longer be reliably determined by X-ray diffraction, and thus X-ray absorption spectroscopy (XAS) with its inherent sensitivity towards the atomic short range order structure was applied in the present experiments. Furthermore, XAS allows the investigation of the clusters incorporated in polymers or glass and in solution as well, so that an analysis of the near range order structure (XANES) may give information about the oxidation state of the nanomaterials. In addition, the influence of the number and the nature of the stabilizing ligands may be studied as well (see e.g. [4, 5]).

In the present study, 1,3,5-Triaza-7-phosphaadamantan ($C_6H_{12}N_3P$, TPA)-stabilized Au nanoclusters were investigated with XANES at the Au L_3-edge using synchrotron radiation from DELTA beamlines 8 and 10. Due to the extremely low concentration of the element of interest of less than 10 ppm, the absorption spectra were collected in the fluorescence mode, where the excited radiation is detected by a peltier-cooled Si pin- diode and a multichannel analyzer (Amptek, Bedford, USA). Several spectra (5-8) were added in order to obtain a reasonable signal-to-noise ratio of the near edge data. Typical results are shown in Fig. 1, where the averaged and normalized spectrum of the TPA-stabilized Au nanoclusters is compared to those of Au reference compounds with different valence. As can be seen, the data quality of the AuNC-TPA is sufficient for a more detailed analysis of e.g. the edge position, the white energy and intensity, and also post edge peaks are clearly resolved.

Obviously, the spectrum obtained from the AuNC-TPA after averaging over several individual spectra is different from those of metallic Au with respect to the edge position and the near edge structure. The spectrum of $Au(PPh_3)Cl$ as a reference for a Au(I) complex differs substantially with regard to the white-line intensity and the post edge structures, most obviously seen in the feature at about 11.97 keV. One suprising fact of the presented data is that the edge position does not shift with the formal chemical valence in a monotonic way as usually observed, i.e. the edge and white-line energies for Au_2O_3 and $AuCl_3$ are similar to that of Au-metal, while those of $Au(PPh_3)$ Cl, $Au(PPh_3)_8$ $(NO_3)_2$ and AuNC-TPA are located at substantially larger photon energies.

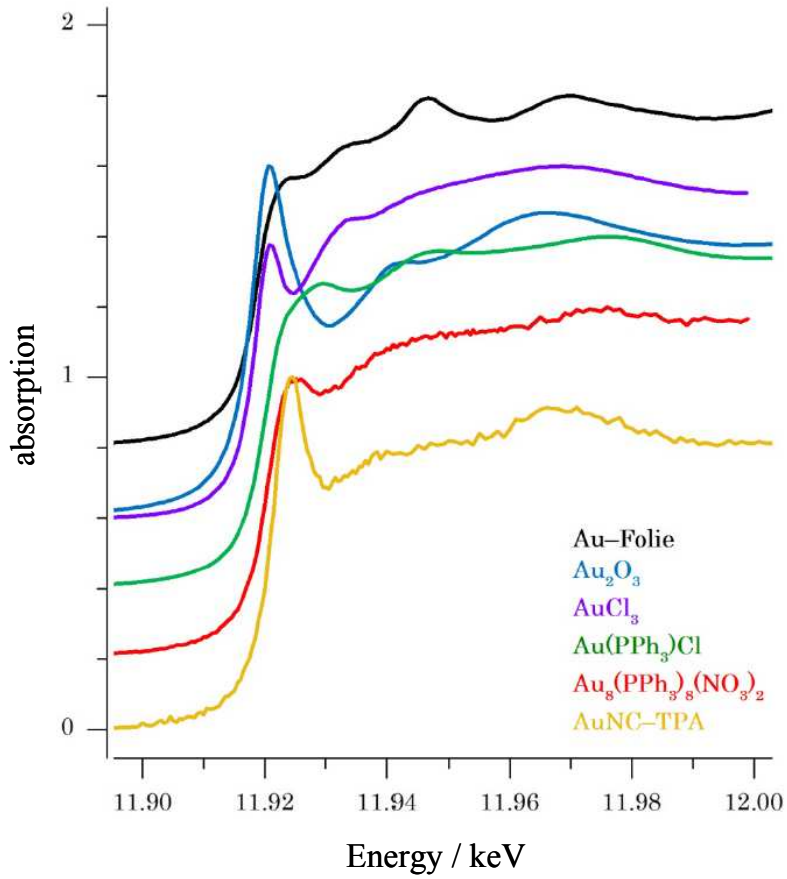

Fig. 1:
Fluorescence mode X-ray absorption near edge spectra of gold nanocluster (AuNC-TPA) in comparison to reference spectra obtained from an Au-metal foil, Au_2O_3, $AuCl_3$, and $Au(PPh_3)Cl$ and $Au_8(PPh_3)_8(NO_3)_2$ as indicated. All spectra are calibrated with respect to the Au foil at 19.919 keV, and the spectra are shifted vertically for a better comparison.

We therefore performed a further data analysis, where the white-line feature is approximated by a Lorentzian peak, and the edge by an atan-function (see [6, 7]). Using such a procedure, a linear relation between the edge position and the valence of the reference compounds was found, and the valence of the AuNC-TPA and the $Au_8(PPh_3)_8(NO_3)_2$ appear slightly larger than the value expected for an Au(I) species. However, the formal valence of $Au_8(PPh_3)_8(NO_3)_2$ is 0.25, and thus a similar value is also deduced for the AuNC-TPA [7].

References

[1] G. Schmid, B. Corain. Eur. J. Inorg. Chem. (2003) 3081.
[2] M.-C. Daniel, D. Astruc. Chem. Rev. 104 (2004) 293.
[3] A. Schwartzberg, J. Z. Zhang. J. Phys. Chem. C 112 (2008) 10323.
[4] A.I. Frenkel, S. Nemzer, I. Pister, L. Soussan, T. Harris, Y. Sun, M.H. Rafailovich. J. Chem. Phys. 123 (2005) 184701.
[5] R.E. Benfield, F. Grandjean, M. Kröll, R. Pugin, T. Sawitowski, G. Schmid. J. Phys. Chem. B 105 (2001) 1961.
[6] J.-H. Choy, Y.-I. Kim. J. Phys. Chem. B 107 (2003) 3348.
[7] C. Helmbrecht, PhD-Dissertation, Heinrich-Heine-Universität Düsseldorf (2014).

The combination of X-ray absorption spectroscopy and X-ray diffraction: Diffraction anomalous fine structure (DAFS) using the PILATUS detector

D. Lützenkirchen-Hecht, J. Meyer, J.-C. Hebig, R. Wagner, R. Frahm

Fachbereich C-Physik, Bergische Universität Wuppertal, Gaußstr. 20, 42097 Wuppertal, Germany

The diffraction anomalous fine structure (DAFS) techniques combines X-ray diffraction and X-ray absorption spectroscopy [1]. DAFS employs the measurement of diffraction peaks of a crystalline sample using energies in the vicinity of an absorption edge of a selected atom in the structure of interest, and simultaneously provides spectroscopic information regarding the local atomic environment of the 'edge atom' through X-ray absorption processes and long-range order information through diffraction processes, thus making element- and site-selective measurements possible [1].

In the present study, we have investigated the feasibility of DAFS measurements at DELTA employing the Pilatus 100 K area detector at beamline 10. In Fig. 1, exemplary diffraction patterns from a Cobalt metal foil are presented for two energies below and above the Co K-edge. While clear diffraction peaks are detectable on an almost vanishing background below the edge, the intensity of the background has substantially increased for the diffraction experiments above the edge, where the detector is homogeneously irradiated by Co-fluorescence photons, and the diffraction peak intensities have decreased strongly. Thus, as a first conclusion, the anomalous dispersion can be well applied at beamline 10 in order to relate the different diffraction peaks to the elements within the sample.

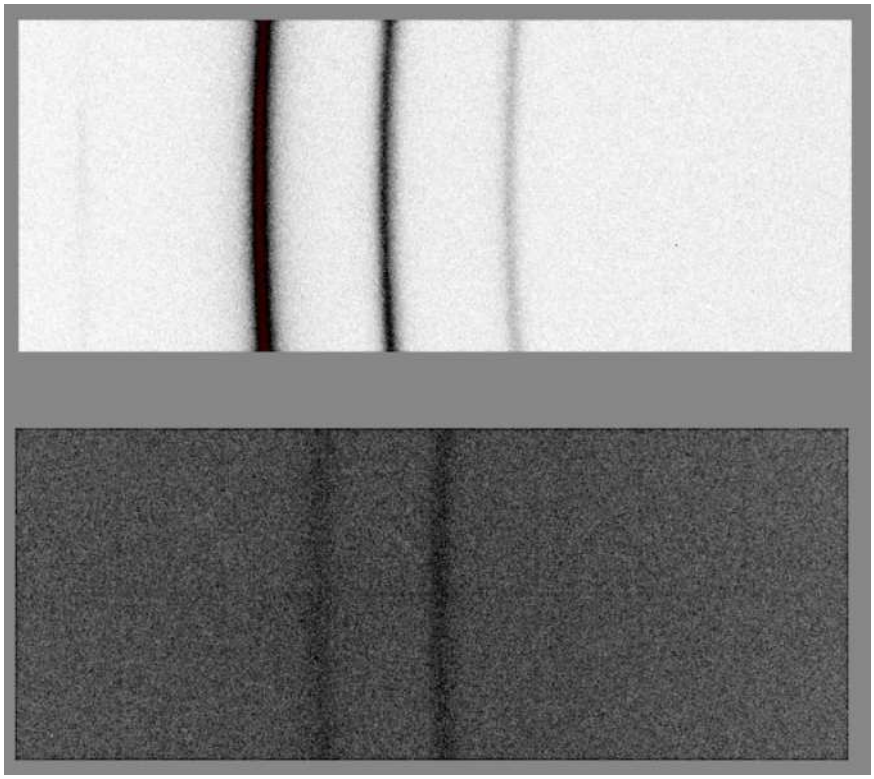

Fig. 1:
Diffraction patterns of a Co-metal foil measured with the PILATUS-detector and a mean diffraction angle of $2\Theta=46°$ (60 s integration time). While the upper diffractogram was measured for a photon energy of 7650 eV, i.e. slightly below the Co K-edge, the bottom diffractogram was measured in the edge at 7723 eV. The overall increase of the background intensity is caused by the onset of the K-shell fluorescence of Co, which makes the data analysis difficult.

A more detailed view of the intensity of the (400)-diffraction peak of a Co_3O_4 sample is presented in Fig. 2. Co_3O_4 is an interesting material for DAFS studies, because it accommodates both Co^{2+} and Co^{3+} ions in its lattice, and by means of DAFS experiments, it should in principle be possible to separate both contributions in the lattice [2].

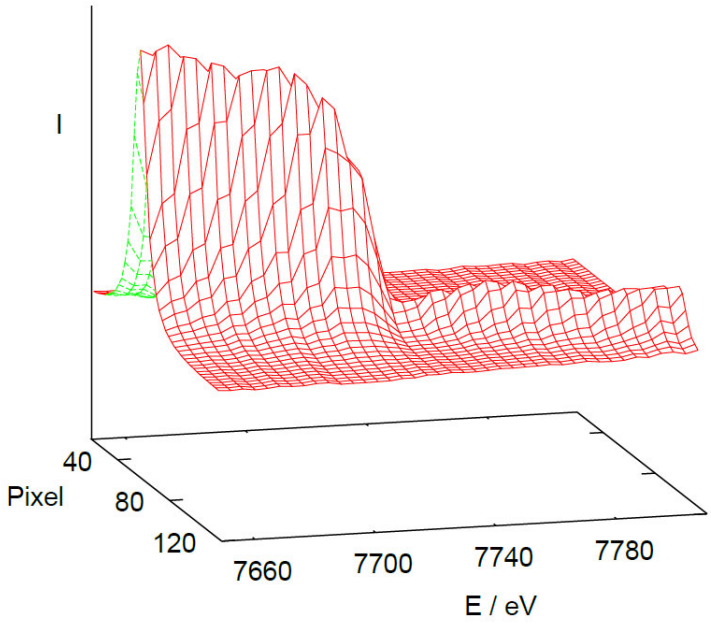

Fig. 2:
(400) diffraction patterns of a Co_3O_4-sample for different photon energies in the region of the Co K-edge. The substantial decrease in diffracted intensity above the edge is clearly detectable, as well as a small modulation in the edge and the post-edge region.

The radially integrated intensity of the (400) diffraction patterns detected for different energies in the vicinity of the Co K-edge of a Co_3O_4-powder sample are presented in Fig. 2. As can be seen, a strong decrease of the diffracted intensity occurs in the edge, and also small variations are visible above the edge. However, model calculations using the DIFFKK-software [3] as well as experimental observations [2] suggest much stronger intensity changes above the edge. More specifically, a stronger increase of the overall intensity with photon energy is expected. The reason for this discrepancy is probably due to the detection of fluorescence photons in the Pilatus detector which are superimposed on the diffracted intensities. Since the fluorescence intensity is directly linked to the absorption of the sample and thus also changes with photon energy from point to point in the spectrum, an adequate extraction of the diffracted intensities is extremely difficult, and still a matter of investigation.

In conclusion, the current setup is at least well suited for making use of the anomalous dispersion in order to identify the contributing X-ray scattering atoms, but for a full DAFS analysis, more work is required.

References

[1] H. Stragier, J.O. Cross, J.J. Rehr, L.B. Sorensen. Phys Rev. Lett. 21 (1992) 3064.
[2] I.J. Pickering, M. Sansone, J. Marsch, G.N. George. J. Amer. Chem. Soc. 115 (1993) 6302.
[3] J.O. Cross, M. Newville, J.J. Rehr, L.B. Sorensen, C.E. Bouldin, G. Watson, T. Gouder, G.H. Lander, M.I. Bell. Phys. Rev. B, 58 (1998) 11215.

Paramagnetic properties of NiTi Nanoparticles studied by X-ray Standing Waves

M. Brücher[1], M. Chakif[2], E.L.Gurevich[2], R. Wagner[3], R. Hergenröder[1]

[1] Leibniz-Institut für Analytische Wissenschaften – ISAS e.V., Dortmund
[2] Lehrstuhl für Laseranwendungstechnik, Universität Bochum
[3] DELTA, TU Dortmund

Nanoparticles possessing superparamagnetic properties are of interest for medical purposes e.g. in cancer therapy.[1, 2] In the present experiments, a polydisperse mixture of NiTi particles was investigated using X-ray Standing Waves (XSW) in order to identify the influence of a magnetic field on the size distribution of the particles.

The experiments were performed at BL10 using a photon energy of 10 keV. A quantity of 10 µl of the acetone suspension containing the particles, which were produced by femtosecond laser ablation, were pipetted on a Si wafer and dried. Fluorescence spectra of the particles (the Kα lines of Ni and Ti) were recorded in angle steps of 0.001°. The resulting fluorescence scan is shown in the upper diagram of Figure 1. After the first measurement, the particles on the wafer were exposed to a magnetic field of B = 0.33 ± 0.01 T, followed by a second angle scan of Ni and Ti fluorescence. The resulting intensity curves of both elements, plotted in the lower part of Figure 1, considerably differ from the first scans: The intensity maximum is shifted towards the critical angle of total reflection; this indicates that the prevailing size of the particles has decreased.

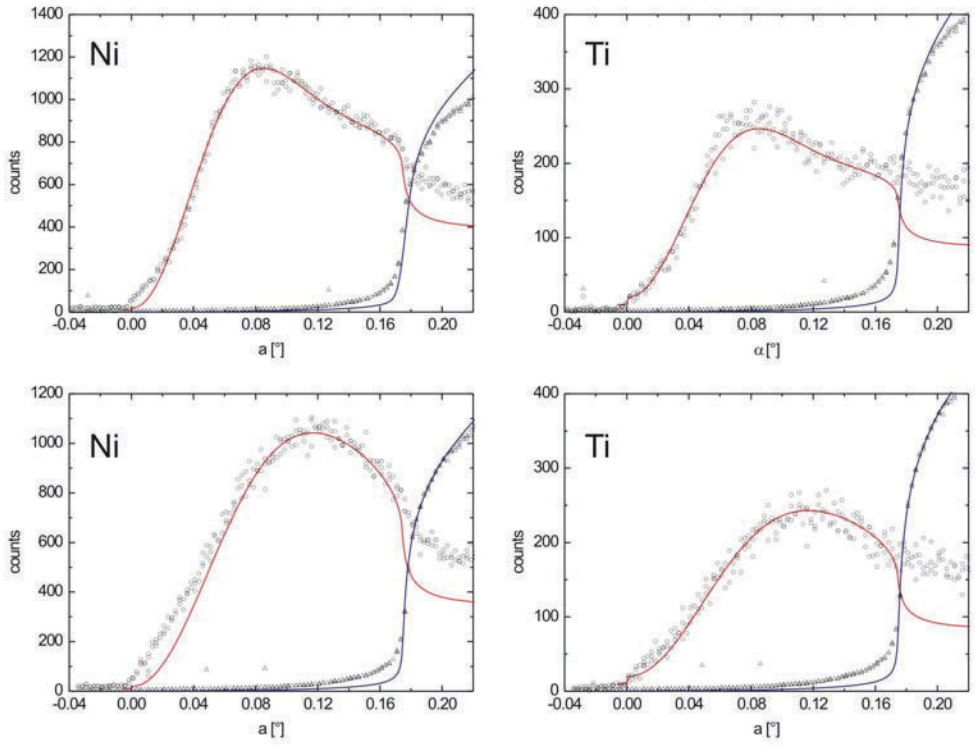

Figure 1: Fluorescence intensity of a NiTi nanoparticle distribution before (above) and after (bottom) the exposure of the sample to a magnetic field. Here, the fluorescence scans of measurement A are shown.

For the quantitative evaluation of the measurement, the XSW-excited fluorescence intensity was calculated for a set of spherical particles of different diameter. The simulation of the measured intensity curves (red lines in Figure 1) was obtained by the linear combination of several individual curves:

$$I(\alpha) = f_1 \cdot I_1(\alpha) + f_2 \cdot I_2(\alpha) + \ldots + f_n \cdot I_n(\alpha) \quad \text{(eq. 1)}$$

This procedure was applied to the results of two pairs of XSW scans, each consisting of one measurement before and after the exposure to the magnetic field. The results are shown in Figure 2:

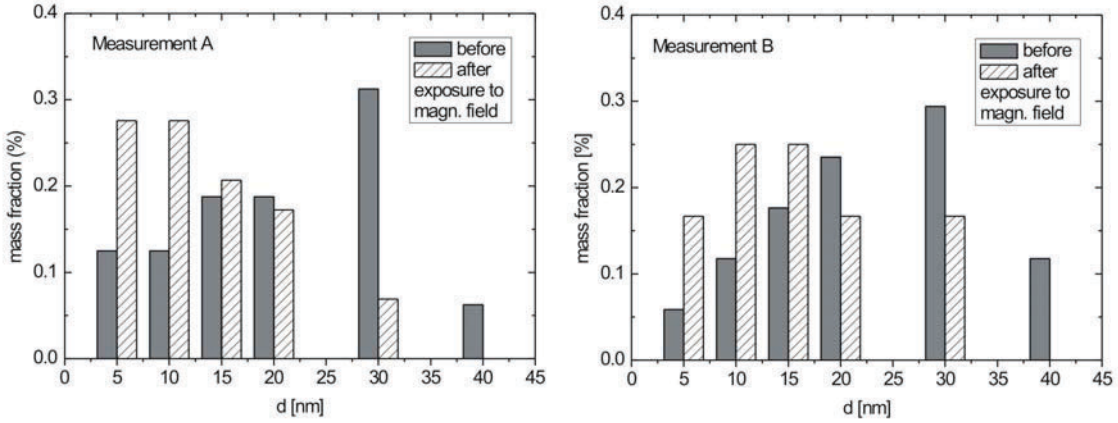

Figure 2: The composition of two NiTi particle distributions before (grey) and after (shaded) the application of a magnetic field.

The grey columns of the histogram show the coefficients f_i of the simulation I(α), the distribution of particle diameters after the application of the magnetic field is plotted by the shaded columns, respectively. The comparison of the diagrams visualizes that the magnetic field mainly removes the particles larger than ca. 20 nm. In contrast to the size distribution, the ratio between Ni and Ti is not influenced by the magnetic field.

Although further studies are necessary for a comprehensive characterization and understanding of the observed effects, the results reveal interesting details concerning the relation of size and magnetic properties of the investigated particles and demonstrate the capability of the XSW technique for the analysis of nanoparticle mixtures featuring a wide range of diameters.

1. M. V. Yigit, A. Moore and M. Zdravka, *Pharm. Res.*, 2012, **29**, 1180-1188.
2. S. Barcikowski, A. Hahn, M. Guggenheim, K. Reimers and A. Ostendorf, *J. Nanopart. Res.*, 2010, **12**, 1733–1742.

Improvements of the low energy XAFS setup at BL8 and experiments at the sulfur K-edge

S. Balk, R. Wagner, D. Lützenkirchen-Hecht, R. Frahm
Fachbereich C – Physik, Bergische Universität Wuppertal, Gaußstr. 20, 42097 Wuppertal

Until last year, the low energy setup at the materials science BL8 [1] at Delta consisted of a pair of YB_{66} monochromator crystals and a differentially-pumped experimental chamber. Unfortunately, this setup did not provided sufficient flux for the detailed investigation of real samples. Furthermore, the intensity monitor for the incident beam turned out to be problematic in conjunction with the beam of the YB_{66}-crystals. Therefore the low-energy setup was completely rebuilt using InSb(111) monochromator crystals. Those crystals offer a substantially larger photon flux, however the low energy side of the spectrum is limited to ca. 1.7 keV, instead of energies around 1.2 keV that can be achieved by using YB_{66} [2, 3]. Still the technologically important K edges of Si, P, S, Cl and Ar are feasible, and the L_3-edges of Rb, Sr, Y, Zr, Nb, Mo, Tc, Ru, Rh, Pd, Ag and Cd. Due to the strong absorption of low energy photons in air, the entire experiment has to be integrated into an ultrahigh-vacuum environment which is directly connected to the storage ring. While the old setup was differentially pumped and build with KF-components, the new one provides all metal sealings for improved vacuum conditions with a base pressure around 10^{-8} mbar. The whole setup is displayed in Fig. 1.

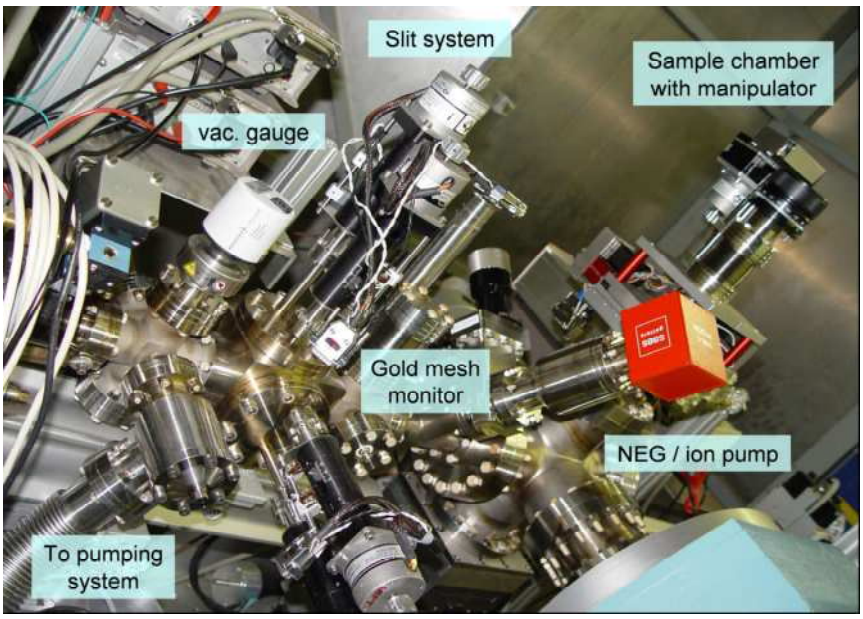

Fig. 1: From left to right: Gate valve that separates experiment and beamline frontend, connection to the turbomolecular pump with full-range gauge, tungsten-carbide slit system, gold mesh monitoring system, NEG/Ion pump. At the right end, the experimental chamber is mounted at the downstream end of the setup.

All used components were especially designed for their use at BL8. The tungsten-carbide slit system with a resolution of 2.5 µm allows beam manipulation in *x* and *y* direction. The monitoring signal is provided by a 15 x 15 mm^2 gold mesh. Using a Keithley 428 current amplifier, which can also apply bias voltages to the mesh, the signal is sent to the beamline control system. The samples can be mounted in a fivefold sample holder on a *z*-manipulator adjustable in the *x*-*y* plane. This allows manipulation of the samples in all 3 dimensions, including 360° rotations. The design of the chamber allows the installation of two different fluorescence detectors, namely a Canberra PIPS detector and an Amptek XR-100SDD silicon drift diode. While the large (7 cm diameter) PIPS detector has a much better solid angle coverage, it is however not energy dispersive unlike the SDD, which on the other hand has only got a very small detector window, that is covered with a thin (12.5µm) Be-foil. The

choice of the detector has to be made in respect to the sample under investigation, i.e. if a sample contains only very small amounts of the element of interest, then it is usually a better choice to use the energy dispersive detector. Doing so will dramatically reduce the overlapping of the background and the elastic scattered photons with the small fluorescence signal of interest. On the other hand, if the element of interest gives a high fluorescence yield, the background will be orders of magnitudes smaller and can be neglected.

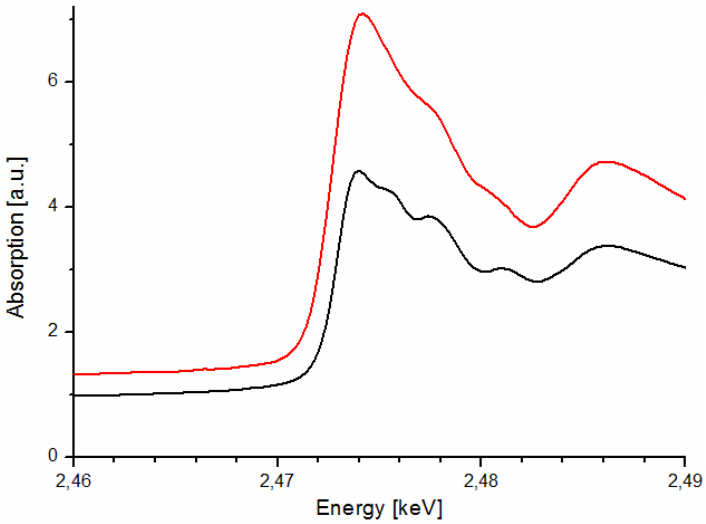

Fig 2: Fluorescence mode ZnS XANES measurements at the sulfur K-edge before (red) and after (black) installing the special crystal. The black curve shows more features, which is due to the improved resolution of the monochromator.

The 15 mm x 20 mm x 2 mm sized InSb(111) crystals are mounted on a water-cooled copper block with special design clamps that minimize the strain on the crystals by equally distributing the pressure that holds them in place. In contrast, the old crystal holder for the first only 1 mm thin InSb crystal induced too much strain by a rather punctual fixation. Unfortunately, the bending of the crystal strongly reduced the energy resolution, which can clearly be observed in the S K-edge XANES spectra of ZnS in Fig 2. While the old setup gives a resolution of about 2-2.5 eV, the new setup gives about 1.5 eV, which is not far from the theoretical value of 1.1 eV at 2.5 keV photon energy [4].

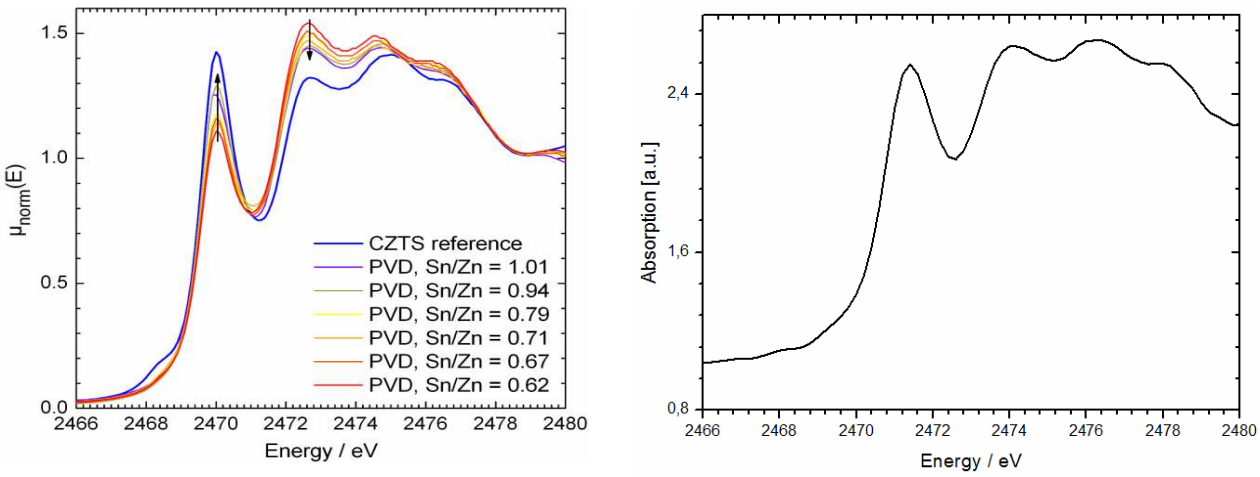

Fig. 3: Comparison of S K-edge XANES of a CZTS kesterite phase test sample at HASYLAB beamline A1 [4] (left) and the new setup at DELTA BL8 (right). The blue curve represents the single phase CZTS reference sample, while the other curves represent CZTS with varying tin to zinc ratios. The latter samples unlike the reference contain a ZnS phase.

These results motivated us to look deeper into experiments at the sulfur K-edge. In a current project [5] we analyze $Cu_2ZnSn(S, Se)_4$ (CZTS) thin film semiconductors, which are a promising absorber material for solar cells. Because of the high amount of different elements there are many possibilities for the formation of secondary phases such as ZnS, CuS, Cu_2S, SnS_{2-x} or Cu_2SnS_3, which influence the performance of the absorber material. The ZnS phase for example, has a much larger band gap than the CZTS, which creates internal barriers and thus diminishes the performance of the solar cell. It is therefore interesting to quantify the ZnS phase within a CZTS sample. To do this, XANES of a single phase CZTS reference sample, a ZnS containing CZTS sample with varying Sn/Zn ratio and a ZnS reference sample were measured at Delta BL8 as well as BL A1 at Hasylab. The corresponding plots, which underlie a different energy calibration and thus have an offset, can be seen in Figs. 2 and 3. At this point it should be noted that both beamlines showed a similar energy resolution, and thus both can in principle be used to do experiments like this. To determine the amount of ZnS, a linear combination of the ZnS reference (Fig. 2) and the CZTS reference (blue curve Fig. 3) has been fitted to the to the measured spectra (Fig. 3). Using the resulting fits even small amounts of down to 3% ZnS can be quantified. This demonstrates that XANES experiments can be used to identify and quantify ZnS phases in CZTS thin film absorbers. We are currently planning an in situ sample heater which would allow us to analyze the formation of the ZnS phase during a controlled annealing procedure.

In conclusion, the presented experiments have shown that the new setup can be used to produce feasible XANES results at low energies in the spectral range of about 1.7 keV to 4 keV and is thus a promising addendum to BL8.

References

[1] D. Lützenkirchen-Hecht, R.Wagner, et al., *J. Synchroton Rad.* **16**, 264 (2009)
[2] A. Herdt, *Diploma Thesis* (2009)
[3] J. Wong, T. Tanaka, et al., *J. Synchrotron Rad.* **6,** 1086 (1999)
[4] F. Schaefers, M. Mertin, et al., *Rev. Sci. Instrum.* **78**, 123102-1-14 (2007)
[5] J. Just, D. Lützenkirchen-Hecht, R. Frahm, et. al, *Appl. Phys. Lett.* **99**, 262105 (2011)

Post-deadline submissions

Deep x-ray lithography at beamline BL1

Thorsten Brenner*, Michael Paulus, Georg Jülicher, Metin Tolan
Fakultät Physik/DELTA, Technische Universität Dortmund, 44221 Dortmund, Germany.
*email: thorsten.brenner@tu-dortmund.de

Beamline BL1 is dedicated to deep x-ray lithography (DXRL). DXRL is a method to produce various microstructures with a height up to several millimeters. Such microstructures can be found in optics, micro mechanics, fluidic, or medical devices. Using DXRL, it is possible to reach a high aspect ratio of about 100 and a lateral resolution up to 2 µm [1]. Thus, DXRL is a industrial relevant method.

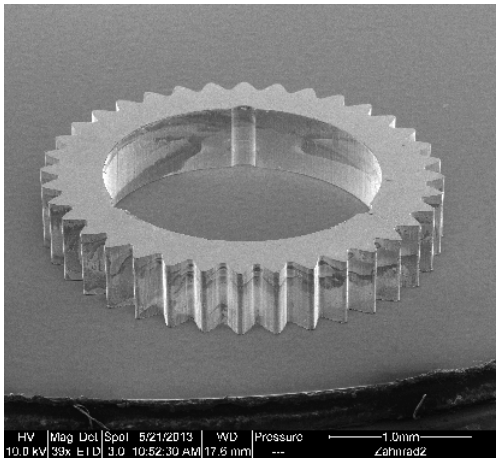

Figure 2: SEM images of a metallic microgear.

The structure production, e. g. the fabrication of microgears used in micro gearboxes, is performed in three different steps [2]: First, a silicon wafer spincoated with a photoresist (550 µm thickness, SU-8) is exposed by polychromatic synchrotron radiation. In this step the two dimensional structure of an absorber material, commonly gold, on a x-ray absorber mask (graphite, beryllium or titanium) is transferred into the photoresist by shadow projection. The exposed resist areas undergo a chemical change regarding their molecular weight. This process is finished by a post exposure bake. In a second step, the exposed wafer is developed chemically. In case of a negative resist (SU-8) the unexposed material is removed. Finally, the ares where the resist has been removed, will be filled applying a galvanic process (nickel). Thus, a metal structure is produced after removal of the remaining photoresist.

In the past year the exposure process at beamline BL1 was optimized. The selection of dose parameters has been chosen more precisely. The post exposure bake has been adapted, implementing weaker heating and cooling ramps. Thus, the deformation of the SU8 surface and the formation of cracks in the resulting structures have been reduced. Furthermore, x-ray masks with smaller and more complex structures have been used at BL1. The development of the wafers and the galvanisation are performed by Micromotion GmbH (Mainz, Germany). Tests of assembled micro gearboxes have shown that the functionality of the produced microparts is given. Thus, BL1 is able to produce microstructures which reach industrial standard.

Acknowledgement
We would like to thank Dr. Alex von Bohlen and Maria Becker (Leibniz-Institut für Analytische Wissenschaften - ISAS - e.V.) for taking the SEM images. We also thank the DELTA machine group for providing synchrotron radiation and for technical support. T. Brenner thanks the NRW Forschungsschule ‘Forschung mit Synchrotronstrahlung in den Nano- und Biowissenschaften‘ for financial support.

References

[1] V. Saile, U. Wallrabe, O. Tabata, J.G. Korvink, O. Brand, G.K. Fedder, C. Hierold (Eds.), *LIGA and its applications*, Wiley-VCH (2009).

[2] *http://www.imt.kit.edu/liga.php*

Correlation of thermoelectric properties with real structure of single $Cu_{2-x}Se$ Nanowires

Ö. Kurtuluş Öztürk[1], Zhen Li[2], Jonas Vogel[3], Ullrich Pietsch[3]

[1] *Physics Department, Doğuş University, Istanbul, Turkey*

[2] *Institute for Superconducting and Electronic Materials, University of Wollongong, North Wollongong, Australia*

[3] *Physics Department, University of Siegen, Siegen, Germany*

Solid-state thermoelectric technology offers a potential for thermal to electrical energy conversion by searching the right materials to work with. On-going challenge has been going on to produce thermoelectric (TE) materials that are efficient enough to be practical. A good TE material is expected to behave as a "phonon-glass electron-crystal" where a crystalline semiconductor structure is desired for the electronic properties while a disordered atomic arrangement is desired for low lattice thermal conductivity.

Cu_2Se crystalized in layered cubic structure which introduces surface roughness, distortions throughout the lattice and reduces the thermal conductivity significantly. Therefore Cu_2Se could behave like phonon-glass electron-crystal. According to the previous studies done with bulk Cu_2Se samples, it has a low electrical conductivity [1], but it is believed that Cu_2Se nanowires would have a lower thermal conductivity because of the thermal phonon boundary scatterings.

In this project, thermoelectric characterization of $Cu_{2-x}Se$ nanowires produced by solution-liquid-solid technique [2] is done. Thermoelectric performance of nanowires should be optimized by means of Cu concentration, temperature and their nanostructure. Cu-Se systems exhibits two phases, tetragonal α phase and face center cubic β phase. According to the studies done up to now with bulk or thin film samples, there exists a phase transition depending on the Cu concentration and temperature [3]. A phase change in their structure would affect the electrical and thermal transport properties of the samples. Therefore the structural properties of the nanowires have been determined by SEM (Figure 1), in situ HRTEM and powder x-ray diffraction technique as it is a fast and non-destructive method for structural analysis of nanowires. The effect of temperature on the crystal structure is planned to be examined by in situ powder XRD measurements in order to check if there would be a phase change in the structure as temperature increases.

The preliminary powder XRD measurements of Cu_2Se nanowires and commercial powders were done at DELTA, BL10 in March 2013 (Figure 2). The measurements were performed at a beam energy of 9keV with a beam size of $0.5*0.5mm^2$. The samples filled into borosilicate glass capillaries were inserted on the Z-stage and measured by Pilatus 2D detector. The

angular values and the background of the raw data were calibrated by using silicon powder as reference material.

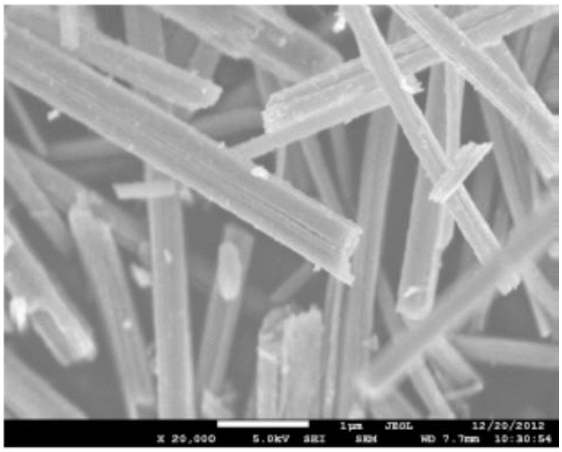

Figure 1. SEM image of Cu_2Se nanowires.

Preliminary diffraction measurements at room temperature confirms that $Cu_{2-x}Se$ nanowires have a polycrystalline structure. A qualitative view of the diffraction pattern seen in Figure 2 corresponds to orthorhombic, tetragonal, hexagonal and monoclinic crystal structures. Hence the nanowires show a non-uniform structure that is called polytypism, which is a result of the growth process. A polytype crystal contains different crystal structures with common crystal facets, which results in similar reflections. The unidentified peaks could be attributed to oxidation during the measurements that would be examined in details in the following measurements.

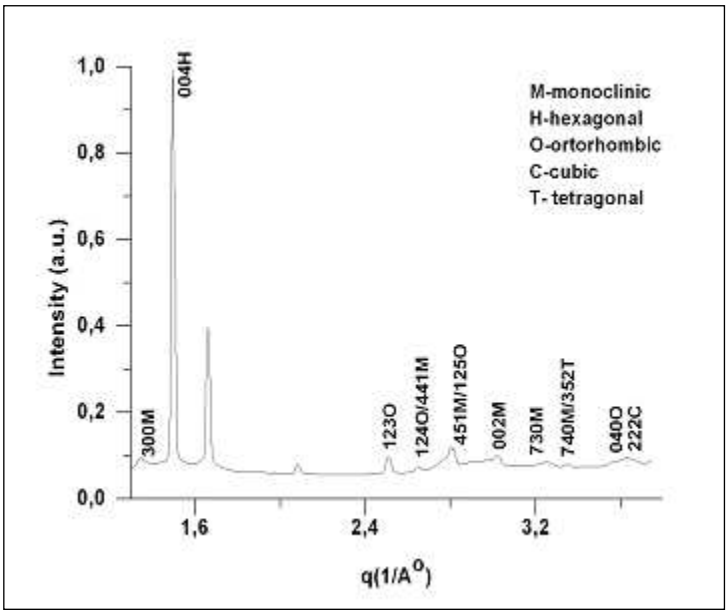

The project is planned to go on with in situ powder diffraction measurements where the temperature will be increased up to 700°C to understand if there is any phase change in the structure, to see if oxidation affects the nanowires and to identify the unknown reflections.

Figure 2. Typical XRD pattern of $Cu_{2-x}Se$ nanowires. Peaks are indexed by Miller indices of either monoclinic, hexagonal, ortorhombic or cubic structure.

References:

1. H. Liu, X. Shi, F. Xu, L. Zhang, W. Zhang, L. Chen, Q. Li, C. Uher, T. Day, G. J. Snyder, *Nature Materials*, DOI: 10.1038/NMAT3273 (2012).
2. Ö. Kurtulus, Z. Li, A. Mews, U. Pietsch, *Physica Status Solidi A*, V206, Issue 8, 1752 (2009).
3. B.Yu, W. Liu, S. Chen, H. Wang, H. Wang, G. Chen, Z. Ren, *Nano Energy*, 1, 472 (2012).

Notes

Notes